ALMA MATER STUDIORUM
UNIVERSITA' DEGLI STUDI DI BOLOGNA

FACOLTA' DI INGEGNERIA

Corso di laurea in Ingegneria civile

D.I.S.T.A.R.T.
Dipartimento di Ingegneria delle Strutture, dei Trasporti,
delle Acque,del Rilevamento e del Territorio

Tesi di laurea
in
Progetto di strutture

COMPUTATIONAL MODELING OF FIBER REINFORCED CONCRETE WITH APPLICATION TO PROJECTILE PENETRATION

Candidato:
Pietro Marangi

Relatore:
Prof. Ing. Marco Savoia

Correlatore:
Prof. Ing. Gianluca Cusatis

*"Ritorna con il tuo scudo
o sopra di esso"*

- Regina Gorgo -

Abstract

Concrete is a material widely used in Civil Engineering due to its good resistance capacity and durability. Even thought engineers have designed the reinforcement of concrete structures for centuries, concrete material is still not well understood. This statement is particularly true outside the elastic range when fracture and other inelastic phenomena occur. The main reason for this hard behavior is due to the extreme complexity of concrete internal structure that is highly heterogeneous. To overcome this problem, in the past, several model have been formulated using different approaches. In this work, the goal is to study at first the Lattice Discrete Particle Model (LDPM) and then to develop one method that allows to study the FRC.

The LDPM will be extended to include the effect of dispersed fibers with the objective of simulating the behavior of fiber reinforced concrete for armoring system applications. The developed model, named LDPM-F, is validated by carrying out numerical simulations of three-point bending tests on fiber reinforced concrete mixed characterized by various fiber volume fractions. Finally, LDPM-F is applied to the analysis o the penetration resistance of fiber reinforced slabs.

In Chapter 1 the formulation of the LDPM is presented and explained, showing the geometry of the model.

In Chapter 2 the constitutive law for interaction of fiber-concrete is described and explained.

In Chapter 3 an experimental campaign of uniaxial compression tests and three point bending tests on plain concrete specimens are simulated.

In Chapter 4 an experimental campaign of three point bending tests on FRC specimens is simulated and the calibration and validation phases are described, in order to clarify the LDPM-F.

In Chapter 5 the results found in the previous chapters will be used for armoring system applications, in order to predict the FRC response.

Contents

Chapter 1

The lattice Discrete Particle Model (LDPM)

Introduction

Concrete is an heterogeneous material, constituted by three phases, with different property: aggregate, matrix and interfacial boundary. In order to investigate these aspects, a lot of models have been proposed in recent years, but although these allowed us to achieve good results, the concrete feature is not still completely understood. The principal reason of this, is the complexity of the internal structure, that is linked with the length scales of observation used for the model.

By this point of view, changing the observation level, is possible to show, different aspects that are directly matched with the heterogeneity of the material.

The scale length range from the atomistic scale (10^{-15} m), characterized by the behavior of crystalline particles of hydrated Portland, to the macroscopic scale (10^1 m), at which concrete has been traditionally considered homogeneous.

In the last twenty years, several authors, have done materials models that use miniscale or mesoscale, to study this kind of material, in special way for the geological problems.

Miniscale models in which concrete is treated as three-phase composites have been proposed by Wittmann (1988), and Carol (2001). They used finite element technique to model with different constitutive laws coarse aggregate pieces, mortar matrix, and inclusion-matrix interface. Another remarkable study is done by Van Mier and coworkers (1992), they proposed a model realized with finite elements but without continuum hypothesis. Concrete was modeled through a discrete system of beams. Important is also the experience by Bolander (1999), which realized a discrete miniscale model based on the interaction between rigid particles obtained though the Voronoi tessellation of the domain.

The main advantage of miniscale models is they are able to reproduce realistic simulation of cracking, coalescence of multiple distribution cracks into localized cracks, and fracture propagation. The only problem that affect these kind of model is that they tend to be computationally intensive especially for 3D modeling.

Mesoscale models appear because they are computationally less demanding than the miniscale models. For mesoscale model, concrete is modeled by the whole

aggregate pieces and the layer of mortar matrix between them. The technique used is finite element. Some examples are Cusatis et al (2003a,b), Cusatis et al (2006), Cusatis & Cedolin (2006).

Summarizing every thing, the principal difference among these two approaches is that, miniscale model describe the concrete like three-phase material: cement paste, aggregate and interfacial transitional zone, and the length scale is of 10^{-4} m or less. The mesoscale, is fundamentally different, because this show only the mortar and the coarse aggregate, and the scale order is 10^{-3} m. Both approaches have the problem, which are very numerically expensive, but for the concrete has been seen that using the mesoscale model, that is relative expensive, and is also possible to achieve fairly good results like the miniscale.

The old models, implemented for macroscale, allowed to obtain good result, but they are not able to simulate material heterogeneity and its effect on damage evolution and fracture. For solving these problems now, one possible manner is to use models, that are able to simulate the concrete at the level of the mesostructure, with discrete approach. In this way, it is possible to replicate damage and fracture, and to capture the phenomena related to the randomness of the material.

Features of the model

The model present in this work, use an analysis at the mesoscale level and is called Lattice Discrete Particle Model (LDPM). It is the result of the union by two different models: Discrete Particle Model (DPM) and Shear Lattice Model (CSL). The principals features of the model are:

a) Concrete mesostructure is simulated by a lattice that match a system of particles that are in interaction into their through triangular facets. This lattice is obtained by a Delaunay triangulation of the aggregate centers.

b) The specimen is created by a randomly distribution of particles, that is computed taking in account the basic properties and the granulometric of the aggregate.

c) The geometrical interaction between the particles is obtained by three-dimensional domain tessellation defining a set of polyhedral cells each including one piece of the aggregate.

d) Two adjacent pieces of aggregates are connected by the generic lattice element, that transmits shear and normal stresses. These are assumed functions of normal and shear strains. Allotting the displacements the model works, and permit to find the stress field.

e) The stresses act on contact areas which are defined by constructing a barycentric dual complex of the Delaunay triangulation.

f) Starting from the strains is possible, using the constitutive law to define the stresses, taking into account the stress-strain boundaries.

g) The constitutive law give the following behavior: softening for pure tension, shear-tension and shear with low compression and it is hardening for pure compression and shear with high compression.

h) Friction and cohesion are shown into the shear response.

LDPM has inherited from DPM the MARS computational environment that includes long range contact capabilities typical of the classical formulation of Discrete Element Methods (DEM). This feature is particularly important to simulate pervasive failure and fragmentation.
LDPM allows to capture a number of new features that greatly improve its modeling and predictive capabilities. These new aspects can be explained as follows:

1) The particles interaction is formulated by the assemblage of four aggregate pieces whose center are the vertex of the Delaunay tetrahedralization. This model geometry allows to include into the constitutive law the volumetric effects, that the other models are not able to capture.

2) Each single aggregate is contained into one polyhedral cells that is made by different triangle facet. Stresses and strains are defined at each single facet. This configuration allows a better stress resolution in the mesostructure, which, in turn, lead to a better representation of mesoscale fracture and damage.

3) The constitutive law simulates the most relevant physical phenomena governing concrete damage and failure under tension as well as compression. This law compared with the previously existed provides better modeling and predictive capabilities especially for the macroscopic behavior in compression with confinement effects.

The LDPM is able to simulate all aspect of concrete response under quasi-static loading, including tensile fracturing, cohesive fracture and also size effect, compression-shear behavior with softening zero or mild confinement, and high confined compression, and strength increase under biaxial loading. The following sections will explain before the geometrical characterization of the model and then equilibrium equation with constitutive law.

Geometrical Characterization of Concrete Mesostructure

The geometrical structure of the concrete mesostructure is obtained with four divers steps. In these phases the objectives is define:

1) Number and size of coarse aggregate pieces;

2) Particle position;

3) Inter-particle connections;

4) The creation of a surface, into the two adjacent particles that permit to exchange the forces.

First step: Number and size of coarse aggregate pieces

The first step is to define the particles diameters and the respective number, that will be used for refill the specimen volume, and generate the its surfaces. In this sense, there are different practice to make this in the LDPM, first of all it will compute the particles and then the zero node point, that also will be explain in the following section. However, the first hypothesis is to consider the particles with sphere shape, under this assumption, the concrete granulometric distribution can be represented by *particle size distribution function* (Psd)*,* proposed by Stroeven:

$$f(d) = \frac{q d_0^q}{\left[1 - (d_0/d_a)^q\right] \cdot d^{q+1}}$$

where d_a is the maximum aggregate size and d_0 represent the minimum particle size.

The precedent Psd, can be interpreted as probability density function (Pdf), this will allow to find the percentage associated with a certain diameter, using the cumulative distribution function (Cdf), that is expressed as:

$$P(d) = \int_{d_0}^{d} f(d)\delta d = \frac{1 - (d_0/d)^q}{1 - (d_0/d_a)^q}$$

It may be shown that the Psd is associated with a sieve curve in this way:

$$F(d) = \left(\frac{d}{d_a}\right)^n$$

where $n = 3 - q$. For $q = 2.5$, the relation represent the classical Fuller curve extensively used for the concrete. With this curve is possible to check the concrete granulometric, analyzing the percentage of passing in function of the diameter, in this way the concrete quality is guaranteed if this curve is contained into the Fuller range. This technique allows to have the best specimen refill and to avoid the empty space, as showed in the Cusatis (2001).

The specimens used in the simulations have particles created with the 30% of the total curve granulometric (Fuller curve), starting from the coarse aggregate; this allows us to find good results, because the computational cost is lower and at the same time there are not big differences between results found using another percentage of generation.

For simulate the specimen in terms of number and diameters of particles, it is important to know: c = cement content, w/c = water to cement ratio, V = specimen volume, d_a = maximum aggregate size, d_0 = minimum particle size.

The following procedure is used to find and then place the particles inside the specimen volume:

a) Calculate the volume aggregate fraction as $v_a = 1 - c/\rho_c - w/\rho_w - v_{air}$, where $w = (w/c)c$ is the water mass content per unit volume of concrete, $\rho_c = 3150\,Kg/m^3$ is the mass density of cement, $\rho_w = 1000\,Kg/m^3$ is the mass density of the water, and v_{air} is the volume fraction of entrapped or entrained air, (usually 3-4%);

b) Compute the volume fraction of simulated aggregate using the following relation: $v_{ao} = [1 - F(d_o)]v_a = [1 - (d_0/d_a)^n]\cdot v_a$;

c) Compute the total volume of simulated aggregate as $V_{ao} = v_{ao}V$;

d) Calculate the particle diameter by sampling the Cdf by a random numeric generator: $d_i = d_0[1 - P_i(1 - d_0^q / d_a^q)]^{-1/q}$, where P_i is a sequence of random numbers between 0 and 1.

e) The total number of the particles is obtained by checking, for each new generated diameter in the sequence, that the total volume of the generated particles $\tilde{V}_{a0} = \Sigma(\pi d_i^3/6)$ does not exceed V_{a0}. When for the first time,

$\widetilde{V}_{a0} > V_{a0}$ occurs, the current generated particle is discarded and the particle generation is arrested, Cusatis and coworkers (2009).

The graphical representation of the procedure explained before is shown in the Fig. 1.1, whereas in the Fig. 1.2 is represent the computational sieve curve obtained during the generation of a cube specimen characterized by c = 300 kg/m^3, w/c = 0.5, d_0 = 4 mm and d_a = 12 mm.
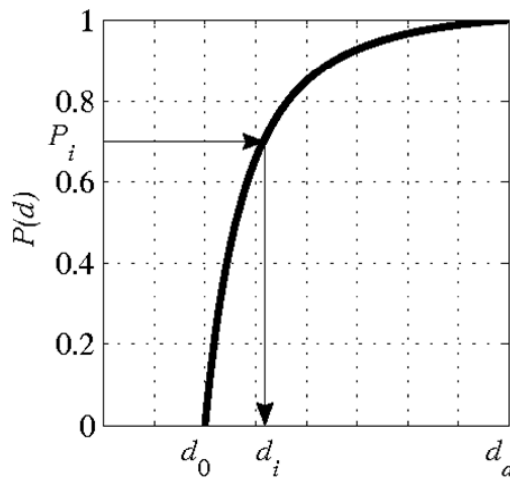
Figure 1.1: Cumulative distribution curve

The diameters and number particles, found in this way, will be used to fill the specimen, now the procedure will be completed creating the zero-diameters particles (nodes), that will be placed over the external surfaces. That practice, is important, for the third step, when the tetrahedral will be generated.
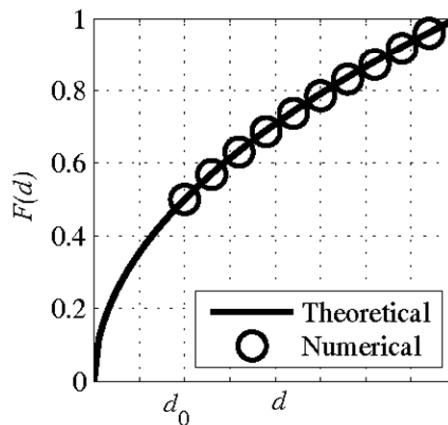
Figure 1.2: Computational sieve curve

The method used to search the number of surface nodes is the following, assuming that the external surface of the specimen volume can be described with a set of polyhedral face, and that is L_e is the generic length of the edge specimen, and A_p the generic surface area, the number of the nodes will be given by these ratio L_e/h_s and A_p/h_s^2, where h_s is the average surface mesh size, chosen such that the discretization resolution on the resolution on the surface is comparable to the one inside the specimen. This is done using this relation $h_s = \xi_s d_0$, by numerical experiment which showed that putting $\xi_s = 1.5$ leads to obtain good results. Clearly for each vertex on the external surface will be placed one node.

Second step: Particle position

The particle computed before, will be now placed in the volume specimen, using a random distribution, on vertexes, edges, surfaces, faces and interior volume. The following idea for the ranked, is first of all, set the vertex nodes, and after in the edges and surface created among these vertex nodes, place other particles, by allowing a minimum distance of $\delta_s d_0$ to minimize the geometrical error of the discretization. The typical value used for $\delta_s = 1.1$, permit to achieve good mesh.

Using a procedure introduced by Bažant, it is possible to generate a statistically isotropic random mesostructure, where the center of particles are placed in the volume of the specimen one by one, from the largest to the smallest.

When the procedure, for generate the particles position, is finished, one control is done, for avoid possible overlaps of this particle with the previously placed particles and with surface nodes. In this phase, at the surface nodes are assigned a fictitious diameter of $\delta_s d_0$ and a minimum distance of $d_i/2 + d_j/2 + \xi d_0$ among the center of the particles with diameters d_i and d_j is enforced. The value of ζ, is very important, because it determines the concrete behavior, for $\zeta=0$ or very small values, the particles distribution is not statically isotropic, and present areas where there are low particle density and others zones with high particle density. In the same manner using very large values of ζ, the specimen volume is saturated quickly and not all particles can be positioned. After several numerical experiments, the best value found is $\zeta = 0.2$, using this, it is possible to avoid the volume saturation while leading uniform particle distribution.

Third step: Inter-particle connection

The third step lets to define the topology of the interaction among the particles. This is performed using a Delaunay tetrahedralization, that utilizing the nodal coordinates of the particles center allows to build three-dimensional tetrahedral, which does not overlap, fill all the volume of the specimen. In each vertex of the

tetrahedrals is placed a particle, generated in the first step, and permit to fill the total volume specimen. In this study, the Delaunay tetrahedralization is carried out by using the TenGen code.

Fourth step: facets generation

The last step, the forth has the aim to define the surface through which the forced are exchanged from one particle to another. There are different ideas proposed for describing this aspect of the problem, in previous works, the interaction between the particles were realized by the edge that was created as a strut. It connected the two adjacent particles, and the effective area of this strut was defined by performing a tessellation of the domain anchored to Delaunay tetrahedralization. This approach gives a good result in terms of fracture behavior and also for the concrete failure under unconfined compression. These methods have the lacuna that does not say something about the volumetric effects that are essential for description of the concrete behavior under high confining pressure.

In the LDPM model, the principal thing is the elementary cell, that is the tetrahedral. There be possible, to see this like the union of four sub-domains, where each sub-domain contains one particle, see Fig. 1.7. The single facet of these sub-domains will be the surface, where will be applied the relation to allow the force exchange.

The last phase will be realized for this local geometry for every elementary cell and for each particles. Starting from the tetrahedral, the tessellation will be construction of the following procedure:

a) One point on each edge (edge-point) is defined at midway of the counterpart of the edge not belonging to the associated particles (point E_{ij} in the Fig. 1.3);

b) One point on each triangular face (face point) of the tetrahedron is defined as follows. First points located on the straight lines connecting each face node to the edge point located on the edge opposite to the node under consideration are considered. Similarly to the edge points, these points are located at midway of the line counterpart not belonging to the associated particles. See point F^*_{kl} in Fig. 1.4 . Later, the facet point is selected as the centroid of the F^*_{kl} point. See point F_l, in Fig. 1.4.
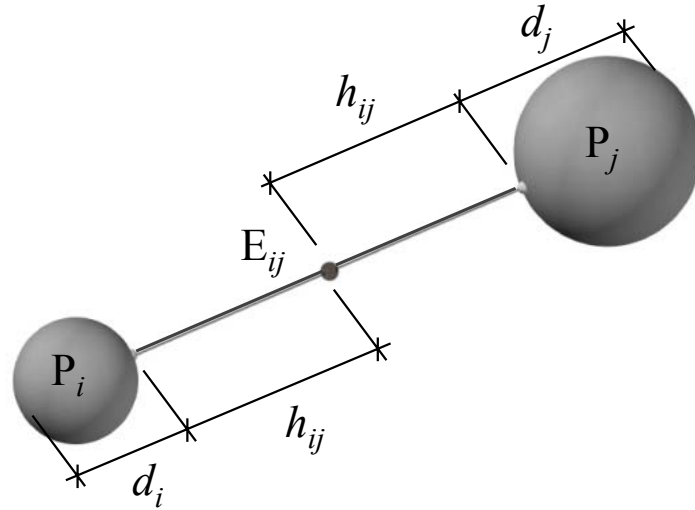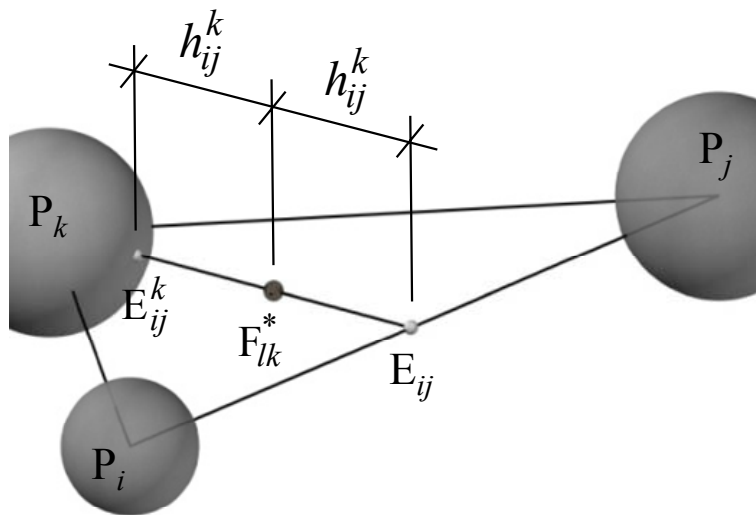
Figure 1.3: Construction for edge-point

Figure 1.4: Construction for face-point

c) One point in the interior of the tetrahedron (tet-point) is defined by the centroid (T_l in Fig. 1.5) of the points identified, similarly to what is done for the face points in item 2, on the straight lines connecting each node of the tetrahedron with the face points on the face opposite to the node under consideration (points T_l^* in Fig. 1.5). Again, these point are located at midway of the line counterpart not belonging to the associated particles.
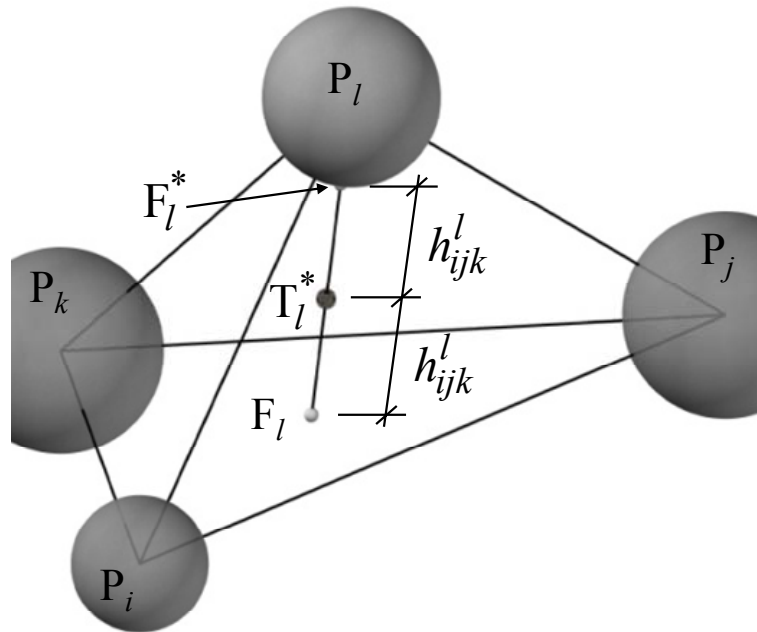
Figure 1.5: Construction for Tet-point

d) Finally, the tessellation of the tetrahedron is obtained by the set of triangles by connecting the tet-point with the one of the edge-points and one of the face-points. Each tetrahedron result tessellated with twelve triangular face (Fig. 1.6).

This is only one type of tessellation possible, basically different procedure could be realized but numerical experiments show that this is the best for minimize the intersection between the tessellating surface and the particles. Isolating one particle and its facets, a polyhedral cell is obtained.
This is the sub domain that has irregular and also random shape, this characteristic is an important property that ensures a realistic representation of the kinematics of the concrete mesostructure, and it especially allows avoiding the excessive rotation.
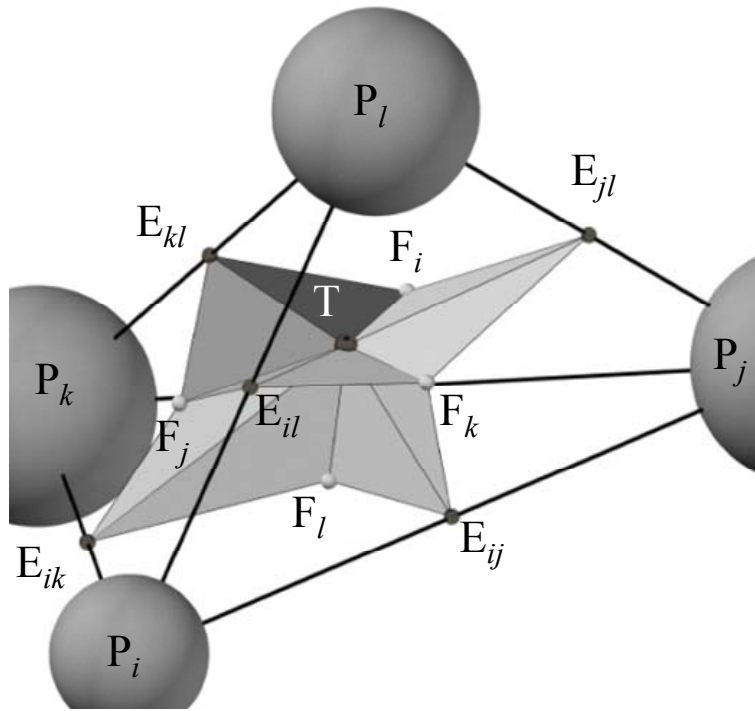
Figure 1.6: Tessellation of the tetrahedron.
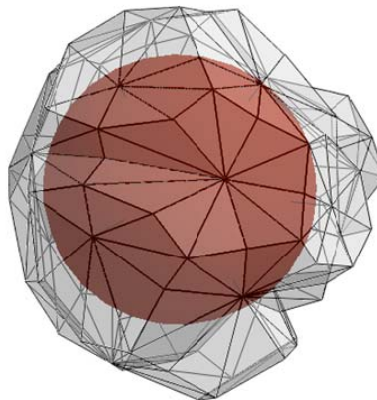
Figure 1.7: Particle sub-domain

Discrete Compatibility and Equilibrium Equations

The tetrahedron formed by the basic four-particles, as showed in the Fig.1.7, is the primary element used to derive the governing equations of the model. Every particle, which forms this tetrahedron, is included in a sub-domains V_i (i =1,…..,4), and all together create the original element. Each sub-domain, has a portion of the three tetrahedron edges attached to the node and also, six triangular tessellation facet joint to the three edges, Fig. 1.8. One of the most important things is to describe, the displacement field in every domain, this is done by rigid body kinematics.
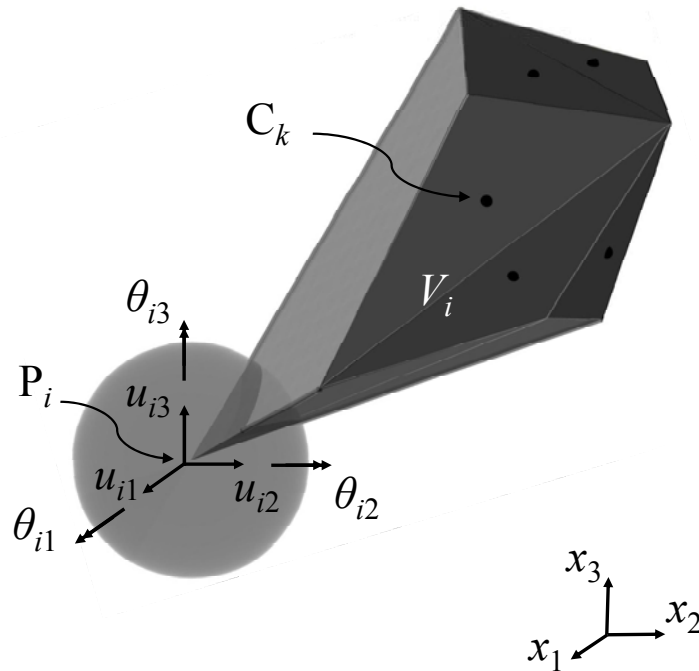
Figure 1.8: Sub-domain geometry.

In order to know the movement of the mid-point, situated over every tetrahedron edge, is important know the displacement and also the coordinates of the center for each particles. Describing $x = [x_1; x_2, x_3]^T \in V_i$, the vector that contains the node coordinates, one can write the following expression:

$$\boldsymbol{u}(\boldsymbol{x}) = \boldsymbol{u}_i + \boldsymbol{\theta}_i \times (\boldsymbol{x} - \boldsymbol{x}_i) = \boldsymbol{A}_i(\boldsymbol{x}) \cdot \boldsymbol{Q}_i$$

where:

$$A_i(\boldsymbol{x}) = \begin{bmatrix} 1 & 0 & 0 & 0 & x_3 - x_{3i} & x_{2i} - x_2 \\ 0 & 1 & 0 & x_{3i} - x_3 & 0 & x_1 - x_{1i} \\ 0 & 0 & 1 & x_2 - x_{2i} & x_{1i} - x_1 & 0 \end{bmatrix}$$

In this equation, the vector $\mathbf{x}_i$ contain the position coordinate of node i, the displacement field is described by $\boldsymbol{Q}_i^T = \begin{bmatrix} \boldsymbol{u}_i^T \boldsymbol{\theta}_i^T \end{bmatrix}^T$ which is realized with the translation $\boldsymbol{u}_i^T = \begin{bmatrix} u_{1i} u_{2i} u_{3i} \end{bmatrix}$, and the rotation $\boldsymbol{\theta}_i^T = \begin{bmatrix} \theta_{1i} \theta_{2i} \theta_{3i} \end{bmatrix}$, that are the degrees of freedom of node i. The displacement jump at the centroid C, of each face, is defined as:

$$[\boldsymbol{u}_{Ck}] = \boldsymbol{u}_{Cj} - \boldsymbol{u}_{Ci}$$

where i and j, are the nodes adjacent to facet k, and:

$$\begin{cases} \boldsymbol{u}_{Cj} = \boldsymbol{u}(\boldsymbol{x}_{Ck}^+) \\ \boldsymbol{u}_{Ci} = \boldsymbol{u}(\boldsymbol{x}_{Ck}^-) \end{cases}$$

represent the displacement field at the facet centroid C_k for $x_{Ck}^+ \in V_i$ and $x_{Ck}^- \in V_j$, see Fig. 1.9.

In order to find the facet strain vector, define as $l_e^{-1} \cdot [\boldsymbol{u}_{Ck}]$, the displacement jump are divided by l_e, where:

$$l_e = \left\| \boldsymbol{x}_j - \boldsymbol{x}_i \right\| = \left[(\boldsymbol{x}_j - \boldsymbol{x}_i)^T \cdot (\boldsymbol{x}_j - \boldsymbol{x}_i) \right]^{1/2}$$

that represents the length of the edge e. To show the real behavior not symmetrical tension compression of concrete, and be able to formulate an appropriate constitutive law, the strain vector $l_e^{-1} \cdot [u_{Ck}]$ is decomposed in normal and shear components, (Fig. 1.10). This is done taking in the count the projection of the tessellation facets, into the planes that are orthogonal to the edge.
The projected facets, are used for the definition of LDPM strain components to avoid non-symmetric behavior under pure shear. It is possible to understand this idea, seeing the Fig. 1.10, where the relative nodal displacement orthogonal to an edge, produce only shear on the projected face at the place of original facet where there also are tension or compression.

Proceeding in this way, the strain components are defined as:

$$\varepsilon_{Nk} = \frac{\boldsymbol{n}_k^T \|\boldsymbol{u}_{Ck}\|}{l_e} = \boldsymbol{B}_N^{jk}\boldsymbol{Q}_j - \boldsymbol{B}_N^{ik}\boldsymbol{Q}_i$$

$$\varepsilon_{Lk} = \frac{\boldsymbol{l}_k^T \|\boldsymbol{u}_{Ck}\|}{l_e} = \boldsymbol{B}_L^{jk}\boldsymbol{Q}_j - \boldsymbol{B}_L^{ik}\boldsymbol{Q}_i$$

$$\varepsilon_{Mk} = \frac{\boldsymbol{m}_k^T \|\boldsymbol{u}_{Ck}\|}{l_e} = \boldsymbol{B}_M^{jk}\boldsymbol{Q}_j - \boldsymbol{B}_M^{ik}\boldsymbol{Q}_i$$

where $\boldsymbol{n}_k = (\boldsymbol{x}_j - \boldsymbol{x}_i)/l_e$, $\boldsymbol{m}_k$ and $\boldsymbol{l}_k$ are two direction that are mutually and orthogonal in the plane of the projected facets, and $\boldsymbol{B}_N^{pk} = (1/l_e)\boldsymbol{n}_k^T A_p(\boldsymbol{x}_{Ck})$, $\boldsymbol{B}_L^{pk} = (1/l_e)\boldsymbol{l}_k^T A_p(\boldsymbol{x}_{Ck})$ and $\boldsymbol{B}_M^{pk} = (1/l_e)\boldsymbol{m}_k^T A_p(\boldsymbol{x}_{Ck})$, $p=i,j$.
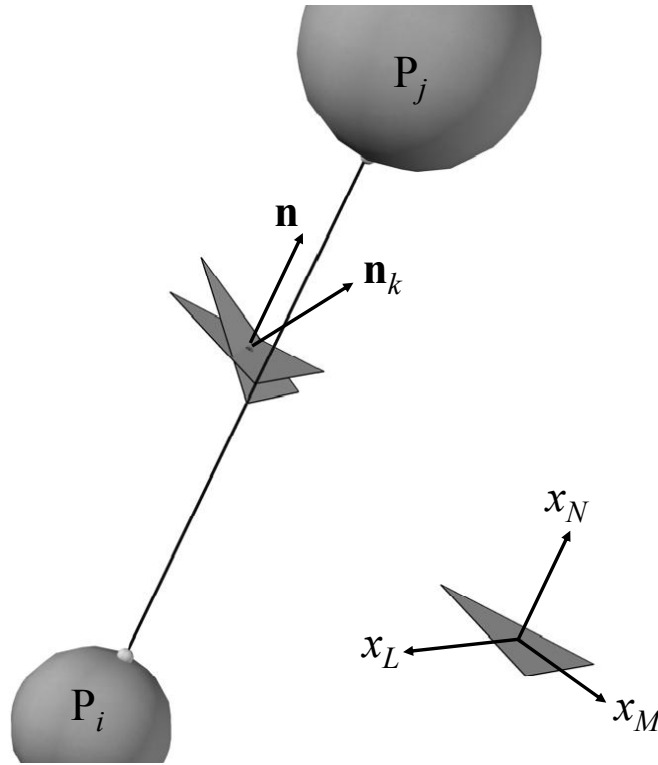

Figure 1.9: Projection of the facets, into planes orthogonal to the edge.

The equations shown here are the discrete compatibility equations of the LDPM formulation.

The normal and shear stresses for each facet is calculate by mesoscale constitutive law, usually is written $\boldsymbol{\sigma}_k = \boldsymbol{F}(\varepsilon_k, \boldsymbol{\xi}_k)$ where $\boldsymbol{\sigma}_k$, ε_k and $\boldsymbol{\xi}_k$ are vectors collecting facet stresses, strain and internal variable, respectively.
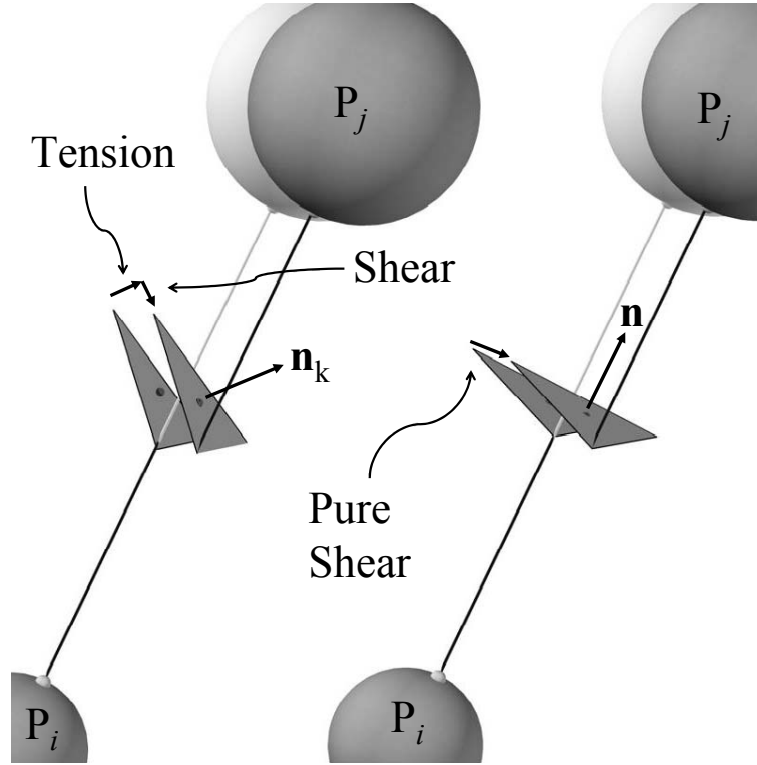
Figure 1.10: Tension and shear components.

Employing the Principle of Virtual Work (PVW), the governing equations can be completed, with the imposing of equilibrium. Using the PVW, in the aspect of virtual displacement, in this case the internal work match with a generic facet can be expressed like:

$$\delta W_k = l_e A_k \boldsymbol{\sigma}_k^T \delta\boldsymbol{\varepsilon}_k = l_e A_k \left(\sigma_{Nk}\delta\varepsilon_{Nk} + \sigma_{Lk}\delta\varepsilon_{Lk} + \sigma_{Mk}\delta\varepsilon_{Mk} \right)$$

where A_k is the area of the projected facet. Substituting the previously equations into the virtual work relation is obtained:

$$\delta W_k = \boldsymbol{F}_{ik}^T \delta\boldsymbol{Q}_i + \boldsymbol{F}_{jk}^T \delta\boldsymbol{Q}_j$$

where:

$$\boldsymbol{F}_{ik}^T = -l_e A_k \left(\sigma_{Nk}\boldsymbol{B}_N^{ik} + \sigma_{Mk}\boldsymbol{B}_M^{ik} + \sigma_{Lk}\boldsymbol{B}_L^{ik} \right)$$

$$F_{jk}^T = l_e A_k \left(\sigma_{Nk}\boldsymbol{B}_N^{kJ} + \sigma_{Mk}\boldsymbol{B}_M^{kj} + \sigma_{Lk}\boldsymbol{B}_L^{kj} \right)$$

This relation express the nodal force at the nodes i and j, associated with the facet k.

Then putting all together the contributions of the several facets and comparing the total internal work with the total external work one can obtain the discrete equilibrium equations of the LDPM formulation. It is also possible, to prove that the equilibrium equations obtained through the PVW corresponds exactly to the translational and rotational equilibrium of each LDPM cell.

LDPM Constitutive Law

The constitutive law, used for LDPM, allows us to put in match the strain vector with the stress vector at the facet level. For realizing the study over concrete behavior, it is better to divide it into: elastic and inelastic behaviors. The stress domain view two different regions that are the for tensile and compressive behavior, Fig. 1.11. This partition is very important because in the tensile field shear and compression are directly matched, but this relation changes completely, in the compression stage, where only the shear in connected with the compression.
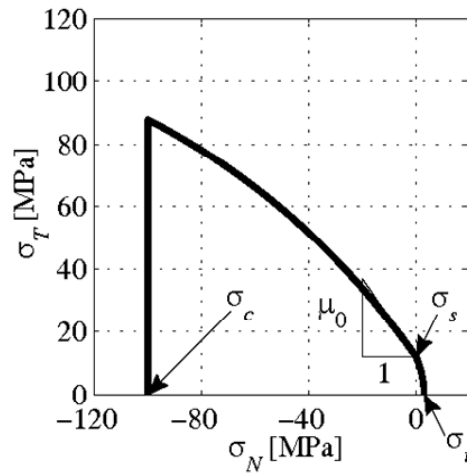
Figure 1.11: Total LDPM domain.

Elastic behavior

In the elastic behavior, the normal and shear stresses are assumed proportional to the corresponding strains:

$$\begin{cases} \sigma_N = E_N \varepsilon_N \\ \sigma_M = E_T \varepsilon_M \\ \sigma_L = E_T \varepsilon_L \end{cases}$$

where $E_N = E_0$, $E_T = \alpha E_0$, E_0 = effective normal modulus, and α = shear normal coupling parameter. These parameters now presented, are the mesostructure parameters, and are assumed to be material properties. This can be demonstrated, looking at the experimental text result obtained in elastic regime.

As mentioned in the introduction, the concrete behavior changes with the observation scale. At the macroscopic level it is consider statistically homogeneous and isotropic material, and therefore the concrete elastic behavior is modeled in the literature by the classic theory of elasticity. The first objective now, is to find one relationship among mesoscale LDPM parameters (α and E_0), and the macroscopic Young's modulus (E), and Poisson ratio. This may be obtained by considering the few case in which an infinite number of facets surrounds one aggregate piece.

In the LDPM formulation, there is the kinematically constrained like the microplane model, that are without deviatoric/volumetric split of the normal strain component. Under these guesses one can write:

$$E_o = \frac{1}{1-2v} E \Leftrightarrow E = \frac{2+3\alpha}{4+\alpha} E_o$$

and:

$$\alpha = \frac{1-4v}{1+v} \Leftrightarrow v = \frac{1-\alpha}{4+\alpha}$$

These relations can be obtained by the kinematically constrained homogenization of a random assemblage of the rigid spherical particles of various sizes interacting through elastic contacts. The eqs. can be used for estimate the LDPM elastic parameters in correct way, starting from macroscopic experimental measuring of Young's modulus and Poisson's ratio.

Inelastic behavior

In this section the aim is to define the formulation of the non linear and inelastic part of the constitutive law, that is characterized by three different physical mechanisms of mesoscale behavior:

   a) Fracturing and cohesive behavior.

   b) Pore collapse and material compaction under high compressive stress.

   c) Frictional behavior.

Fracturing and cohesive behavior

The fracturing behavior is present for tensile normal strain when it is $\varepsilon_N > 0$. As has just done in other papers publishing, is better to do, one kind of formulation

that put in relationship the effective strain and effective stress, that are expressed by the following relations. This is convenient for formulate the fracture and damage evolutions. The principal relations are:

$$\varepsilon = \sqrt{\varepsilon_N^2 + \alpha\left(\varepsilon_M^2 + \varepsilon_L^2\right)} \qquad \sigma = \sqrt{\sigma_N^2 + \frac{\left(\sigma_M + \sigma_L\right)^2}{\alpha}}$$

The relation used as effective strain, is similar to the strain measured used in the interface element model of Camacho and Ortiz (1996), and supply a total measure of the material straining. The normal and shear strain can be calculated from effective and shear strain using the following relation, in a way similar to simple damage models:

$$\begin{cases} \sigma_N = \sigma\dfrac{\varepsilon_N}{\varepsilon} \\[2mm] \sigma_M = \sigma\dfrac{\alpha\varepsilon_M}{\varepsilon} \\[2mm] \sigma_L = \sigma\dfrac{\alpha\varepsilon_L}{\varepsilon} \end{cases}$$

The effective stress σ, is incrementally elastic, $\dot{\sigma} = E_0\dot{\varepsilon}$ and have to respect the inequality $0 \le \sigma \le \sigma_{bt}(\varepsilon,\omega)$, where the E_0 is the effective strain that is one of LDPM parameters.

In according with the Cusatis (2008) the strain dependent boundary $\sigma_{bt}(\varepsilon,\omega)$, may be written as:

$$\sigma_{bt}(\varepsilon,\omega) = \sigma_0(\omega)\exp\left[-H_0(\omega)\frac{\langle\varepsilon_{max} - \varepsilon_0(\omega)\rangle}{\sigma_0(\omega)}\right]$$

In which the brackets $\langle\bullet\rangle$ are used in Macaulay sense: $\langle x\rangle = \max\{x,0\}$.

These relations, are used for describe the elastic-softening concrete domain when it is over tension stress, looking the relation is possible understand how when the $\varepsilon_{max} > \varepsilon_0$, the strength drop for the softening effect, see Fig. 1.12.

Now every behavior is summarized into the total domain of LDPM model, that is characterized by ω, the internal variable. This is written as following:

$$\tan\omega = \frac{\varepsilon_N}{\sqrt{\alpha}\varepsilon_T} = \frac{\sigma_N\sqrt{\alpha}}{\sigma_T}$$

that is characterized by the ratio between normal strain ε_N and the total shear strain ε_T, obtained in this way $\varepsilon_T = \sqrt{\varepsilon_M^2 + \varepsilon_L^2}$, or equivalently using the ratio into the normal stress σ_N and the total stress, so defined as $\sigma_T = \sqrt{\sigma_M^2 + \sigma_L^2}$.
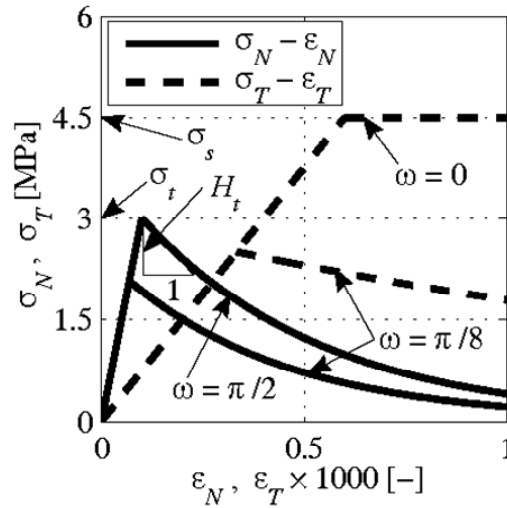
**Figure 1.12: Tensile behavior, changing
the internal parameter ω**

The inelastic behavior σ_{bt} is commanded with the exponentially relation, that also represent the boundary in the total domain, as a function of the maximum effective strain, which is a history dependent variable defined as:

$$\varepsilon_{max} = \sqrt{\varepsilon_{N,max}^2 + \alpha \varepsilon_{T,max}^2}$$

where:

$$\begin{cases} \varepsilon_{N,max}(t) = \max_{\tau<t}[\varepsilon_N(\tau)] \\ \varepsilon_{T,max}(t) = \max_{\tau<t}[\varepsilon_T(\tau)] \end{cases}$$

are the value of maximum normal and total shear strain, that are present during the loading history. It is worth noting that in absence of unloading $\varepsilon_{max} \equiv \varepsilon$.

The point over the boundary in the total domain, are decrypted by the function $\sigma_0(\omega)$ that is the strength limit for the effective stress and is defined as:

$$\sigma_0(\omega) = \sigma_t \frac{-\sin(\omega) + \sqrt{\sin^2(\omega) + 4\alpha \cos^2(\omega)/r_{st}}}{2\alpha \cos^2(\omega)/r_{st}}$$

where: $r_s = \sigma_s/\sigma_t$ represent the ratio among the shear strength σ_s, and the tensile strength σ_t. In the total domain, or stress space $\sigma_N - \sigma_T$, the equation previously present describe a parabola with its axis coincident with the σ_N − axis.

The transition between the two fields (elastic and inelastic domain) occurs, when the maximum effective strain achieves its elastic limit $\varepsilon_0(\omega) = \sigma_0(\omega)/E_0$, in this circumstances, the boundary σ_{bt} start to decay in exponential way. The speed of this decaying is governed by the post peck slope (softening modulus), that is considered to be a power function of the internal variable ω:

$$H_0(\omega) = H_t \left(\frac{2\omega}{\pi} \right)^{nt}$$

Using this expression it is possible to have a smooth transition, from the softening behavior subject to pure tensile stress ($\omega = \pi/2$, $H_0(\omega) = H_t$), to perfectly plastic feature under pure shear ($\omega = 0, H_0(\omega) = 0$). For avoiding problems with the dissipation energy during the mesoscale damage localization, this expression is used for the softening modulus in pure tension: $H_t = 2E_0/(l_{cr}/l - 1)$, and where G_t represent the mesoscale fracture energy, $l_{cr} = 2E_0 G_t/\sigma_t^2$, and l is the length of the tetrahedron edge associated with the current face.

Poor collapse and Material Compaction

Another typically inelastic behavior is present when the concrete is under high compressive hydrostatic deformations, in this set is possible to see one strain-hardening plasticity. This plastic field really can be divide into two different phases, the first is connected with the pores collapse under load and a second phase, when the pores are closed, and this give to the concrete structure one major density. Computing these two effect, in terms of stress-strain response, is showed for the first problem, one sudden decrease of the stiffness, that is in the second stage regained with a rehardening behavior.

Experiments show that after the densification phases both the tangent plastic stiffness and the unloading elastic stiffness, can be even higher than the initial elastic stiffness, in the rehardening phase. However, in the case of present of a significant deviatoric deformations, the rehardening phase result limited or sometimes also negligible, this really produce a horizontal plateau in the measured stress versus strain curve, Fig. 1.13.

The LDPM constitutive law, simulates this feature using a strain-dependent normal boundary $\sigma_{bc}(\varepsilon_D, \varepsilon_V)$, that is assumed function of volumetric strain ε_V and the deviatoric strain ε_D. These kind of deformation are computed respectively at the level of tetrahedron as $\varepsilon_V = (V - V_0)/V_0$, where V is the current volume and

V_0 is the initial volume of the basic element. For each tetrahedron there are twelve facets, for these is guessed that its are subjected at the same volumetric strain. Although, there is one think that change for every facets, this is the deviatoric strain characterized by several value. It computes as $\varepsilon_D = \varepsilon_N - \varepsilon_V$, where ε_N is the normal strain.

The definition of the volumetric and deviatoric strains are equivalent to the same quantities defined at each microplane in the microplane formulation.

The compressive boundary is expressed as function of $r_{DV} = \varepsilon_D/\varepsilon_V$ (deviatoric strain to volumetric strain ratio), that when assume constant value give at $\sigma_{bc}(r_{DV}, \varepsilon_V)$ an initial linear evolution (modeling the pore collapse) followed by an exponential evolution. It is possible to write:

$$\sigma_{bc}(\varepsilon_D, \varepsilon_V) = \begin{cases} \sigma_{c0} + \langle -\varepsilon_V - \varepsilon_{c0} \rangle H_c(r_{DV}) & \text{for} \quad -\varepsilon_V \le \varepsilon_{c1} \\ \sigma_{c1}(r_{DV}) \exp[(-\varepsilon_V - \varepsilon_{c1})H_c(r_{DV})/\sigma_{c1}(r_{DV})] & \text{otherwise} \end{cases}$$

where: σ_{c0} = yielding compressive stress, $\varepsilon_{c0} = \sigma_{c0}/E_0$ = volumetric strain at the onset of pore collapse, $H_c(r_{DV})$ = initial hardening modulus, $\varepsilon_{c1} = k_{c0} \varepsilon_{c0}$ = volumetric strain at which hardening begins, k_{c0} = material parameter governing the onset of hardening, $\sigma_{c1}(r_{DV}) = \sigma_{c0} + (\varepsilon_{c1} + \varepsilon_{co})H_c(r_{DV})$.

When there is a increment of r_{DV}, the slope of the initial hardening modulus needs to go to zero, in order to the simulate the observed horizontal plateau featured by typical experimental data. One way for obtaining this is the following:

$$H_c(r_{DV}) = \frac{H_{c0}}{1 + k_{c2}\langle r_{DV} - k_{c1} \rangle}$$

For compressive loading, the normal stress is calculated imposing the inequality $-\sigma_{bc}(\varepsilon_D, \varepsilon_V) \le \sigma_N \le 0$. Inside the domain, descript with the previously equation, the behavior is assumed to be incrementally elastic $\dot{\sigma}_N = E_{Nc}\dot{\varepsilon}_N$. In agree to the model the increased stiffness during unloading, the loading-unloading stiffness E_{Nc} is defined:

$$E_{Nc} = \begin{cases} E_0 & \text{for} \quad -\sigma_N < \sigma_c \\ E_d & \text{otherwise} \end{cases}$$

where E_d is the densified normal modulus. The Fig. 1.13 shows the typically hardening behavior for compression.
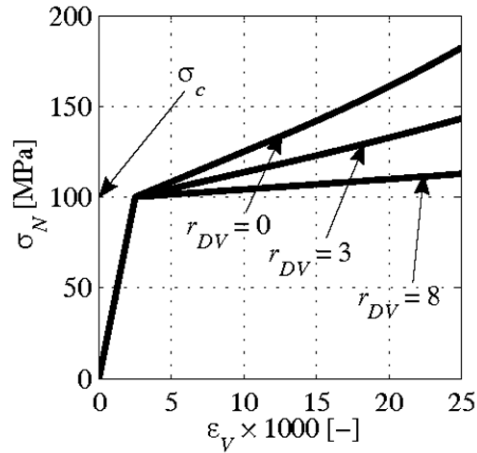
Figure 1.13: Elastic-hardening behavior under compression stress.

Frictional behavior

The concrete present when in compression stress stage one increasing of shear stress due the frictional effects, is possible to compute this effect using the classical incremental plasticity. The relation used for calculate the shear stress is the following:

$$\begin{cases} \dot{\sigma}_M = E_T\left(\dot{\varepsilon}_M - \dot{\varepsilon}_M^p\right) \\ \dot{\sigma}_L = E_L\left(\dot{\varepsilon}_M - \dot{\varepsilon}_L^p\right) \end{cases}$$

Where the plastic strain increments are assumed to obey the normality rule:

$$\begin{cases} \dot{\sigma}_M^p = \dot{\lambda}\,\partial\varphi/\partial\sigma_M \\ \dot{\sigma}_L^p = \dot{\lambda}\,\partial\varphi/\partial\sigma_L \end{cases}$$

The plastic potential is written as $\varphi = \sqrt{\sigma_M^2 + \sigma_L^2} - \sigma_{bs}(\sigma_N)$ in which shear strength σ_{bs} if formulated with a nonlinear frictional law:

$$\sigma_{bs}(\sigma_N) = \sigma_s + (\mu_0 + \mu_\infty)\cdot\sigma_{N0} - \mu_\infty\cdot\sigma_N - (\mu_0 - \mu_\infty)\sigma_{N0}\exp(\sigma_N/\sigma_{N0})$$

Where σ_s = cohesion, μ_0 and μ_∞ are the initial and final internal friction coefficients, respectively, and σ_{N0} = the normal stress at which the internal friction coefficient transitions from μ_0 to μ_∞.

Finally, equations governing the shear stress evolution must be completed by the loading-unloading conditions $\varphi\dot{\lambda} \leq 0$ and $\dot{\lambda} \geq 0$.

Numerical Implementation and Stability Analysis

The LDPM model, is implemented into one software called MARS (Modeling and Analysis of the Response of Structures), which is a multi-purpose structural analysis program based on a modern object-oriented architecture. The MARS uses one kind of the explicit dynamic algorithm for solving the analysis of structural problems. The dynamic algorithm take for the our problems is the central difference method, that is developed from central difference formulas for the velocity and acceleration. This is particularly important for the research presented in this model, because it is characterized by several thousands of degrees of freedom, and this permits to solve the problem using a standard computer, because it does not need more computational space. In any way the explicit scheme is not affected by the convergence problems that implicit schemes have in handling softening behavior. In fact, the explicit algorithms are not always stable, and these often need an accurate analysis on the numerical stability of the numerical simulation. In order to have the stability, it is possible to make this kind of approach. In the elastic regime, the stability condition may be expressed, with the respect of the following relation: $\Delta t < 2/\omega_{max}$. In this relation ω_{max} represents the highest natural frequency of the computational system. The first step, for ensure the stability is to find this value, is possible demonstrate that $\omega_{max} < \max(\omega_I)$, where the ω_I is the natural frequencies of the individual unrestrained elements composing the mesh used in the simulation.

Basically, the objective is to study every element and to find its natural frequency, then to take a higher value which will represent one limited for the our system. In this way is estimated ω_{max} , which will be contained in the range that see ω_I like last value. The second step will be to compute the time step, using this relation: $\Delta t < 2/\omega_I$, this procedure permits to avoid every instable convergence problem.

Knowing the correct time step, the following problem $\det(K - \omega^2 M) = 0$ is computed, where K is the stiffness matrix and M the mass-matrix. The elastic energy associated with the generic facet k is:

$$U_K = \frac{1}{2} l_e A_K \left(E_N \varepsilon_{Nk}^2 + E_T \varepsilon_{Lk}^2 + E_T \varepsilon_{Mk}^2 \right) = \left(K_{ij}^k + K_{jj}^k \right) Q_j + \left(K_{ii}^k + K_{ji}^k \right) Q_i$$

where:

$$K_{pq}^k = E_N \left(B_N^{pk} \right)^T B_N^{qk} + E_T \left(B_M^{pk} \right)^T B_M^{qk} + E_T \left(B_L^{pk} \right)^T B_L^{qk} \qquad (p, q = i, j.)$$

The total tetrahedron stiffness matrix is obtained by assembling the strain energy contributions of all twelve facet:

$$K = \sum_{k=1}^{12} K^k = \sum_{k=1}^{12} \begin{bmatrix} K_{ii}^k & K_{ij}^k \\ K_{ji}^k & K_{jj}^k \end{bmatrix}$$

where the symbol Σ is used to identify the assembly operation.

For a generic facet k, the kinetic energy associated is subdivided into two terms relative to the two nodes, that belonged at the facet. This may be showed in this way: $I_k = I_{ki} + I_{kj}$. Each individual term read as:

$$I_{ki} = \frac{1}{2} \int_{V_{kp}} \rho \dot{u}(x)^T \dot{u}(x) dV = \frac{1}{2} \dot{Q}_p^T \left[\int_{V_{kp}} \rho A_p(x)^T A_p(x) dV \right] \dot{Q}_p = \frac{1}{2} \dot{Q}_p^T \dot{M}_p^T \dot{Q}_p$$

where:

$$M_p^k = \rho \begin{bmatrix} V_{kp} & 0 & 0 & 0 & S_{kp}^z & -S_{kp}^y \\ 0 & V_{kp} & 0 & -S_{kp}^z & 0 & S_{kp}^x \\ 0 & 0 & V_{kp} & S_{kp}^y & -S_{kp}^x & 0 \\ 0 & -S_{kp}^z & S_{kp}^y & I_{kp}^y + I_{kp}^z & -I_{kp}^{xy} & -I_{kp}^{xz} \\ S_{kp}^z & 0 & -S_{kp}^z & -I_{kp}^{xy} & I_{kp}^x + I_{kp}^z & -I_{kp}^{yz} \\ -S_{kp}^y & S_{kp}^x & 0 & -I_{kp}^{xz} & -I_{kp}^{yz} & I_{kp}^x + I_{kp}^y \end{bmatrix}$$

The elements that appear in this matrix are: ρ = material density, V_{kp} = volume identified by the facet k and the node p. The others terms present in the matrix are: S = the volume first order , and I = the second order moments of the volume V_{kp} about the axes of the Cartesian system of the reference with origin at the node p. In the same way, the overall mass matrix is computed using the assemblage of the contribution for each facets:

$$M = \sum_{k=1}^{12} M^K = \sum_{k=1}^{12} \begin{bmatrix} M_i^k & 0 \\ 0 & M_j^k \end{bmatrix}$$

Chapter 2

Constitutive law for the concrete-fiber interaction

Introduction

Fibers, whose use can be traced back to the Roman Empire, are important to restrict and, in some sense, protect against the coalescence of microcracks, microvoids into wide cracks. Nowadays there are many types of materials with this structure among which Fiber-Reinforced Concrete (FRC) and the Engineered Cementitious Composites (ECC), whose function is exactly what I just pointed out.

The main function of fibers, besides giving a moderate increase to the tensile and compressive strength, is to ameliorate the energy transmission and absorption capability that is fundamental in resisting impacts and different kinds of shocks. More specifically fibers limit crack width and permeability and have a substantial impact in reducing corrosion risk, Begnini, Bažant, Zhou, Gouirand and Caner (2007).

Previous literature mainly focuses on uniaxial tension, Li et al. (1998), Nataraja et al. (1999), Ramesh et al. (2003). More recently, multiaxial loading models and experiments have been reported by Kullaa (1994), Nataraja et al.(1999), Grimaldi and Luciano (2000), Peng and Meyer (2000), Li and Li (2001), Kholmyansky (2002), Kwak et al. (2002), Cho and Kim (2003), Ramesh et al. (2003), and Kabele (2004), Yin et al. (1989), Traina and Mansour (1991), Chern et al. (1992), Pantazopoulou and Zanganeh (2001), Mirsayah and Banthia (2002).

The objective is to create one constitutive law that permits to describe the relationship between the bridging stress σ_f transferred across a crack and the opening of this crack w_f and apply it to the LDPM. In this way it include the effects of randomly dispersed fibers in order to simulate the behavior of fibers.

During the pre-processing phase, each individual fiber is inserted into the specimen volume.

Fibers positions and orientations are randomly generated, and the intersections between fibers and LDPM facets are detected.

The stress on each LDPM facet can be computed as:

$$\boldsymbol{\sigma} = \boldsymbol{\sigma}_c + \boldsymbol{\sigma}_f = \boldsymbol{\sigma}_c + \frac{1}{A_c} \sum_{f \in A_c} \boldsymbol{P}_f \left(w, \boldsymbol{n}_f, d_f L_{sf}, L_{lf} \right)$$

This relation assume a parallel coupling between the fibers and the concrete matrix. The elements present in this relation are: $\boldsymbol{\sigma} = \begin{bmatrix} \sigma_N & \sigma_M & \sigma_L \end{bmatrix}^T$, $\boldsymbol{\sigma}_c = \begin{bmatrix} \sigma_{Nc} & \sigma_{Mc} & \sigma_{Lc} \end{bmatrix}^T$, $\boldsymbol{P}_f = \begin{bmatrix} P_{Nf} & P_{Mf} & P_{Lf} \end{bmatrix}^T$, A_c = facet area, w_f = facet crack opening, d_f = fiber diameter, L_{sf} = short embedment length, L_{lf} = long embedment length, and $\boldsymbol{n}_f$ = fiber orientation with respect to the crack (facet) plane. The terms relative to the concrete stress are computed in according to the LDPM constitutive law.

Basically, this construction starts from modeling a single pull-out fiber behavior against the surrounding matrix. The relationship $\sigma = \sigma(w)$ can be then obtained by averaging the contributions from fibers with different embedment length and orientation across the crack plane. In the theory that is proposed in this study the following aspects are considered: two-way fiber debonding-pullout due to a slip-hardening interfacial bond, matrix micro spalling and also the Cook-Gordon effect.

This constitutive law will be used so to describe the concrete-fibers interaction behavior, into the LDPM. The idea used to achieve this aim takes the formulation proposed for E.H. Yang, S. Wang, Y. Yang and V.C. Li (2008), as a base, and develops this idea for the mesoscale approach. In the following sections, will be shown the analysis that starts from the single fiber pull-out and later takes into account the total effects that are present in the fiber feature. In the next chapter the constitutive load will be verified using the results that are available from the experimental tests.

Modeling of the single fiber behavior

A well-known technique to study fiber-matrix interfacial behavior is single fiber pull-out, Katz. A., Li V.C. (1996). In Fig. 2.1 is shown the typical pull-out curve. Three stages are identified: initial elastic stretching of the fiber free length, followed by debonding stage and at the end the pullout phase.
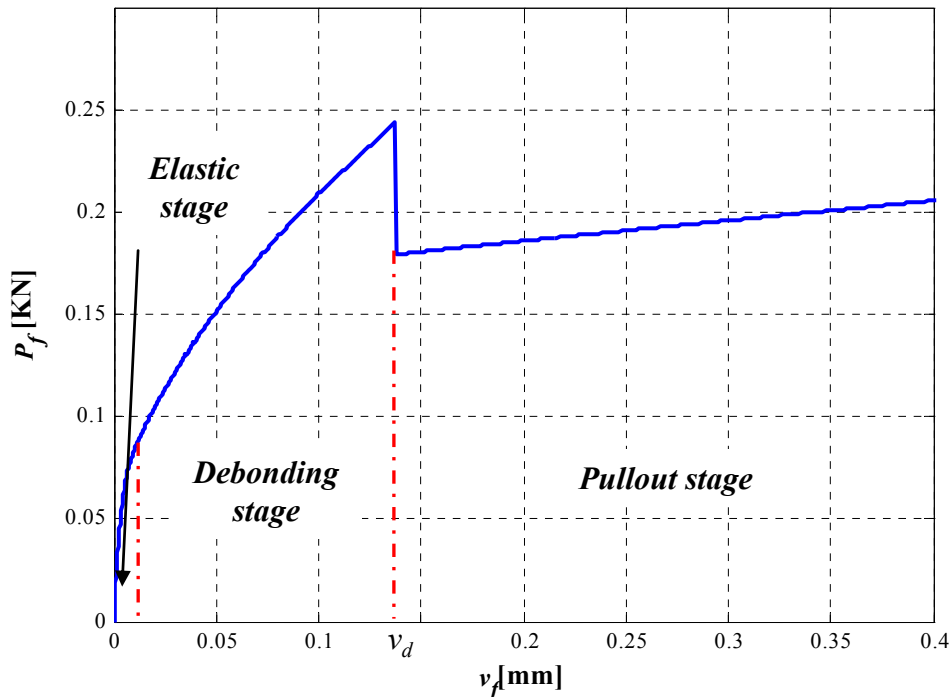

Figure 2.1: Single pullout curve of steel fiber.

The fiber in pullout first is subject to debonding before the pulling out phase takes place. Basically, this can be described as a crack propagation from the surrounding matrix crack to the embedded end. This stage lasts until there is the load drop, that represents the transition to the pull-out stage, when we are left just with frictional bond that can actually increase, whereas the chemical bond, that is present during this first stage, is lost. Stress analysis and energy balance process are used to model the debonding and the pullout of a single fiber. The following are the main assumptions of this model by Z. Lin, T. Kanda and V.C. Li (1999):

a) Fibers are high aspect ratios (>100), so that the final effect on the total debonding load is negligible;

b) During the debonding stage, the slip-dependent effect is negligible since relative slippage between the fiber and the matrix in the debonded portion is small. Hence, the frictional stress within the debonding zone remains at a constant τ_0;

c) Poisson's effect is negligible. For flexible fiber-cement systems, Poisson's effect is usually diminished due to inevitable slight misalignment and surface roughness of the fiber;

d) Elastic stretch of the fiber after complete debonding is negligible, compared with slip magnitude.

The relation between the load P_f and the displacement w is written. This is divided in two different equations, matched with the different stages present in the single fiber behavior. At each stage, the fiber extending across the matrix microcrack is always in equilibrium. It is possible to say that the force exerted on the short embedment side and the long embedment side are equal:

$$P_f = P_{sf}\left(v_{sf}\right) = P_{lf}\left(v_{lf}\right)$$

According to the previous statement, it is also true to declare that in absence of the different effects, the crack opening can be written as:

$$w_f = v_{sf} + v_{lf}$$

this is the case when the crack opening is done only by the fibers-matrix slippage. The crack opening, implemented into the code, is composed by three different contributions, given that the model allows to study 3d problems:
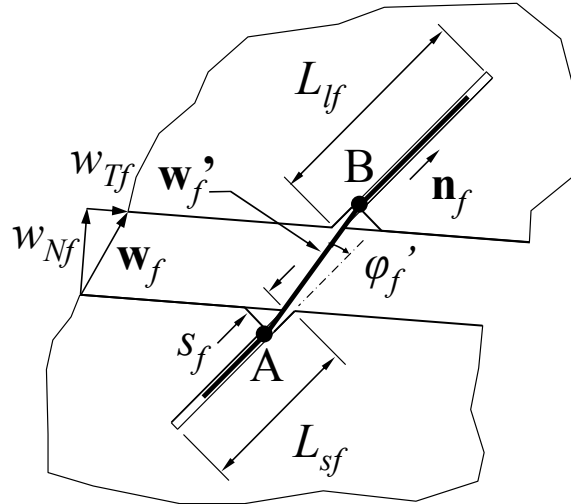
$$w_f = \left[w_{Nf}^2 + w_{Mf}^2 + w_{Lf}^2\right]^{1/2}$$

In this way, is identified the vector identifying the crack opening created only by the fibers slippage. This crack opening vector is the result by sum of the slippages values, later when the other effects will appear there will be a new crack opening vector, called w_f'. This will be different than w_f for direction and modulus. Considering a crack crossed by straight fiber (Fig. 2.2), characterized by the embedment lengths L_{sf} and L_{lf}. If one neglects the fiber bending stiffness and the elastic deformation of the crack-bridging segment, the length of such a segment (distance between points A and B in Fig. 2.2) can be computed as:

$$\boldsymbol{w}_f' = \boldsymbol{w}_f + 2s_f\boldsymbol{n}_f$$

where $w_f^{'}$ is the crack opening vector and s_f the reduction of embedment lengths due to micro-spalling.

**Figure 2.2: Schematic of inclined bridging
with matrix spalling.**

In additional, the fiber force con be assumed to be coaxial with the crack-bridging segment and expressed as:

$$\boldsymbol{P}_f = P_f \boldsymbol{n}_f^{'}$$

where: $\boldsymbol{n}_f^{'} = \boldsymbol{w}_f^{'}/w_f^{'}$ and $w_f^{'} = \sqrt{w_{Nf}^{'2} + w_{Mf}^{'2} + w_{Lf}^{'2}}$.

The Fig. 2.3 shows the best situation possible, characterized by fiber orthogonal to the crack plane. In this particular configuration the spalling and the snubbing, that will be later explained, are not present.
In the next section, will be explained how the crack opening vector changes according to the other effect that the fibers issue shows. The new effect that will be considered is Cook-Gordon effect. According to the change just show before, will be explained also the micro-spalling.
The different stages for a single fiber will be described using different relations that permit to find the link between $P_f - v$ and also $\sigma - v$. In this first step, the relation between force and crack opening will be analyzed, assuming that the pullout force is always applied orthogonal to the crack plane. Later on, the same analysis will be performed but looking at most common cases.

In the second step, the strength relations will be introduced. In this way the constitutive law is done.

$$P , v$$

$$L$$
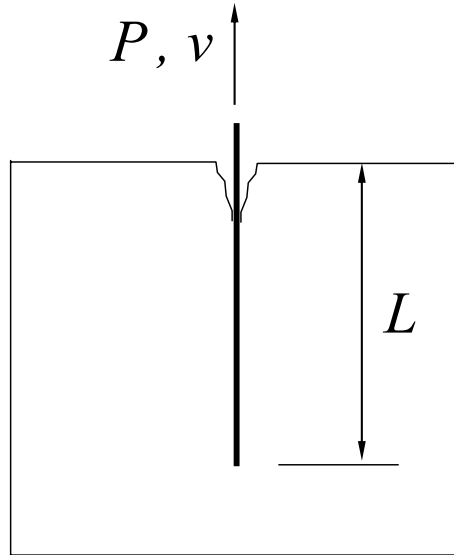
**Figure 2.3: Fiber pullout with force applied orthogonal
to the crack plane.**

Following the detailed derivation by the Z. Lin, T. Kanda and V.C. Li (1999), the equation for the debonding stage can be written as:

$$P(v) = \sqrt{\frac{\pi^2 \tau_0 E_f d_f^3 (1+\eta)}{2} v + \frac{\pi^2 G_d E_f d_f^3}{2}} \qquad 0 \le v \le v_d$$

where v_d is the crack opening that corresponds to the displacement at which full-debonding is completed, and it is expressed as:

$$v_d = \frac{2\tau_0 L^2 (1+\eta)}{E_f d_f} + \sqrt{\frac{8 G_d L^2 (1+\eta)}{E_f d_f}}$$

The elements that appear here are: $\eta = V_f E_f / V_m E_m$, this is a parameter expressing the ratio of the effective (accounting for the volume fraction) fiber stiffness to effective matrix stiffness, frictional stress τ_0 and debonding fracture energy G_d (also referred to as chemical bond). When the debonding phase is finished, it is possible to see a sudden drop due to unstable extension of the tunnel crack. Subsequently, the fiber is held back into the matrix only by frictional bonding.

The magnitude of the drop can be used to calibrate the chemical bond G_d. During the debonding and pullout stage, the fiber may rupture if the load P exceeds the fiber tensile strength. According to this effect, the study is developed under the assumption that the fiber rupture never happen.

The relation that describe the force in the pullout stage is:

$$P(v) = \pi d_f \tau_0 \left(1 + \beta \frac{(v - v_d)}{d_f} \right)(L - v + v_d) \qquad v_d \leq v \leq L$$

The different elements present in this equation, are shown in Fig. 2.4. It is also possible to write the equation for the debonding stage in terms of the debonding length. In this case the debonding load P can be also expressed as:

$$P(L) = \pi d_f \tau_0 L + \sqrt{\pi^2 G_d E_f d_f^3 / 2}$$

at the full debonding $L = L_e$. The maximum debonding load is given by:

$$P_a = P_b + \sqrt{\pi^2 G_d E_f d_f^3 / 2}$$

where $P_b = \pi d_f \tau_0 L_e$ is the initial friction pullout load. This equation allows calibrating the chemical bond strength G_d and the frictional bond strength τ_0, from the maximum debonding strength load P_a and the initial frictional pullout load P_b. The slip-hardening coefficient β, is obtained from the relation that is used for the pullout stage.
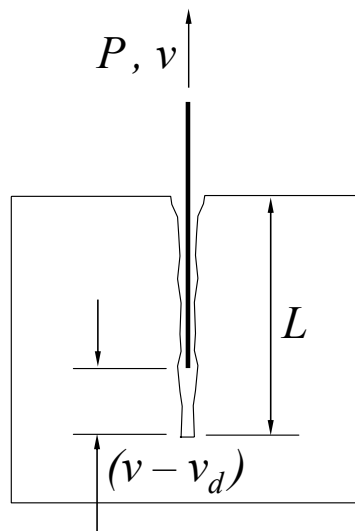
Figure 2.4: Slippage effect and variable of the problem

β is the parameter that controls the behavior in the tall of the curve $P_f - v$. It can be hardening or softening according to the kind of fiber used in the specimen. These simple relations are the building blocks to construct the constitutive law for composite material like fibers-concrete. The next step will be the writing of the relations in terms of strength and displacement.

The single fiber-bringing stress $\sigma_{debonding}$ versus the fiber displacement (at exit point) relative to the matrix crack surface v is given by:

$$\sigma_{debonding} = 2\sqrt{(\tau_0 v + G_d)\frac{2E_f(1+\eta)}{d_f}}$$

where E_f and d_f are fiber Young's modulus and diameter, respectively of fiber. After the debonding is completed, the fiber is in the pull-out stage. In this stage, there is one load drop that represents the absence of chemical bonding. Here the strength is guaranteed by its frictional bond only. For some types of fibers, particularly PVA fibers, significant slip-hardening response was observed during long-range pullout. Assuming the linearity of the frictional stress with respect to the slip distance with the coefficient β (referred as slip-hardening coefficient , Lin, Z. and Li, V.C. (1997), the fiber stress $\sigma_{pullout}$ during the pullout stage can be expressed as:

$$\sigma_{pullout} = \frac{\tau_0}{d_f}\left(L_e - v - v_d\right)\left(1 + \frac{\beta(v - v_d)}{d_f}\right)$$

In the short fiber composite system, most fibers are oriented to an arbitrary angle φ relative to the crack plane, which takes values in the range of $0 \div \pi/2$, with $\varphi = 0$ for fibers perpendicular to the plane and $\varphi = \pi/2$ for fibers parallel to the plane. Furthermore, the interaction with the matrix, when this last one exits the fiber puts the fiber under further stress. Specifically for the polymeric fiber as Morton and Groves (1979) and Z. Lin, T. Kanda and V.C. Li (1999) suggest the following holds:

$$P_f = P_{sf}\left(v_{sf}\right)e^{k_{sn}\varphi_f'} = P_{lf}\left(v_{lf}\right)e^{k_{sn}\varphi_f'}$$

Where $k_{sn} > 0$ is referred to the snubbing coefficient. This relation accounts the increase of bridging force P_f due to an inclination angle φ by making analogy to an Euler friction pulley at the fiber exit point. As shown in Fig. 2.5, at the exit point, i.e. where the fiber begins to protrude beyond the crack face, there is a kink

in the fiber. At this point, the matrix acts as a "frictional pulley". This phenomenon is typically called "snubbing effect".
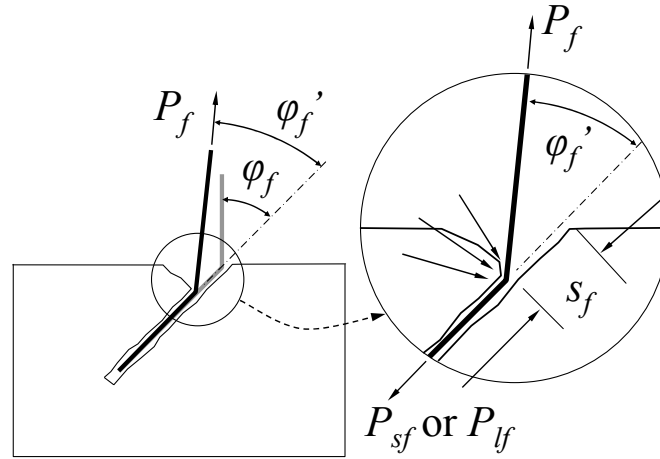

Figure 2.5: Snubbing effect geometry.

Moreover different fibers reacts differently to bending and lateral stress. For instance, in order to study this effect, for the PVA fiber, Kanda and Li (1998) introduced a strength reduction coefficient:

$$\sigma_{fu}(\varphi) = \sigma_{fu}(0)e^{-k_{rup}\varphi}$$

where σ_{fu} is the ultimate tensile strength of the fibers associated with the theoretical situation where the fiber's bridging segment and its embedded segment are collinear, and k_{rup} is a material parameter.

Basically the previously relation can be written also in term of force. The previously equations are valid only if the fiber force does not cause fiber rupture. This can be checked by making sure that the fiber force magnitude is less than the rupture force:

$$P_f < P_{uf} = 0.25\pi d_f^2 \sigma_{uf} e^{-k_{rup}\varphi_f'}$$

Until this point I just tries to illustrate and explain the fibers behavior. Later on in my work I will focus on three important aspects: two-way fiber pullout, spalling effect and the Cook Gordon effect, according with E.H. Yang, S. Wang, Y. Yang and V.C. Li (2008).

Matrix micro-spalling

An issue that should be taken into account is the misalignment of the pullout force with the orientation of the embedment segments at the fiber exit (Fig. 2.2). This is called, matrix micro-spalling, common in the case of random fiber reinforced brittle matrix composites, as PVA-ECC, Kanda and Li (1998).

For the definition of the spalling length, s_f, various models have been proposed in the literature, including Cailleux et al (2005) and Leung & Li (1992). Herein, the formula proposed by Yang et al. (2008) is adopted.

The spalling length, expressed as a function of external load on the fiber, matrix strength, matrix stiffness, and inclination angle influences the size of the spalled matrix piece, that is estimated through the following equation:

$$s_f = \frac{P_{fN} \, sen\left(\varphi/2\right)}{k_{sp} d_f \sigma_t \cos^2\left(\varphi/2\right)}$$

where P_{fN} is the normal component of the external force acting on the fiber, φ is the fiber inclination angle, σ_t is the matrix tensile strength, k_{sp} is a dimensionless constant related to the fiber geometry and matrix stiffness, calibrated through experimental observation and called spalling parameter.

This specification, typical of LDPM, allows to consider the inclination crack, that is not possible by simply following Yang, S. Wang, Y. Yang and V.C. Li (2008) that only consider crack opening normal to the crack plane.

In the above specification, the spalling size is considered as proportional to the external load on the fiber exit and inversely proportional to the matrix tensile strength and fiber diameter.

For typical forces in PVA, fiber in ECC, the predicted spall size (for $k_{sp} = 3000$), is in the range of the $0 - 28 \mu m$, consistent with those observed experimentally.

Matrix micro-spalling has an impact on stress concentration on strengthen bridging fibers and on the fiber inclination angle φ to a smaller φ'.

In a PVA-ECC fiber, the spalling size s_f ranges from several micrometers to fiber diameter. Moreover, starting from a steady-state crack width of $60 \mu m$, the maximum elastic stretch of the fiber segments freed from spalling will not exceed $2 \mu m$ at the peak load, which is negligible compared without significant influence on the modeling of single fiber-bridging behavior with consideration of both two-

way pullout and matrix spalling can be reduced to the problem of two-way pullout with a modified $w_f^{'}$, as is just shown before.

Cook-Gordon effect

The Cook-Gordon effect is linked to the tensile stress exerted on a blunt matrix describes a premature fiber/matrix interface debonding normal to the fiber axis caused by a tensile stress located ahead of blunt matrix crack propagating towards a fiber under remote tensile load as depicted in Fig.5.
In the Fig. left is represented the induces fiber-matrix separation due to the tensile stress in the horizontal direction associated with the elastic crack tip field of the approaching matrix crack. Whereas the Fig. on the right leads to an additional crack opening v_{cg} due to elastic stretching of the fiber segment.
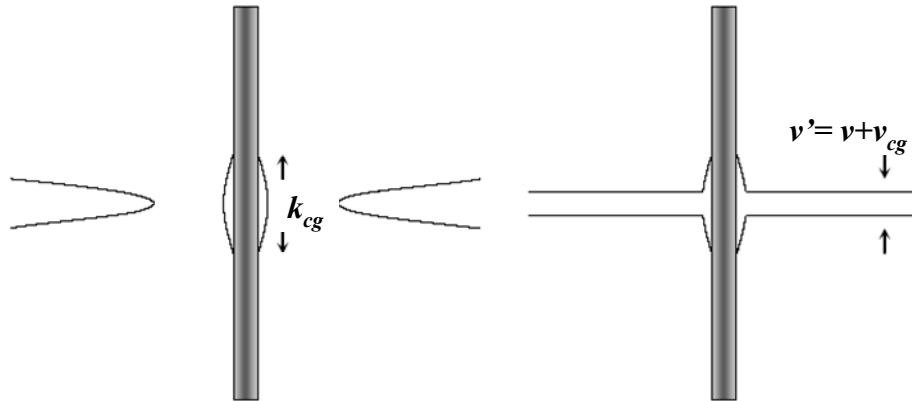

Figure 2.6: Cook Gordon effect.

In other words, we have the stretching of a free fiber segment k_{cg} (Cook-Gordon parameter), and additional crack opening v_{cg}, as shown in Fig. 2.6, due to debonding ahead if the matrix crack. Following Li at al: (1993), v_{cg} can be directly computed from the bridging force P_f for all fibers without considering the orientation.
Therefore, for a single fiber, the formula for the additional displacement is the following:

$$v_{cg} = \frac{4k_{cg}P_f}{\pi d_f^2 E_f}$$

When P_f is independent of φ and z, the integration of next relation gives the number of fibers bridging across the crack per unit area times P_f.

$$\sigma_f = P\frac{A_f}{V_f}\int p(z,\phi)dzd\phi \equiv PN_B$$

where N_B, the number of fiber-bridging across the crack per unit area, is:

$$N_B = \frac{A_f}{V_f}\int p(z,\phi)dzd\phi = \frac{A_f}{V_f}\eta_B$$

and

$$\eta_B = \int p(z,\phi)dzd\phi$$

this is the efficiency of bridging in terms of the amount of fiber bridging across a crack with respect to orientation effect. The $P - v_{cg}$ relationship for the single fiber, can be written also in this way:

$$v_{cg} = \frac{k_{cg}\sigma_f}{V_f E_f \eta_B}$$

In this way, the fiber-bridging stress σ_f is computed as a function of the numerical procedure for calculating the bridging stress vs. crack opening displacement relationship.

Two way pullout

Once the crack opening takes place, the short embedment side of the fiber debonds. It is the pullout of this side that leads to an increase of the crack opening itself. Infact, at this point, the long embedment side is characterized only by an elastic stretch whose influence on the crack opening is minimal. Of course, the effects is different according to the type of fiber. Specifically for the PVA one, Redon and Li (2001) suggests that slip-hardening of PVA fiber in cement matrix is due to abrasion and to the jamming effect during the slip stage.

The embedment length is also important: when it is small the fiber is completely pulled out from the matrix, whereas when the length is large there is a rupture of the fiber. Moreover, it should be pointed out, that the significant slip-hardening behavior causes the pullout load to be larger at full debonding rather than at the completion of the debonding.

Looking at PVA fibers, we can witness a two-way fiber pull-out process, given that, when the short embedment sides goes through bridging, it is the long embedment side that starts the pull-out stage. This feature makes necessary, to have a complete and not biased picture, to include the effect that the slip displacement coming from both sides of the fiber has on the total crack opening $w_f^{'}$. Wang et al (1988) were the first to suggest this two-way fiber pullout, shown in fig. Later, I will describe the different phases in more details.

Analysis stages

The aim is to divide the different stages and to analyze every stages so to have a complete picture of the problem. For each stages, the fiber is assumed to be no orthogonal to the crack opening, the snubbing and spalling effects for this reason will be always present. In this study, nothing will be said about these effects, the attention will be focus only on the two way pullout behavior.

Stage 1: neither embedment ends completely debonded

In this stage, the crack opening v is started and the fiber begins to work. Here the magnitude of the crack opening is really and the relation that allows to write the compatibility equations is $v = v_{lf} + v_{sf} = 2v_{sf}$, where v_{lf}, v_{sf} are respectively the slippage in the long and in the short embedment fiber. In this stage, $v_{sf} = v_{lf}$, because both sides are in the debonding stage. The next subsection shows how the

passage to the short embedment length in the pullout stage will change the above relation. It will also show that the slippage will significantly increase in this stage. For the debonding stage, the equation used to express the relation $P_f - v$ is the following:

$$P_f = \sqrt{\frac{\pi^2 \tau_0 E_f d_f^3 (1+\eta)}{2} v + \frac{\pi^2 G_d E_f d_f^3}{2}} \qquad 0 \le v_f \le v_{df}$$

applied to both sides until there is complete debonding in the short side (Stage 2):

$$v_{df} = \frac{2\tau_0 L_s^2 (1+\eta)}{E_f d_f} + \sqrt{\frac{8 G_d L_s^2 (1+\eta)}{E_f d_f}}$$

where L_s is the length for the short fiber. This is an assumption already seen in previous literature. It states that the pullout stage is achieved first in the short side and later in the other side. However, the fiber is always in equilibrium: the force in the fiber is independent of the embedment length, Yang at al. (2008). For a given crack opening v, the contribution v_L and v_S from the long embedment segment (length L_{lf}) and the short embedment segment (length L_{sf}), respectively, can be calculated from the fiber load balance. The upper bound on v for this stage can be defined as:

$$v_f < 2 v_{df}$$

where v_d is the crack opening relative to the completely debonding for the short side

Stage 2:short embedment end complete debonded

In the new stage the short embedment length is at full debonding and the force suddenly weakens. Therefore, the bonding embedment is lost. However, the friction effect is still present and it also allows increasing the force in this stage. It should be noted that, if the frictional pullout is a hardening process, the P_f will increase until it reaches the value needed to debond the long side. Mathematically, this stage can be depicted using the following equations:

$$v_{lf} < v_{dlf} = \frac{2\tau_0 L_l^2 (1+\eta)}{E_f d_f} + \sqrt{\frac{8 G_d L_l^2 (1+\eta)}{E_f d_f}}$$

$$v_{sf} > v_{dsf} = \frac{2\tau_0 L_s^2 (1+\eta)}{E_f d_f} + \sqrt{\frac{8 G_d L_s^2 (1+\eta)}{E_f d_f}}$$

and the following relations are used to describe the problem for the force:

$$P_{lf} = \sqrt{\frac{\pi^2 \tau_0 E_f d_f^3 (1+\eta)}{2} + \frac{\pi^2 G_d E_f d_f^3}{2}}$$

$$P_{sf} = \pi d_f \tau_0 \left(1 + \beta (v_s - v_{sd})/d_f\right)\left(L_s - v_{sf} - v_{sdf}\right)$$

where v_{sd} corresponds to the displacement at which full-debonding is completed and it is given by:

$$v_{sdf} = \frac{2\tau_0 L_s^2 (1+\eta)}{E_f d_f} + \sqrt{\frac{8 G_d L_s^2 (1+\eta)}{E_f d_f}}$$

The equilibrium in the fiber is assured in this way:

$$P_{ld}\left(v_{fl}\right) = P_{sp}\left(v_{sf}, L_s\right)$$

Stage 3: both embedment ends completely debonded

In this last stage, the debonding is achieved for both sides of the fiber that is in pullout stage. The relations that describe this stage are:

$$v_{lf} > v_{dlf} = \frac{2\tau_0 L_l^2 (1+\eta)}{E_f d_f} + \sqrt{\frac{8 G_d L_l^2 (1+\eta)}{E_f d_f}}$$

$$v_{sf} > v_{dsf} = \frac{2\tau_0 L_s^2 (1+\eta)}{E_f d_f} + \sqrt{\frac{8 G_d L_s^2 (1+\eta)}{E_f d_f}}$$

In this phase the relation for the crack opening changes, and the new form is:

$$v_{lf} + v_{sf} + 2s_f = v_{eff}$$

Where s_f is the spall size that is included in the frictional pullout equation. It reduces the length of "cylinder", where the fiber is in frictional contact with the "tunnel". The term that includes β, which provides the magnitude of the frictional stress and which is dependent upon the occurrence of the relative slip between the fiber and the tunnel, does not change.

$$P_{ps} = \pi d_f \tau_0 \left(1 + \beta\left(v_{sf} - v_{sdf}\right)/d_f\right)\left(L_s - v_{sf} - v_{sdf}\right)$$

$$P_{pl} = \pi d_f \tau_0 \left(1 + \beta\left(v_{lf} - v_{ldf}\right)/d_f\right)\left(L_l - v_{lf} - v_{ldf}\right)$$

Parameters analysis of the model

The constitutive law implemented into the LDPM will be studied to check and understand how the different parameters allow to modify the curve form for fiber pullout.

The single pullout fiber will be evaluated trying to change the values of the main parameters, that have a crucial impact on the way the fibers react. With this in mind, the several cases studied are: pullout force applied in the same fiber direction and not (present of spalling effect), different values for β (pullout hardening behavior), a geometrical study about the two different embedment lengths for the fiber, that bring the phenomenon of two way pullout and several more. In additional, the geometry of the problem is investigated. In this way taking fixed the parameters values, is studied how the fiber position affect the response. In brief, looking also at the findings of previous literature, for each of these cases just described, I will develop and test several hypotheses on the reaction behavior of the fibers.

Presentation of fiber parameters

The LDPM-F model for the fibers is governed for the 11 parameters. These ones are:

E_f = Elastic Modulus;

k_{sp} = Spalling Parameter;

σ_f = Fiber Strength;

k_{rup} = Fiber Strength Decay;

k_{sn} = Snubbing Parameter;

τ_0 = Bond Strength;

η = Volume Stiffness Ratio;

G_d = Debonding Fracture Energy;

β = Pull Out Hardening;

k_p = Plastic Parameter;

k_{cg} = Cook-Gordon Parameter;

The next paragraphs will be a discussion on the most important parameters, and the main effects of this constitutive law. The idea is to hypothesize the effect

connect to the different parameters, and then to check if the hypothesizes done are corrects. In this way the law is checked over.

Pullout hardening behavior

The fiber behavior after complete debonding is characterized by the presence of a sudden drop of the load caused by the lost of the chemical bond. In the next stage, called pullout phase, the fiber response can change significantly according to the kind of fiber used in the specimen.

Several previous works showed that these parameters can be ranged into $-1 < \beta < 1$. The idea is to try now to change each parameter and to check that the reply the one expected. The behavior can be referred as softening when $\beta < 0$ or hardening $\beta > 0$.

This kind of test is not affected by the fiber position respect to the crack plane. According to this aspect, the test is realized using one fiber positioned orthogonal to the crack plane, therefore the pullout force is applied coaxial to the fiber direction. This problem configuration is shown in the Fig. 2.3.

It is defined as linear when $\beta = 0$. This is shown in the following image:
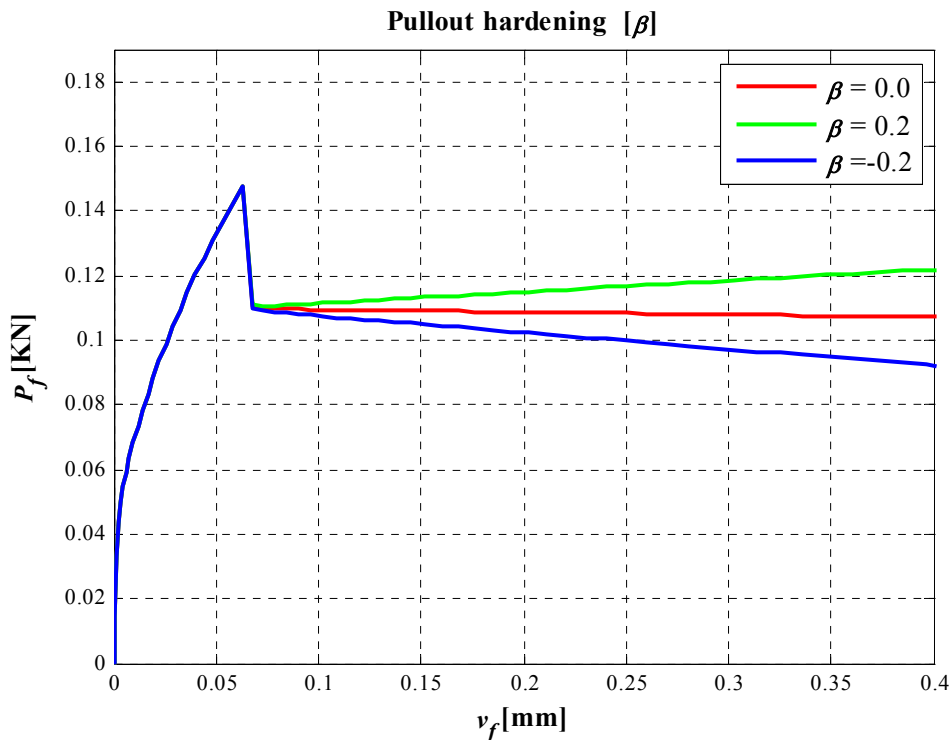
Figure 2.7: Influence of the pullout parameter on single fiber pullout curve.

Clearly this kind of parametric analysis is done, fixing the other parameters equal to zero, in this way the results are not affected by mixed of different phenomenon. Basically the pullout effect can be divided into three different groups. On of this, is shown a linear behavior, the remaining two are a no-linear trend.

Two way pullout

This effect is not matched with the parameters changing. The purpose is to understand how the two way pullout change the response of the fiber. As already said in this chapter, the fiber is always in equilibrium for both the debonding and pullout stages. The only difference is that in the short embedment length the full debonding crack opening is achieved before the long side, this shows that the slippage in the short time is bigger than the long side. Now in order to check that the model allows for a good description of this aspect, the test done will change the two embedment length. The tests will have embedment length very different in the first stage (v_f^*), and almost equal in the second test v_f.
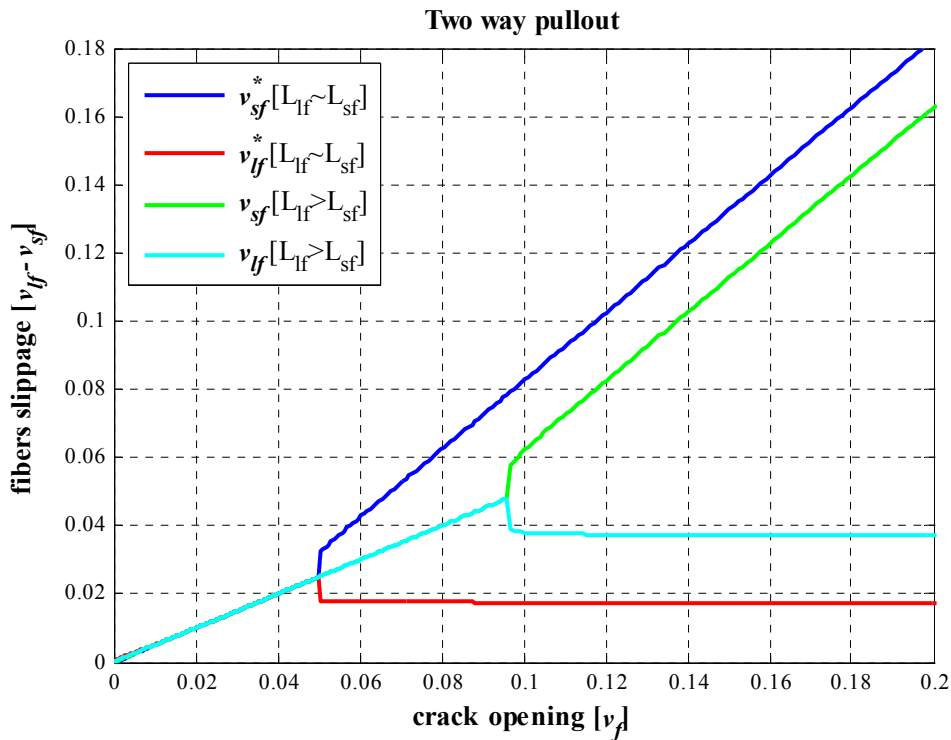
Figure 2. 8: Two way pullout behavior due to the different embedment lengths.

The result expected is that in the test v_f the slippage for the two sides is the same until the full debonding crack opening is achieved, after the test v_f^*. When this

limit for the both tests is achieved, it is possible to see how to change the slippage magnitude in the short and length embedment sides.

Debonding fracture energy

In this analysis, the aim is to investigate the effect of the debonding fracture energy (G_d). How is already said in this chapter the fiber can be in two different stage: debonding and pullout.

When the fiber pass from debonding to the pullout stage is possible to see a sudden drop in the force. The magnitude of the drop is directly proportional to the value of G_d.

The approached used is to try several values of G_d and will check if the results expected will be captured from the model. The results obtained prove how increasing the value of G_d the drop increase. It is also shown one increasing in the force peak. This is reasonable because with a bigger value of G_d in the fiber is so increasing the force that is brought.
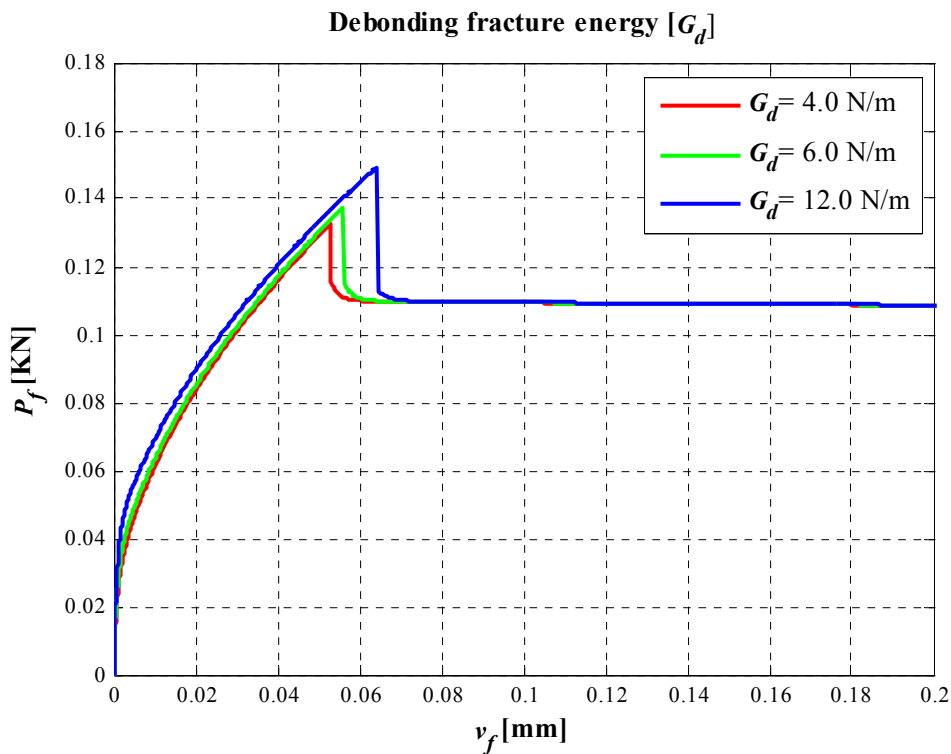
Figure 2. 9: Influence of the Debonding fracture energy on single fiber pullout curve.
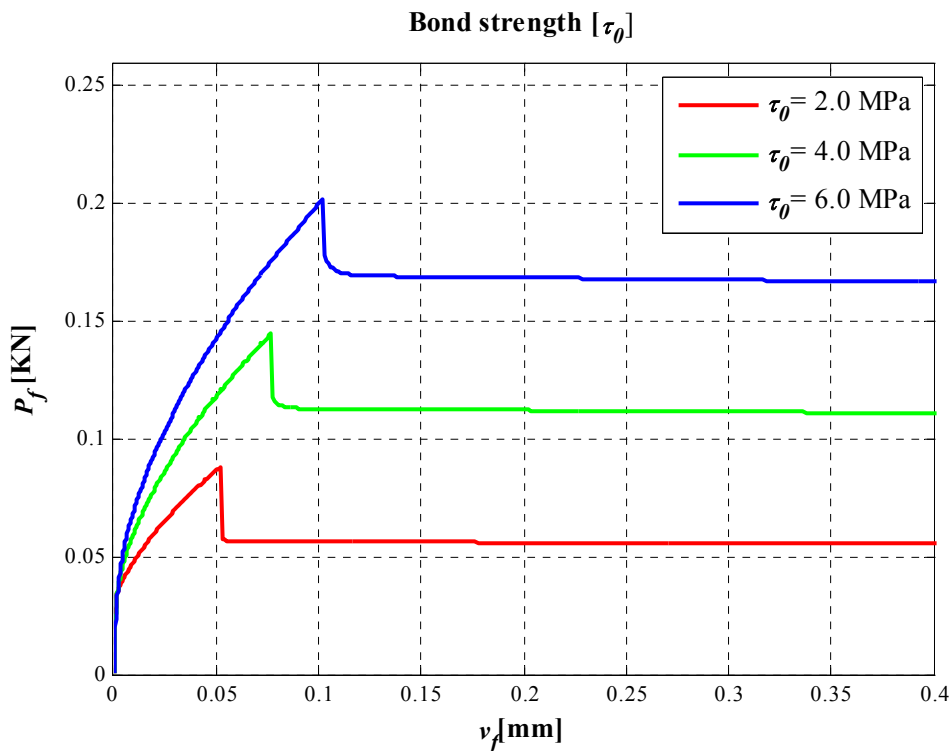
This parameter is also not affected by fiber position. The angle realized between fiber direction and pullout force is not important to the analysis of the problem.

The parameters that are important for considering this angle are: spalling parameter and snubbing effect. They are shown later.

Bond strength

The bond strength τ_0 is a crucial parameter and it is matched with the frictional force, that it is assumed to be constant in the debonding stage. This parameter appears in both the relations for P_f. It not only affects the elastic slope but also the peak force. Notably, its effect is more clear after the post peak, where the fiber is held in the concrete matrix only by the frictional strength. Starting from this idea, the value of the bonding strength will be increased step by step and later the results will be checked. As the graph shows the results found are in line with the expectations.


Figure 2. 10: The curves show how the single fiber pullout is affected by bond strength.

This parameter is not affected by the fiber inclination respect to the pullout force direction. According to this, the single fiber is positioned orthogonal to the crack opening plane.

Snubbing effect

The snubbing effect is present when the angle ϕ between the fiber and force direction is different from zero. This phenomenon shows how the force brought by the fiber increases in this new configuration. We expect that the P_f value, particularly at the peak, increases with k_{sn} fixed, and changes only the ϕ angle. Using this approach, the force increases when the angle becomes larger. In this study, three values of angle will be used. The graph shows that again findings are in line with expectations.
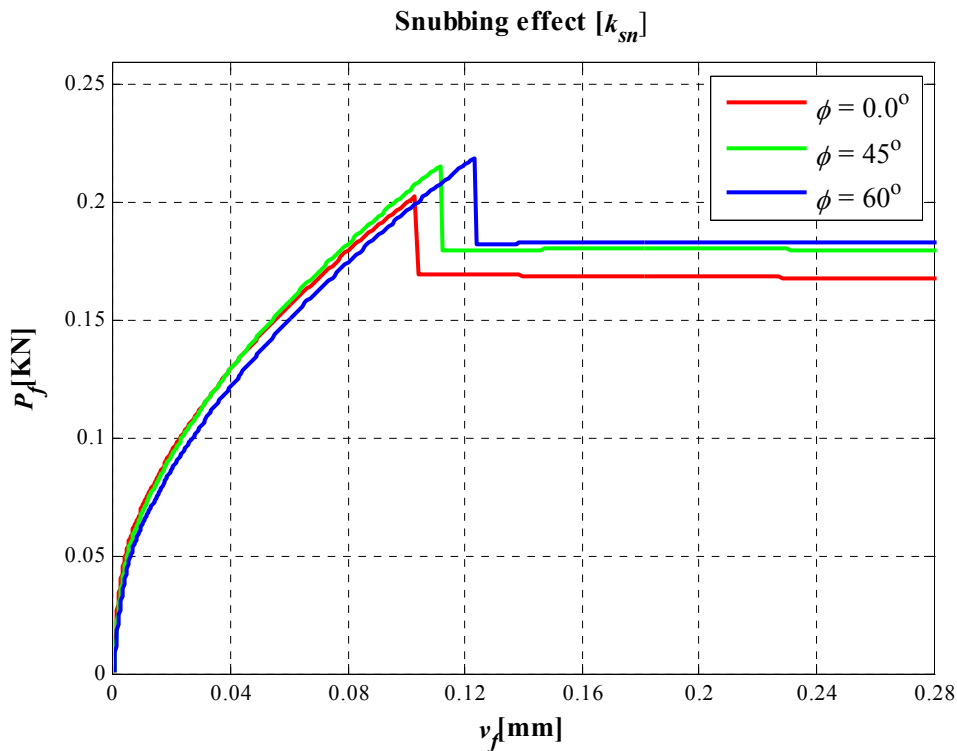
Figure 2.11: Different response for snubbing effect caused by fiber orientation.
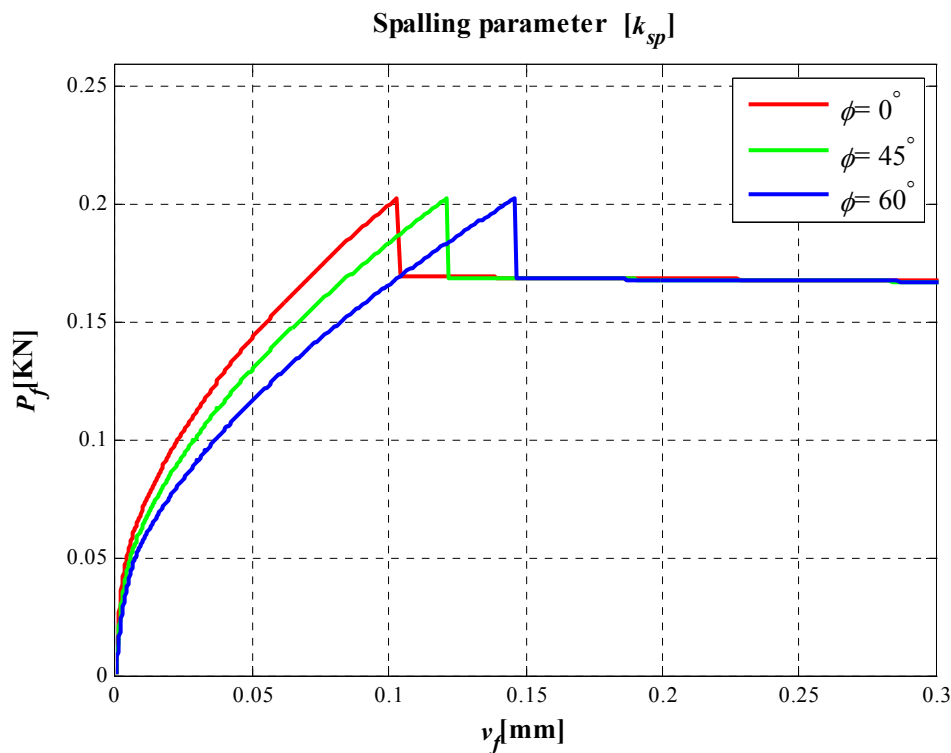
According to this figure, the snubbing parameter has the same trend fixing the angle and increasing the value of the parameter. This parameter will be very important in the next chapter, when the model will be calibrated. It allows to fit the peak.

Spalling effect

The spalling effect is present when the angle ϕ between the fiber and force direction is different from zero (Fig.4). This phenomenon shows how the embedment length of the fiber is subject to one reduction caused by the rupture of the concrete matrix close to the fiber exit.

The behavior will be the same in terms of force sustained, but I expect that the full debonding crack opening will be achieved earlier than in the case without spalling.

Thus, three different values of the angle will be used. We expect that the value, in particularly at the peak, increases with the fixed, and a change in the angle. Using this approach, the force increases when the angle is larger. In this study, three values of the angle will be used. As expected, when the angle value increases, the full debonding crack opening is achieved earlier.

**Figure 2. 12: Different response for spalling effect
caused by fiber orientation.**

The spalling parameter is too important in the processing phase because it determines the spalling length. According to this factor, the crack opening vector changes, and for this reason also the pullout force that the fiber can bring.

The inverse relation between spalling length and spalling parameter is important. In fact, the increasing of spalling parameter produces one reduction in the spalling length.

Chapter 3

Numerical analysis plain concrete subject to tension and compression

Introduction

In this chapter will be explained how to calibrate the LDPM in order to fit the experimental results by Laps (Bologna), Buratti at al (2008). Following this idea, initially will be studied the 3PBT (three point bending test) and UC (uniaxial unconfined compression test) just focusing on the concrete.
After that, in the next chapter, when the concrete is already calibrated, the fibers will be introduced in the specimens.
The first calibration is done using the common mesostructure values of parameters, shown in previous works. Starting from here, will be run one parameter study to understand as the different parameters affect the model.
The experience sais that usually there is no linear relationship among the different parameters. In order to obtain the best possible calibration, the following tests should be run: uniaxial unconfined compression, three point bending test, triaxial shear test and hydrostatic compression test. In such a way it will be possible to capture each kind of concrete behaviour: compressive and shear-tensile response.
Is a common procedure not to run each one of these tests. It is enough to run two tests related to the study of the tensile and compression behaviour.
The approach followed is aimed at calibrating how the model reacts to a change in the parameters for each type of available test while using for the rest of parameters the common values found for other kind of concretes.
The structure will be as follow. I illustrate the calibration procedure first and then I will analyze the different topics matched with the LDPM model.

Presentation of the parameters

The Lattice Discrete Particle Model (LDPM) is governed by the 16 meso-structural parameters, that allow to describe the concrete behaviour. In the next chapter will be introduce additional parameters, specifically used for the fibers calibration in addition to the previous one. The parameters used for the fibers calibration that will be add to these. For the concrete calibration the parameters are:

- E_0 = Normal Modulus;
- E_d/E_0 = Densification Ratio;
- α = Shear-normal coupling parameter;
- σ_t = Tensile Strength;
- σ_c = Compressive Strength
- σ_s/σ_t = Shear Strength Ratio;
- l_{cr} = Tensile Characteristic Length;
- n_t = Softening Exponent;
- H_c = Initial Hardening Modulus Ratio;
- $\varepsilon_{c1}/\varepsilon_{c0}$ = Transitional Strain Ratio;
- μ_0 = Initial Friction;
- μ_∞ = Asymptotic Friction;
- σ_{N0} = Transitional Stress;
- β = Volumetric Deviatoric Coupling;
- k_1 = Deviatoric Strain Threshold Ratio
- k_2 = Deviatoric Damage Parameter.

Model sensibility

The LDPM allows to reproduce the concrete behaviours, showing tension, compression behaviour and also the shear effect. It will involve tests replicating both behaviours. Through these experimental tests, will be study few parameters. For calibrate the model all kind of test for the same concrete need. In this way will be able to fit each parameter. Using this approach, will be shown the parameters that affect the test behaviour for 3PBT and UC. However, I will refer to the precious works done in this field, in order to have a clear idea about the different values ranges in which the parameter fluctuate and for understand what kind of

parameter affect my test. In the recent years, the following links test parameters were identified:

- Tensile test: the elastic part is linked with the E_0 and α. The peak is moved by σ_t and the inelastic part is a function of l_{cr} that allows to change the post-peak slope and σ_t, important in order to move the curve tail;

- Uniaxial unconfined compression test: E_0 and α represent the principal parameters needed to fit the elastic part. The peak is governed σ_t, σ_s/σ_t and μ_0. The post-peak by σ_t and l_{cr};

- Hydrostatic compression test: the elastic part is function of E_0 and α. The limit pressure value of the elastic behaviour by σ_c, the initial slope of the hardening part by H_c.

Looking at the previous literature according to Mencarelli (2007):

- For tests like tensile and the uniaxial unconfined compression the curve is scaled proportionally to σ_t out of the elastic part (peak and post-peak);

- l_{cr} does not allow to scale in proportional way the curves out of the elastic part for the tensile and uniaxial unconfined compressive tests;

- The ratio between the value of the peak of the Uniaxial Unconfined Compression Test and the value of the peak of the tensile test is governed by the σ_s/σ_t;

- The σ_c is the parameter that allows to scale the curve out of the elastic part for the hydrostatic test;

Phases of the calibration

Two types of tests are available in order to calibrate the LDPM only for the concrete. The tests used are 3PBT and UC. The calibration will be done, starting from the 3PBT Afterwards, will be checked if the results found in this first phase are in line with the experimental data for the UC test.

The difficulty of this calibration is the non-linearity of relationship among parameters. The final aim, then, will be that to find a fir compromise among successive calibrations, so to account for and understand the nonlinearity of the problem. The following section is divided into different subsections according to the different steps needed to perform the calibration.

Specimens geometry

The specimens used in these tests are the beam and the cube respectively for 3PBT and UC. In general the approach is always characterize by these three phases, as I pointed out already in the first chapter of this work. In this subchapter the first stage will be explained. Basically, the Mars requires the only dimension of the specimen that can be directly assigned, when it has a common shape, as it is done for the UC test.

Three point bending test (3PBT)

The approach used for the 3PBT specimen is completely different from the one usually done. There are two main reasons: the beam is realized with the notch in the middle of the span, making the specimen geometry a no-easy shape.
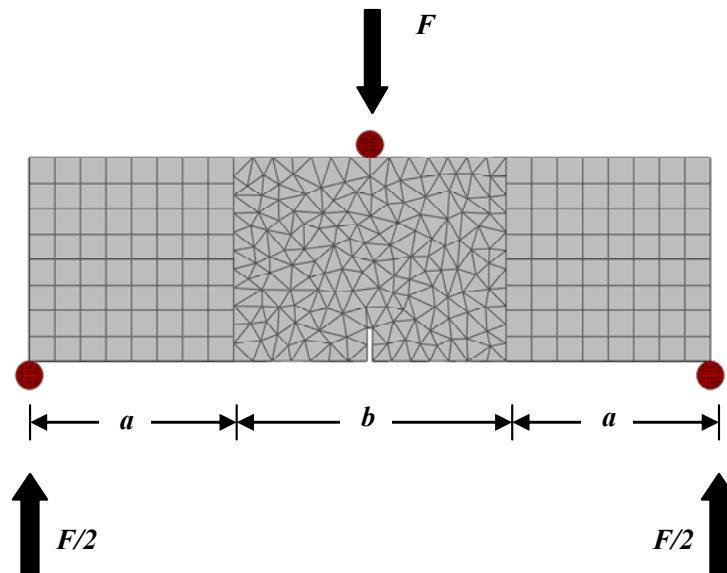

**Figure 3.1: Three point bending test specimen geometry.**

The Mars allows to overcome this problem, by referring to the nodes coordinate of the solid that will be used later on in the second stage. The second problem that affect this test is the specimen dimension. The beam used has one span of 500 mm and the sectional area is 150x125 mm, in the middle section where the notch is present.

In order to reduce the computational cost and to take into account that all cracks are in the central area, where the notch is done, the beam is divided into three zones. The two areas near the supports, indicated with *a* in the Fig. 3.1, will be realized with finite element. The central part, called *b* is the "LDPM volume". The dimensions of these regions are: *a*=150mm and *b*=200mm.

These dimensions are found according to the possibility cracks opening distribution, helping to get better clear scenario. In this way it is possible to realize a good numerical test without spending a lot of time, because the number of the particles has been reduced. The Fig. 3.1 shows the beam used in my test.

Uniaxial unconfined compression test (UC)

Cube, cylinder and prism are the common shapes of specimen used in this test. These specimens are positioned between a top and a bottom plate, where the vertically compression is applied by the top plate with no lateral confinement.
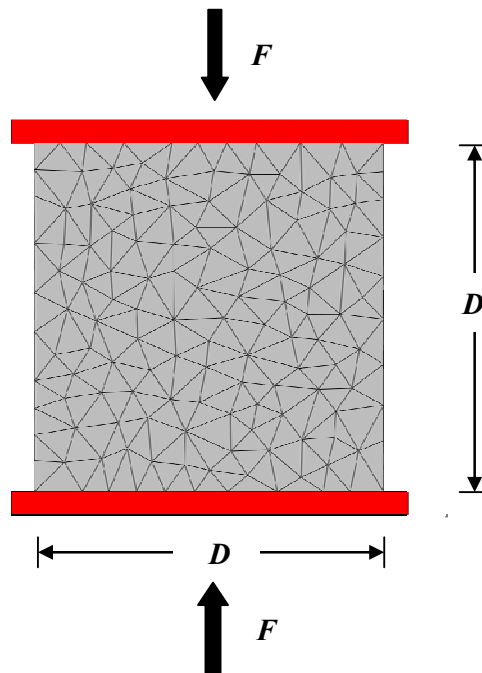
Figure 3.2: Uniaxial unconfined compression specimen.

In my test, the specimen used is a cube of dimension 150x150x150mm. The characteristic used for the contact plate-specimen is high friction; in the

experimental analysis sometimes this effect is reduced putting Teflon or an oil layer between the plate and the specimen. The Fig. 3.2 shows the specimen used. This volume will be later filled with the particles defined in the following subchapter. The image shows a triangle construction, that is realized in the last stage, when the particles and the zero-nodes are positioned into the volume, leading to the Delaunay triangulations is done.

Aggregate generation

The composition of the concrete, used into the LDPM model, is simulated starting from the parameters of the mix design. This is very important in order to reproduce the mesostructure of the concrete.

The tables present in the Buratti N. at al (2008) show the concrete mix used in the Laps tests, this will be an obvious starting point. According to these tables, it is possible to rebuild the Fuller curve, that is expressed by this equation:

$$F = \left(\frac{d}{D_{max}} \right)^n$$

where *n* is the Fuller coefficient, that will be estimated. This function allows me to describe the granulometric distribution of the particles. By performing a study on the principles parameters, it is possible to find this distribution.

The principles parameters are: the cement content *c* (mass/cubic length), the water to cement ratio *w/c*, the aggregate cement ratio *a/c*.

At this stage, the main aim is to define the concrete characteristic and the diameters range used to generate the particles that the LDPM will use to fill the specimen volume. Basically, only the coarse aggregate are reproduced, these are defined as the particles with characteristic size greater that 5 mm. It should be noted that, in order to obtain a reasonable computational time, the whole sieve curve cannot be simulated and, therefore, very small size aggregates must be discarded. According to this idea, the range 10-22 mm is used in my simulations. This choice allows to respect the two criteria fundamentally empirically. First of all, later different years of simulation is been found that covering the 30% of the total Fuller curve. I am able to define one mixed design that allows to obtain good results, that are not affected by the choice itself. Different percentage coverages are considered, but given some slight difference in the results, the 30% is defined as the best value in terms of quality of reaction and computational time cost. The characteristics used in my test are:

- Cement Content = 357 kg/m3
- Water To Cement Ratio = 0.49;
- Aggregate To Cement Ratio = 5.02;

- Min Aggregate = 10 mm;
- Max Aggregate = 22 mm;
- Fuller Coefficient = 0.5131;

The following image shows the estimated Fuller curve, where the green part represent the percentage simulated
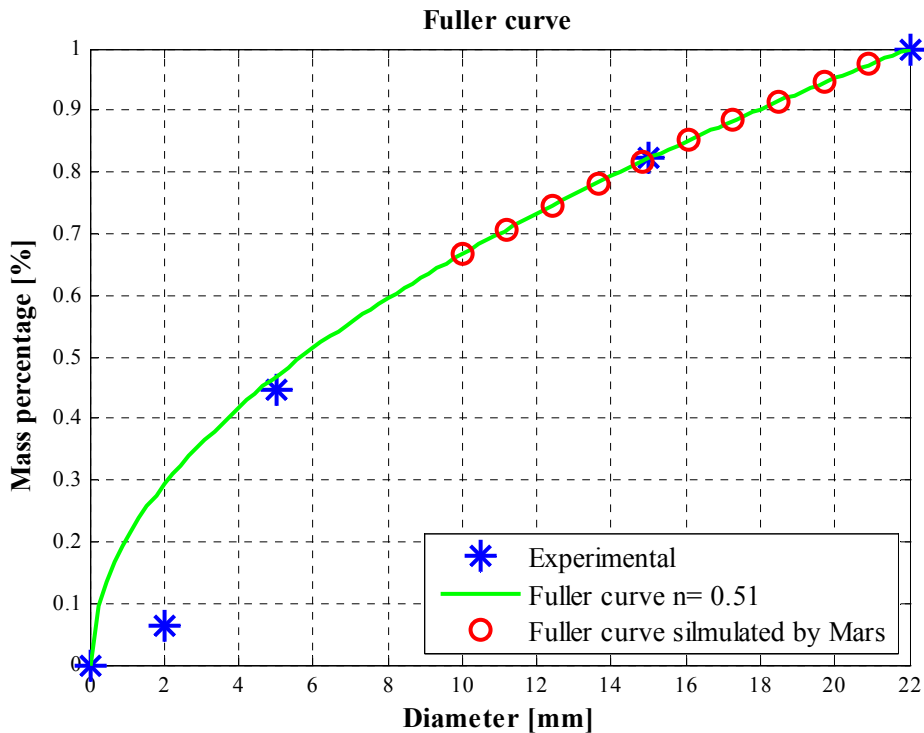

Figure 3.3: Computed sieve curve.

The generation phase ends by positioning the particles into the specimens. This is done by using a random algorithm that replaces the particles according to the command "seed". The seed is assigned into the mars input file, and allows to simulate the concrete randomness structure as well. This will be very interesting in the calibration stage, where the results will be affected by seed. this is in line with experimental date with the experimental data, where a scatter is always present for the same materials specimens.

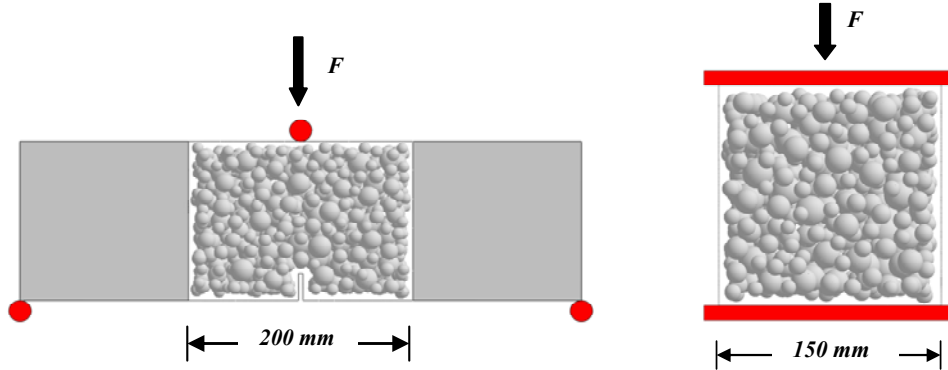At the end of this study, the specimens appear in this way:

**Figure 3.4: Specimens fill with the
generate particles.**

Parametric analysis

The LDPM, as pointed out before, is governed by 16 parameters. These parameters are needed in analyzing of the concrete and in capturing the compressive and shear-tensile behaviour.

The parameters will be calibrated according to the experimental tests available. The experience say that the principal parameters that affect these two tests are: tensile strength σ_t, shear-strength ratio σ_s/σ_t, tensile characteristic length l_{cr} and initial friction μ_0. The reaming parameters affect strongly the others kind of tests, whereas, in my tests, they imply just a small change in the results.

The main objective is to take averaged values of each of the parameters and then start studying them. In this way, I will be able to fit one concrete that can represent a good response also to other types of behaviour, for which the analysis cannot be performed.

Basically, it is important understand how these parameters change the responses of the model. According to this goal, a parameter study is done. This is the reason why sometimes it is possible to run one test, for instance 3PBT, but lose the good calibration specific for the UC. In general, to have a good fit, is needed is to achieve a balance among the different effects.

Three point bending test (3PBT)

The 3PBT is a test dominated by tension where a load is applied vertically in the middle of a simple support beam specimen of span *l* with or without notch in the central section. The aim is to obtain the force-Crack Mouth Opening

Displacement (CMOD) curve, where the two magnitudes are measured respectively in the point where the load is applied and at the extremes of the CMOD, when the notch is done. In other situations, the displacement considered is vertically measured in the same point where the force is applied.

The rupture starts vertically from the center of the specimen, where the notch is realized or in this central area when is without the notch. In this case, the area under the force-displacement curve divided by the area of the ligament is defined like the Fracture Energy G_f.

The 3PBT can be calibrated, by focusing the attention on two main parameters, that are know to affect more this kind of test. The parameters are: σ_t (tensile strength) and l_{cr} (tensile characteristic length). In order to this kind of approach, this parametric analysis is done:
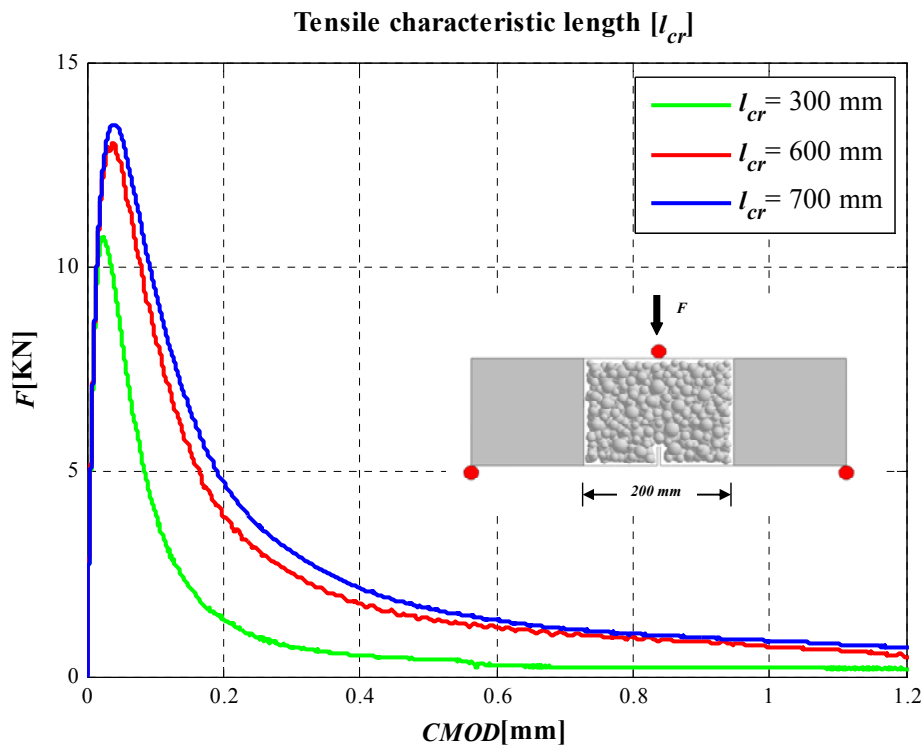
**Figure 3.5: Tensile characteristic length analysis for 3PBT
on plain concrete specimen.**

In this first image, is shown how the tensile characteristic length l_{cr} affects the peak and the slope for the plastic stage and, then, the position of tail curve. According to these results, this parameter will be used to estimate the post-peak slope and then when this portion of the curve become fixed of curve is fixed the peak will be found. The peak is moved using other parameters. The image allows to understand how only one parameter affect different parts of the curve and also the behaviour. It is important to keep in mind this, because often changing a

parameter to fit one part of the curve, would imply a change in another portion that was fixed before. This can be very expensive in terms of computational time. The tensile strength σ_t is another important factor that is used for the 3PBT. By varying this, according to its three values realized, the results obtained are:
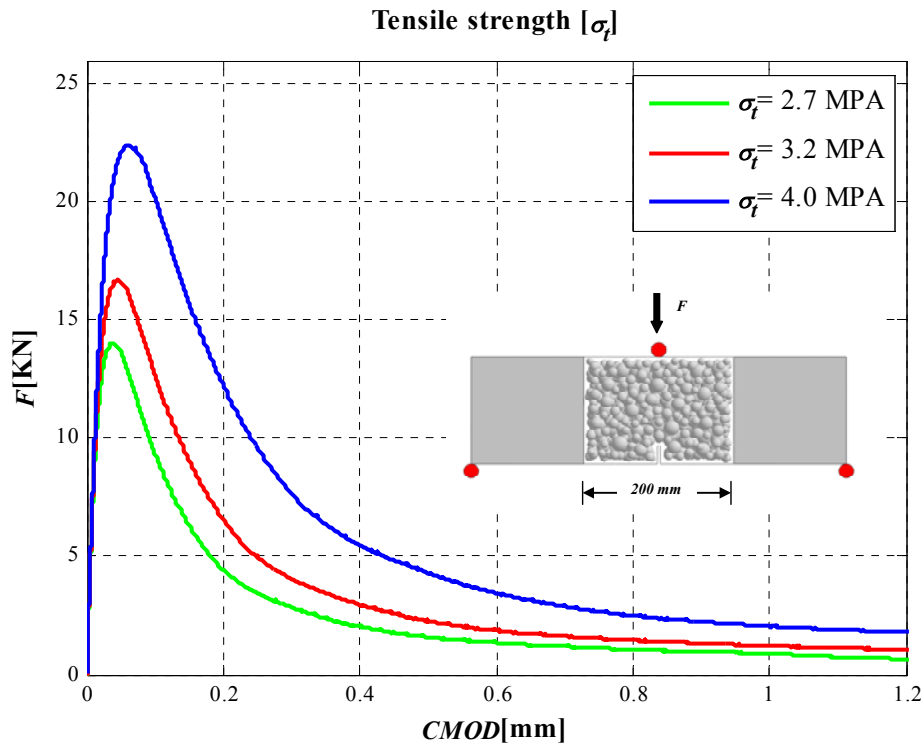
Figure 3.6: Tensile strength analysis for 3PBT on plain concrete specimen.

In this case, the tensile strength appears like a parameter that affect only the peak, and no-effect are shown for the post-peak slope. It allows to scale the curve out of the elastic part.

As expected, by increasing the tensile, the strength increased the peak and at the same time also the curve tail went up.

The method used for the calibration has been the following: starting from the 3PBT and then I tried for different values of these two parameters. Later on in the study, when a good fit is achieved, the same parameters for the UC behaviour will be checked.

How was clear to aspect the results found in this stage, was not good also for the UC.

With this in mind, I re-start my analysis by checking for what values there is a good fit in the UC test, which has to be done by using shear strength ratio and initial friction. These changes affect also 3PBT. Thus, in order to explain this type of behaviour the following analyses are run:

Initial friction [μ_0]

Figure 3.7: Initial friction analysis.

Shear strength ratio [σ_s/σ_t]

Figure 3.8: Shear strength ratio analysis.
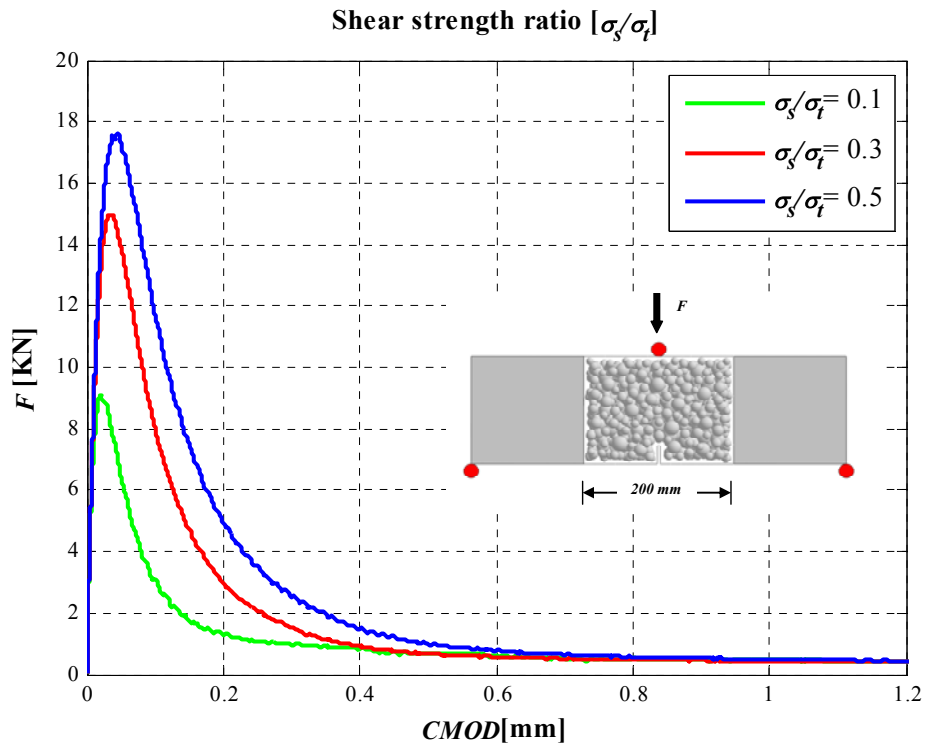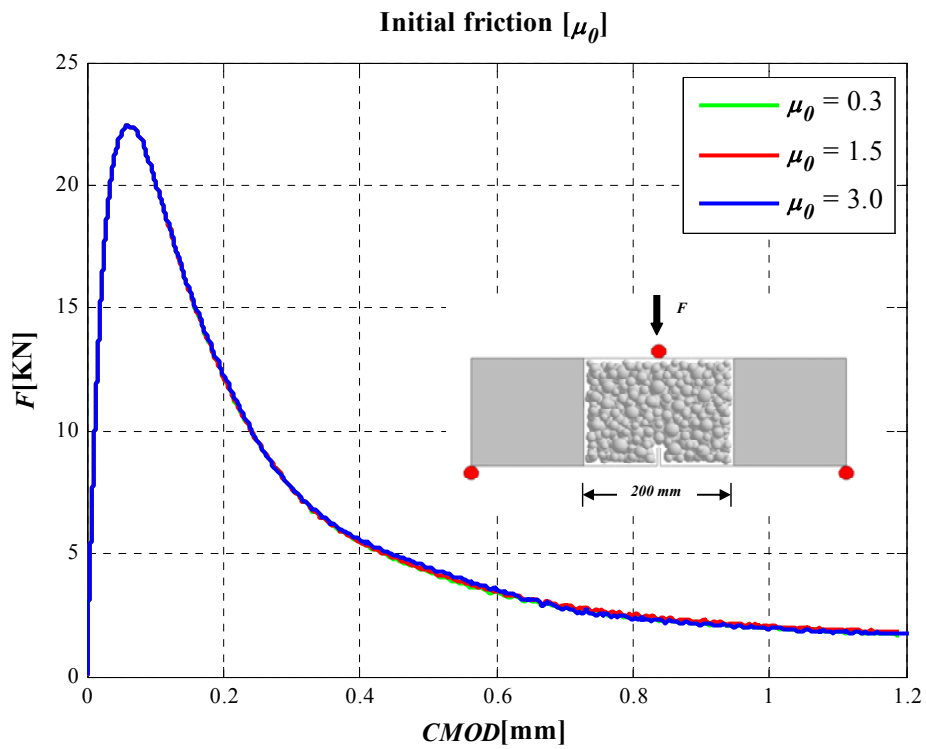
The initial friction μ_0 does not affect the 3PBT and will be used later on to fit the pick in the UC test. Notable, this goal is achieved also by using the shear strength ratio σ_s/σ_t. This completely changes the curve, as it is shown in the next figure.
Moreover this parameter is important for the triaxial test. For this reason it is preferred not to change this parameter value. Therefore, the common value shown by the experience is used.
Notable, in order to solve the calibration problem and to cover UC and 3PBT experimental results, the initial friction will be used for the UC test. The next sub-section show how these parameters affect the UC test.

Uniaxial unconfined compression test (UC)

It is a test where a prismatic, cubic or cylindrical specimen positioned between a top and bottom plate is compressed vertically by the top plate with no lateral confinement. For the prismatic and cylindrical specimen, the ratio between the dimension of the side L, of the square section or the diameter D of the circular section and the height H is usually 1:2 or 1:3. In both cases, the height of the specimens helps to decrease the confinement because the effect of the boundary plate does not influence the behaviour in the central part of the specimen for the De Saint Venant effect.
Cube specimens are used in my tests. The goal is to obtain the stress- strain curve, that is found to divide the force and the displacement, as measured on the plate for the area of the section and for the height of the specimen. The rupture response is matched with the level of confinement and can be explosive in the case of high friction.
Basically, the problem linked with the calibration stage, was to take the pick. This can be achieved by using with shear strength ratio σ_s/σ_t and the initial friction μ_0.
The elastic slope is already knew by the Bažant relations, that are the only relations that create a link into macro-parameters and meso-parameters. The results found changing different values for these parameters are the following.
The first parameter used to fit the peak was the shear strength ratio σ_s/σ_t, from the parametric study is possible to see how, by increasing it, the value the peak goes down. The experience also says that there is a linear match into the value of this parameter and the compressive strength. According to this, it is possible to fit the curve, making a linear study.
This method will create a problem into the 3PBT curve, because this kind of test is strongly influenced by the shear strength ratio.
The solution used is to work with the initial friction that does not change the results found in the 3PBT. The sensibility of this parameter is shown in the Fig. 3.10.
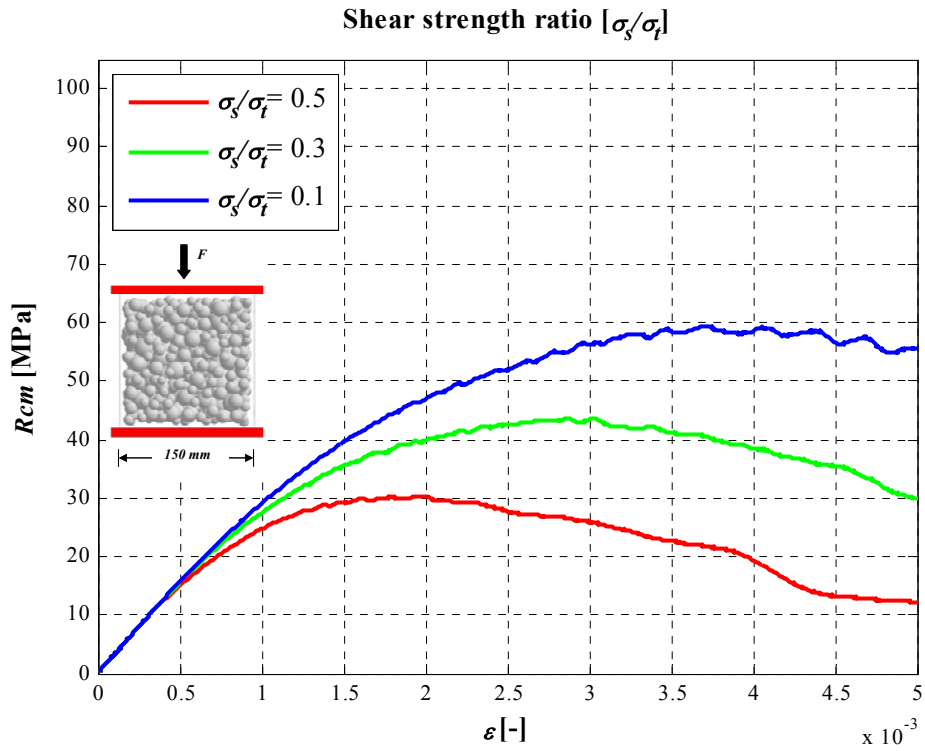
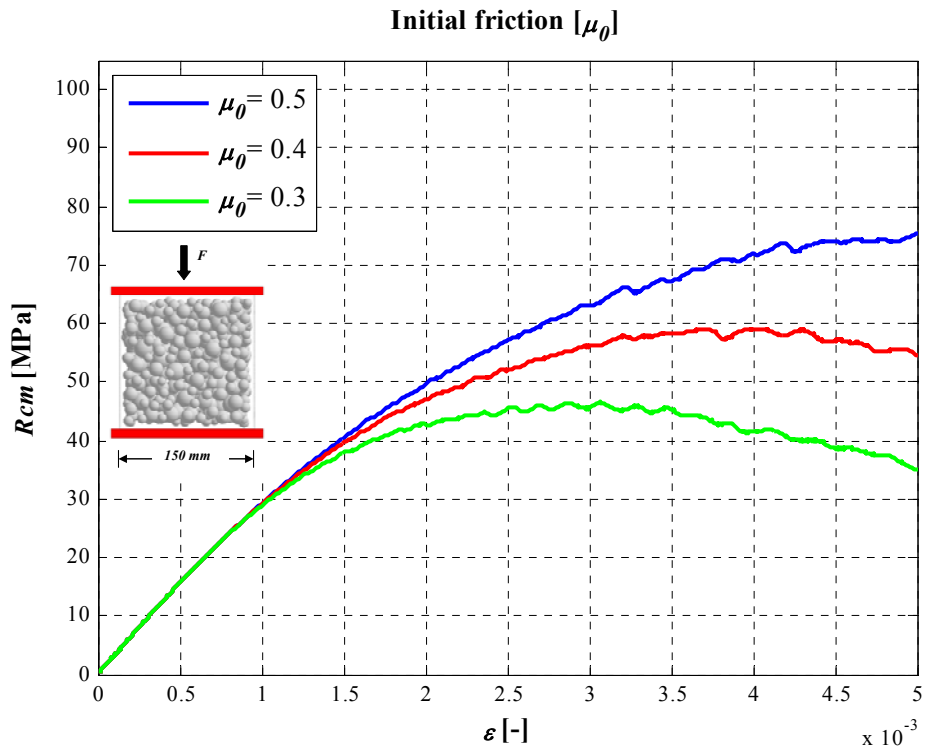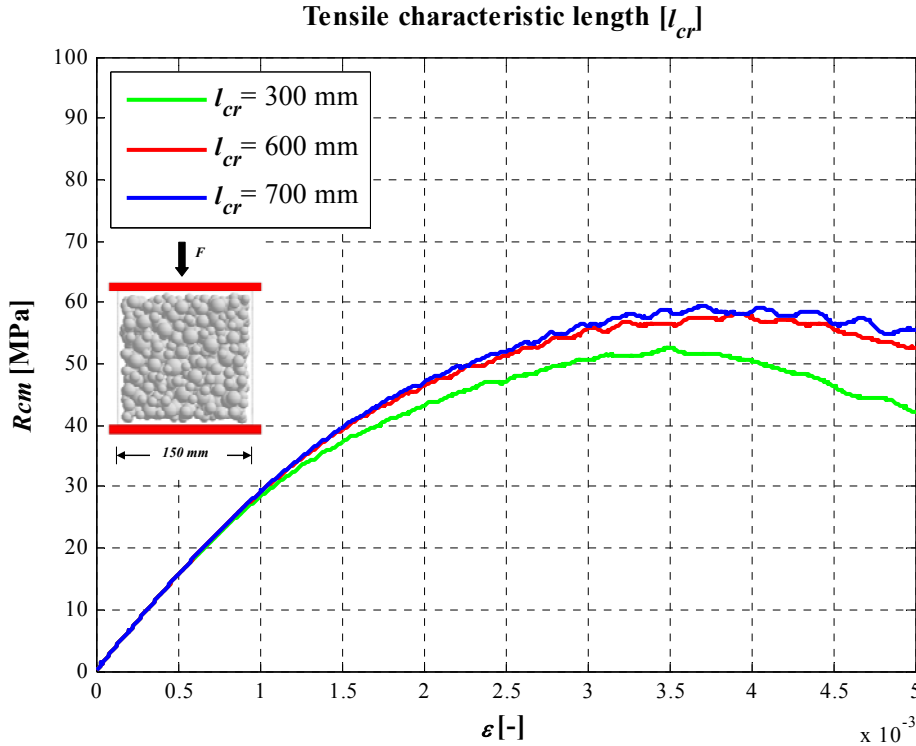**Figure 3.9: Shear strength ratio analysis for UC test.**

Figure 3.10: Initial friction analysis for UC test.

The remain two parameters that are important into the 3PBT calibration test are these types of responses in the UC.

Tensile characteristic length [l_{cr}]

Figure 3.11: Tensile characteristic length for UC test.

Understand how the UC react when these two parameters are changed is very important in the last calibration phases, when both test are almost fit and small changes are needed to complete the model. In this way, the sensibility analysis permit to have just one idea also for this kind of study.
Concluding this will be the order followed for fit the result:

    a) The 3PBT will be calibrated using σ_t and l_{cr};
    b) The UC will be checked with the calibration used for the 3PBT;
    c) If it is not correct this will be changed using σ_s/σ_t and μ_0;
    d) The new parameters values set will be checked for the 3PBT;
    e) If the curves found do not allow to reproduce both the behaviours, the loop restarts from "a" point, until to achieve a good calibration.

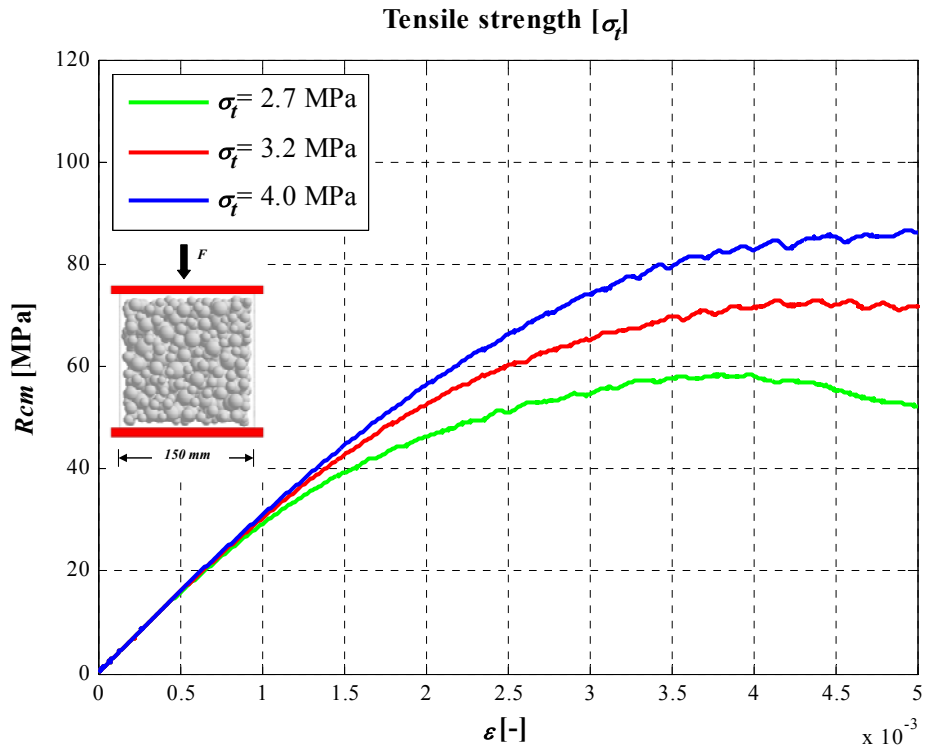Figure 3.12: Tensile strength for UC test.

Calibration stage

For the calibration of the model the 3PBT and UC, previously described, are used. The tests performed are.

- the uniaxial unconfined compression test allows to fit the elastic part E_0 and the peak σ_c for the compressive behaviour;
- the three point bending test is the principal test used for to find the tensile reply of the concrete.

The experimental data available are: two test for the 3PBT and six for the UC for the specimen made only by concrete. The approach used is divided in two different phases.

The first step is the analysis of the experimental curves for both tests. One average curve will be generated to fit at the start the calibration. According with the heterogeneity of the concrete, the experimental tests present a certain scatter and this approach allows to fit the numerical curve on the average. Starting from this, the calibration begins by using a generic seed for the Mars file. It is a tool that is used for positioning the particle into the volume specimen. Changing this value, the randomness algorithm change the position and the heterogeneity of concrete can be reproduced also in the numerical model.

The calibration starts using the common parameters values that are: Normal Modulus 43744 MPa, Densification Ratio 1, Alpha 0.25, Tensile Strength 4.03 MPa , Compressive Strength 150 MPa, Shear Strength Ratio 2.7, Tensile Characteristic Length 120 mm ,Softening Exponent 0.2, Initial Hardening Modulus Ratio 0.4, Transitional Strain Ratio 2, Initial Friction 0.2, Asymptotic Friction 0, Transitional Stress 600 MPa, Volumetric Deviatoric Coupling 0, Deviatoric Strain Threshold Ratio 1, Deviatoric Damage Parameter 5.

The idea is to initially look at how the model response is found and after that start changing the parameters that the previous study has identified has the most important. When a good calibration is found, the second phase start.

In this second step, the idea is to realize one general study being able to show the heterogenic structure of the concrete. With this in mind I lock the parameters values of the previously step, and six tests are run with different seed values. The tables 3.1 and 3.2 summarize the particle and tetrahedrons number present for the different specimens, for both UC and 3PBT. The curves found are averaged and then compared with the experimental average curve. The magenta curve are the curve obtained by the model using different seeds.

If the two curve are fitted the calibration phase is over. Otherwise, it should continue, following the same approach.

The results found for 3PBT are:
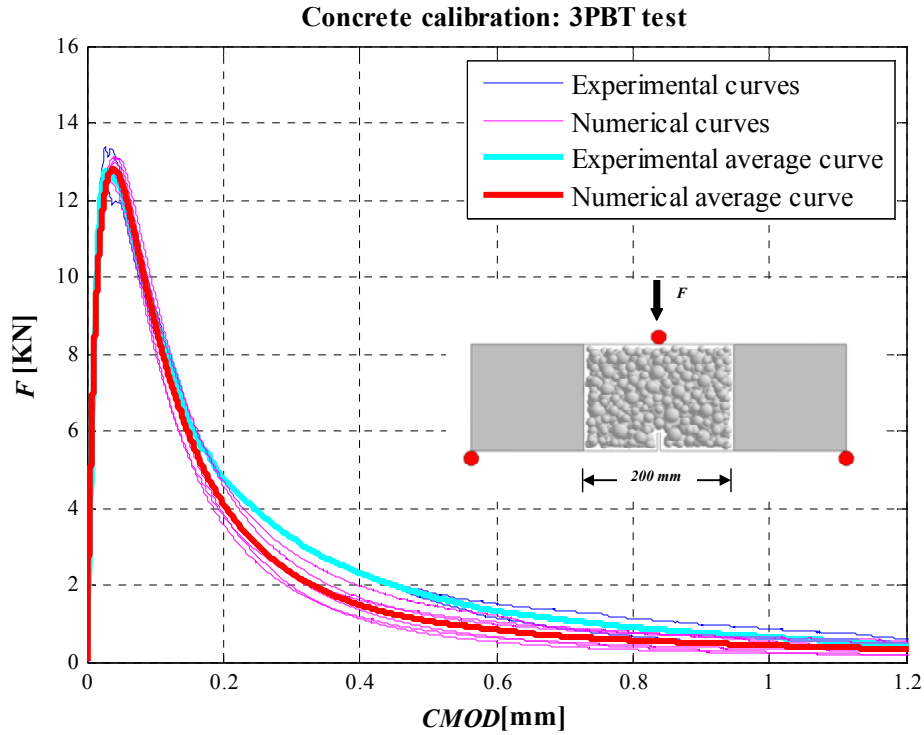
Figure 3.13: Comparison between numerical and experimental results, for 3PBT.

In this figure is possible to see the complete study. The blue curves are the experimental test results and the cyan blue curve is the their average. This is compared with the red curve that is the model average response. As it is shown, the model allows to have a very good fit of the experimental data.

Specimen	Particles	Tetrahedrons
A	1278	5599
B	1276	5610
C	1267	5532
D	1290	5721
E	1258	5530
F	1253	5513

Table 3. 1: UC specimens.

The objective for the UC test is different. In this case only numerical values are available, for fit the pick and the elastic part. These values are picked using

different seeds and then the average curve is used to check the final results. The calibration found for this test is shown here.

Specimen	Particles	Tetrahedrons
A	1656	7385
B	1660	7427
C	1641	7304
D	1651	7340
E	1632	7212
F	1637	7263

Table 3.2: 3PBT single notch specimens.

The images shown how the LDPM allows to fit every part of the curve with an high quality.
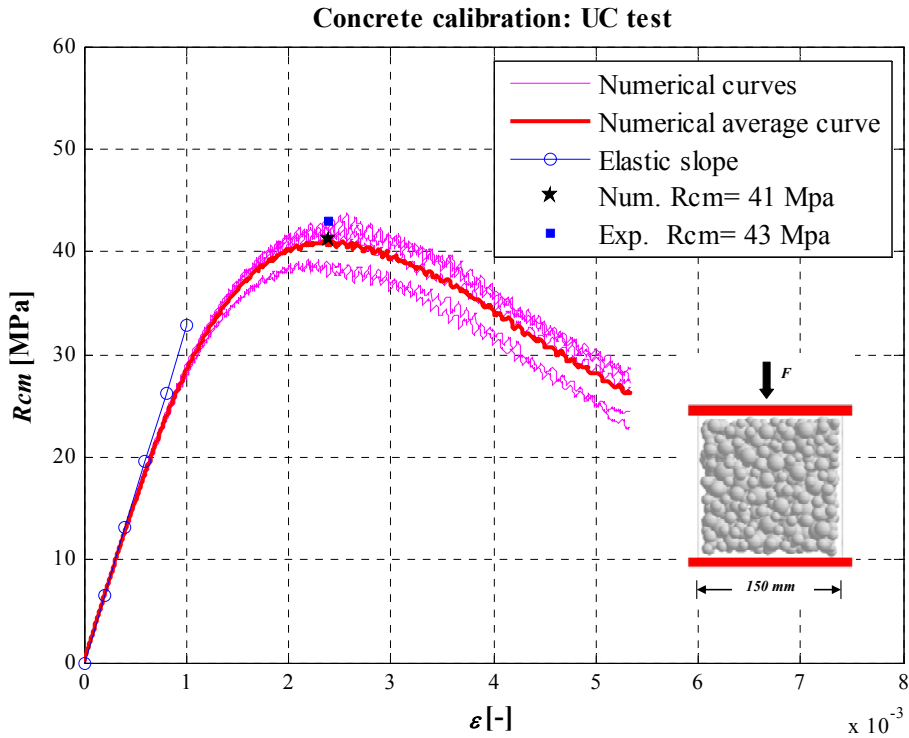

Figure 3.14: Comparison between numerical and experimental results for UC test.

The specimens for UC and 3PBT appear later the test respectively as show in the Fig. 3.15 and 3.16. In this images is possible to see the cracks patterns and also the fragmentation due to the compressive load in the UC specimen.
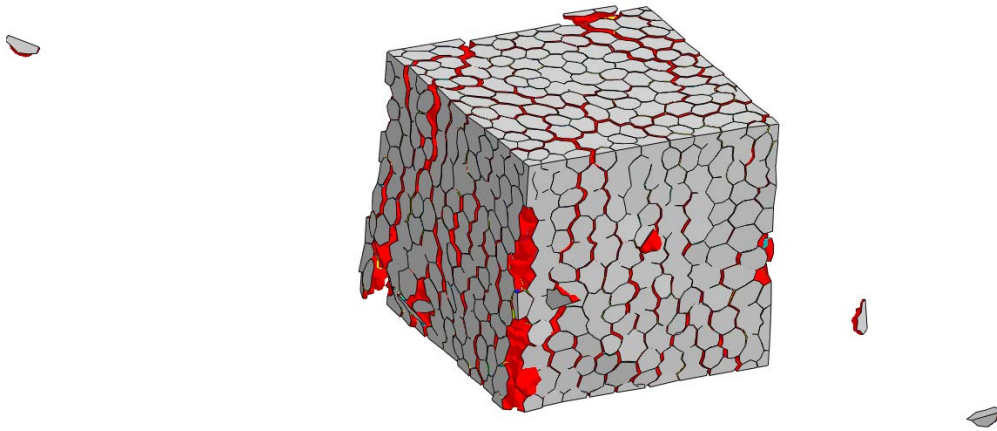
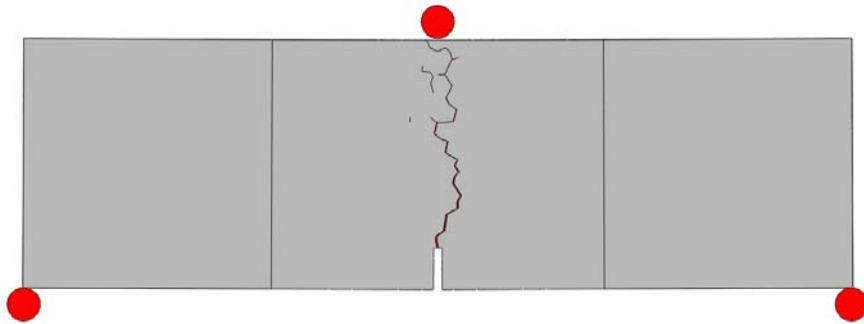**Figure 3.15: UC specimen damage. Cracks evolution.**

Figure 3.16: 3PBT specimen damage. Cracks propagation.

The parameters value that allow this calibration are:

- E_0 = Normal Modulus 50655 MPa
- E_d/E_o = Densification Ratio
- α = Alpha 0.25
- σ_t = Tensile Strength 2.21 MPa
- σ_c = Compressive Strength 195 MPa
- σ_s/σ_t = Shear Strength Ratio 2.5
- l_{cr} = Tensile Characteristic Length 900 mm
- n_t = Softening Exponent 0.2
- H_c = Initial Hardening Modulus Ratio 0.2
- $\varepsilon_{c1}/\varepsilon_{c0}$ = Transitional Strain Ratio 2.7

- μ_0 = Initial Friction 0.25
- μ_∞ = Asymptotic Friction 0
- σ_{N0} = Transitional Stress 600 MPa
- β = Volumetric Deviatoric Coupling 0
- k_1 = Deviatoric Strain Threshold Ratio 0.5
- k_2 = Deviatoric Damage Parameter 5

These value are close to the common range shown by the experience. This allows to say that a good calibration is done. The only strange value is for the tensile characteristic length l_{cr} = 900 mm. Normally, this value range into 120 mm. To check if this is a result acceptable, in the next sub-section one energy analysis is done.

Fracture energy control

The fracture energy control will be done to justify the large value found for the tensile characteristic length, because it is the first time that such large values are found. In line with this, a new test will be done. This test is a dog bone test, that is a test that allows to study the tensile behaviour. No experimental test are available, but the idea is to reproduce one specimen with my calibrate parameters value found and to calculate the Fracture energy . This test is necessary because generally the area under the curve force-displacement divided by the ligament represent the Fracture energy value. In my test, is not possible to done this, because force and CMOD are not two comparable magnitude. to solve this problem, dog bone test is done.

Tensile test are the best for evidence the fracture energy, for this reason this is used. The dog bone specimen is generated with the same material of my calibration and later in the post processing phase the fracture energy is calculate. The Fig. 3.17 shown the specimen.

The value of the fracture energy found calculating the area under the curve, divided by the ligament is:

$$G_d^* = \frac{s}{A_{lig}} = \frac{240 Nmm}{40x60mm^2} = 81\,N/m$$

The objective now, is to compare this value with the value of G_d that can be analytically found using the relation that match fracture energy and characteristic length, written in the first chapter. It is:

$$G_d = \frac{\sigma_t^2 l_{cr}}{2E_0} = \frac{900 x 2.28^2 \dfrac{N^2}{mm^3}}{2 x 50655 \dfrac{N}{mm^2}} = 63\,N/m$$

This control shows that the two Fracture energy found are comparable as value. The reason of this large change with a higher probability is due to the dimension of aggregate. In my test, the particles are arranged in the range of 10-22 mm. These are values bigger than the common values that the experience show. This will be the principle reason.
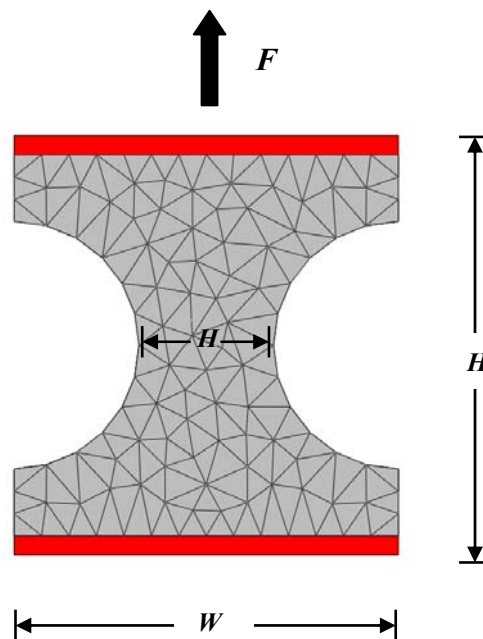

Figure 3.17: Dog bone specimen geometry.

In the next chapter, using this concrete calibration found, the fibbers will be introduced.

Chapter 4

Numerical analysis fiber reinforced concrete (FRC) subject to tension

Introduction

The goal of this chapter is to introduce the fiber into the LDPM and calibrate this new model. The constitutive law that is applied for the relations among concrete-fiber is explained in the second chapter of the thesis. In brevity, the methods used to achieve the objective of this study will be discussed herein.

The developed model is called Lattice Discrete Particle Model for Fiber Reinforced Concrete (LDPM-F). Starting from the results found for the plain concrete, using 3PBT and UC, the fibers are introduced into the specimen, this can be considered the first step. The second step is to calibrate the typical parameters of the constitutive law, followed by validating the results of the analysis.

Figure 4.1: Steel fibers used in the experimental specimens.

The two steps, calibration and validation, are done utilizing experimental data from Buratti, Mazzotti, Savoia and Thooft (2008). The tests done are 3PBT. The specimen is of the same geometry as that shown in the previous chapter, with the same plain concrete plus random distribution of fiber. There are two percentages of fiber distribution for the test. The specimen called SF1B_20 have 0.26 % of

fiber and the group SF1B_35 is characterized by 0.45% of fibers randomly distributed into the specimen. This parameter is identified as V_f. These two groups will be very important for the study, in fact the first is used for the calibration and then the second group allows the validation of the result. In Fig. 4.1 are shown the fibers used in the experimental tests.

Phases of pre-calibration

The pre-calibration phases are the same as those just described in the previous chapter, however the only difference is that there is one more step. According to the order just shown, the new step is introduced after the aggregate generation. This stage is called "fiber generation".

Fiber generation

At the global level, the distribution of fiber-facet intersections is accomplished by generating a uniform distribution of fibers throughout a simulated specimen. From a geometry point of view, physical fiber can be described using a few parameters: fiber density, length, diameter, and tortuosity. The latter parameter is used to characterize the fiber shape: a straight fiber has no tortuosity while a fiber with many "kinks" is very tortuous. These geometric parameters are used in MARS for generating random fibers inside a control volume, which can either be the volume of the entire specimen or a larger volume that contains the specimen. Each fiber is modelled using a sequence of one or more segments linked together. Single segments are sufficient for generating straight fibers. Multiple segments are necessary for generating "tortuous" fibers. Fiber location and orientation are assumed to be randomly distributed. All fibers are completely contained in the control volume. For cast FRC parts, the control volume should be equal to the volume of the simulated specimen. For machined parts, the control volume should be larger than the simulated specimen. The fibers that intersect the external surface of the part are treated as cut. The portion of a cut fiber which lays inside the part is shorter than the length of original fiber and this affects the mechanical characteristics of the fiber-facet interaction near the external surfaces. In the spirit of the discrete, multi-scale physical character of LDPM, the occurrences of fiber-facet intersection are determined by computing the actual locations where fibers cross inter-cell facets. This computation can require significant resources for large models in terms of both time and memory. For this reason, an efficient bin-sorting algorithm was developed for computing these intersections. For each intersection, the fiber length on each side of the facet and the orientation at which the fiber intersects the facet (crack plane) are computed. These parameters are saved in the facet data structure and used during the simulation for calculating the fiber

contribution to the LDPM facet behaviour. It is worth noting that the uniform distribution of fibers throughout a volume is sometimes not realistic due to the intrinsic technical difficulties of dispersing the fibers evenly in an actual concrete specimen. This issue needs to be taken into account carefully when calibrating and validating the model, G.Cusatis, and co-worker (2009). In these tests used steel fibers for calibrating the model. The values of the principle characteristics implemented in the code to represent and describe the fibers characteristics are:

- Fiber Length=5 cm
- Element Size=5.01 cm
- Fiber Section Area=0.785 mm^2
- Tortuosity=0.0
- Volume Fraction=0.0026
- Elastic Modulus=210 GPa
- Fiber Strength=1100 MPa

According to these properties the specimens can be generated. The geometry is the same as that used for the plain concrete test, in other words a prismatic notched specimen with span of 500 mm. Fig. 4.2 shows the specimen, where it is possible to see the fibers presence. They are represented in blue colour and the particles are plotted in transparent way to show a better view of the fibers.
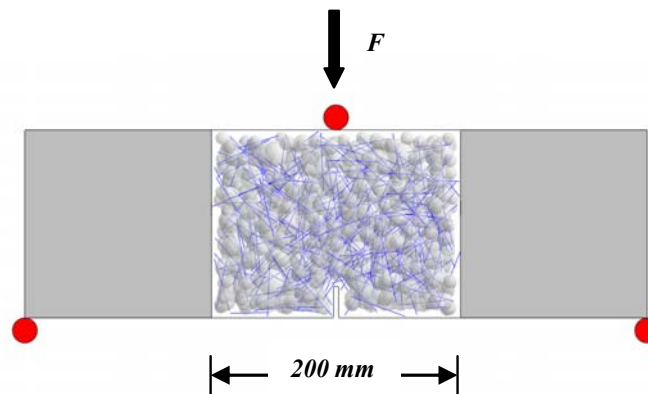
Figure 4.2: 3PBT specimen with fibers.

In this Fig. 4.2 it is possible to see that the only central part, where damage is expected to occur due to the presence of notch, is modelled thought LDPM-F, while the two lateral parts are modelled with standard elastic finite elements. All of the specimens have an out of plane thickness of 150 mm.
The second step is to define the parameters that will be calibrated to make the model usable. The tests done for calibrating the model were 3PBT.

Presentation of parameters

The Lattice Discrete Particle Model for Fiber Reinforced Concrete (LDPM-F) is governed by 11 parameters that allow the description of the concrete-fibers behaviour. These parameters that are now shown will be added to the other 16 meso-structure parameters that are calibrated for plain concrete. The strain and strength that are measured on the generic triangular face of model are the combination of concrete and fiber contribution. The parameters are:

E_f = Elastic Modulus

k_{sp} = Spalling Parameter

σ_f = Fiber Strength

k_{rup} = Fiber Strength Decay

k_{sn} = Snubbing Parameter

τ_0 = Bond Strength

η = Volume Stiffness Ratio

G_d = Debonding Fracture Energy

β = Pullout Hardening

k_p = Plastic Parameter

k_{cg} = Cook Gordon Parameter

Model sensibility

The LDPM-F allows reproducing the concrete-fiber behaviour. The fibers are designed to work when the cracks initiate, for this reason their effects on tests characterized by tension are more important compared to tests characterized by compression and shear. Accordingly, only this kind of tests are reproduced. The calibration phase for concrete-fiber specimens starts by conducting a sensibility analysis of the model.
This is the first work done with this model, since there are no available results or examples from the literature. In the sensibility analysis a specific study over the parameters was done. For each parameter three numerical tests were done by changing the number of the parameters analyzed. Clearly the other parameters excluding Debonding Fracture Energy G_d, Bond Strength τ_0, Elastic Modulus E_f and Fiber Strength σ_f, are put equal to zero. The results found are presented in the next series of figures.

These figures 4.3 and 4.4 show how the curve for 3PBT change in according to the different values of the parameters. In the second chapter only one sensibility analysis was made for the only one fiber pullout case, but it can not take completely the "big" test in account, in which the number of fibers is bigger than single pullout and also the force which is applied in different ways.

The results found shows that in some cases, for example for the Pullout Hardening β the model response is almost the same as that which was found in the single fiber analysis. Worth noting is that it is possible to divide these parameters in two groups, according to the relative importance that they have in the calibration process. The first group is formed by Debonding Fracture Energy G_d, Pullout Hardening β, Bond Strength τ_0, Fiber strength σ_f and Elastic Modulus E_f. The sensibility of these parameters is obvious from the following figures.
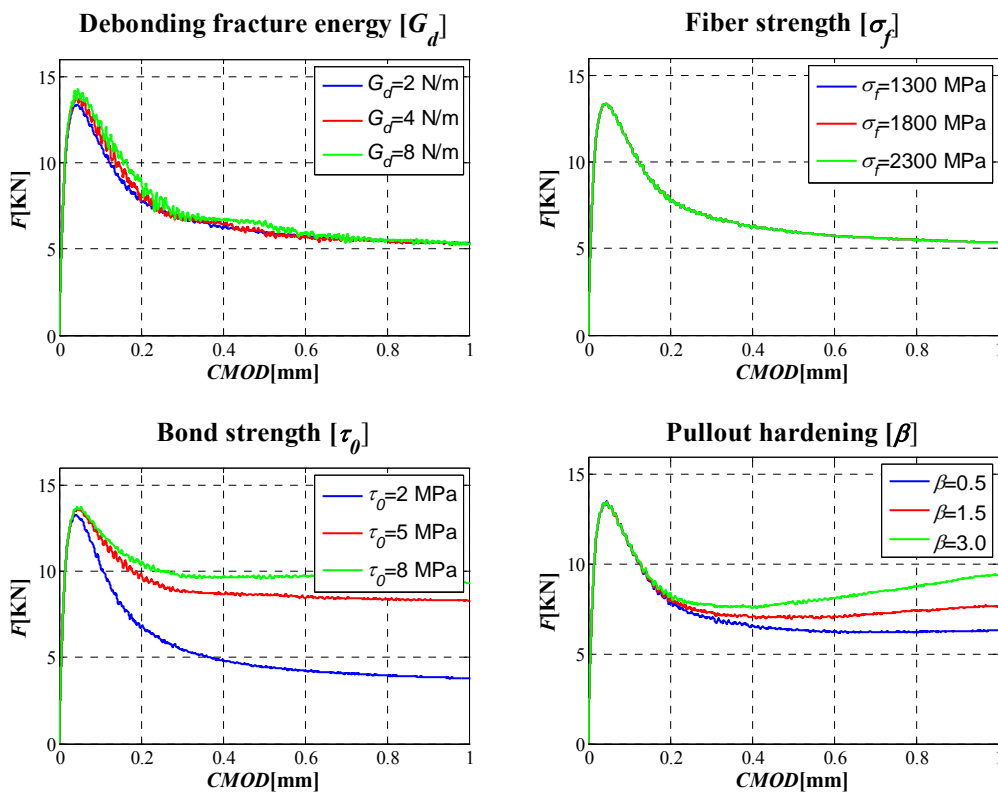

Figure 4.3: Parametric analysis of the principle parameters

The second step is done by the remaining parameters. The aim is to work over parameters that allow the calibration the model for the 3PBT, and also for other kinds of tests to achieve a calibration that permit to reproduce the behaviour for every kind of steel fibers.

Following this target, the work will be developed using values of parameters, that allow to fit also tensile tests. Parameters like Volume Stiffness Ratio η and Cook Gordon Parameter k_{cg} are assumed to be equal to zero, because their effect can be considered negligible.

Following are shown the remaining parameters which govern the fiber-concrete behaviour, Fig. 4.4.

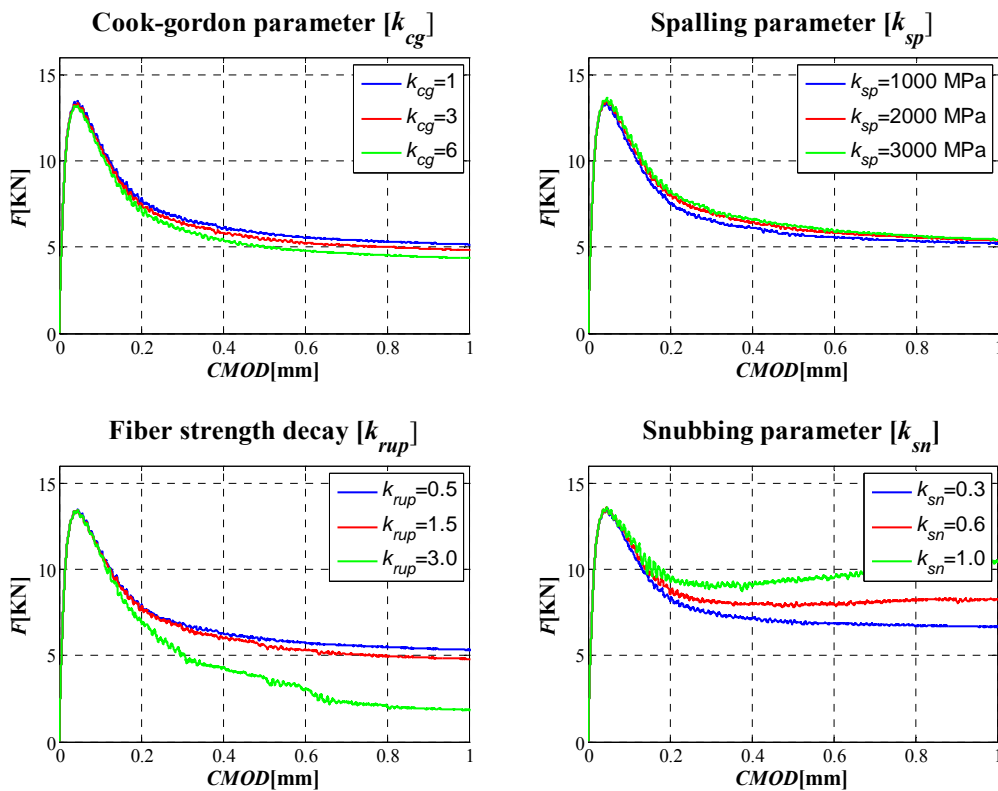Taking in consideration all the results from this sensibility analysis, the calibration was done.

**Figure 4.4: Parametric analysis of the
remaining parameters**

Calibration stage

The experimental data presents two different group of specimens characterized by different percentages of fibers dispersed into the specimens, this parameter is called V_f. The SF1B_20 is used for the calibration.

This group presents V_f = 0.26 % of fiber and seven experimental tests are done.

The table 4.1 shows the number of particles and tetrahedron present in the different specimens.

Specimen	Particles	Tetrahedrons
A	1656	7385
B	1676	7465
C	1634	7238
D	1660	7376
E	1617	7151
F	1687	7609
G	1658	7362

**Table 4.1: 3PBT single notch specimens
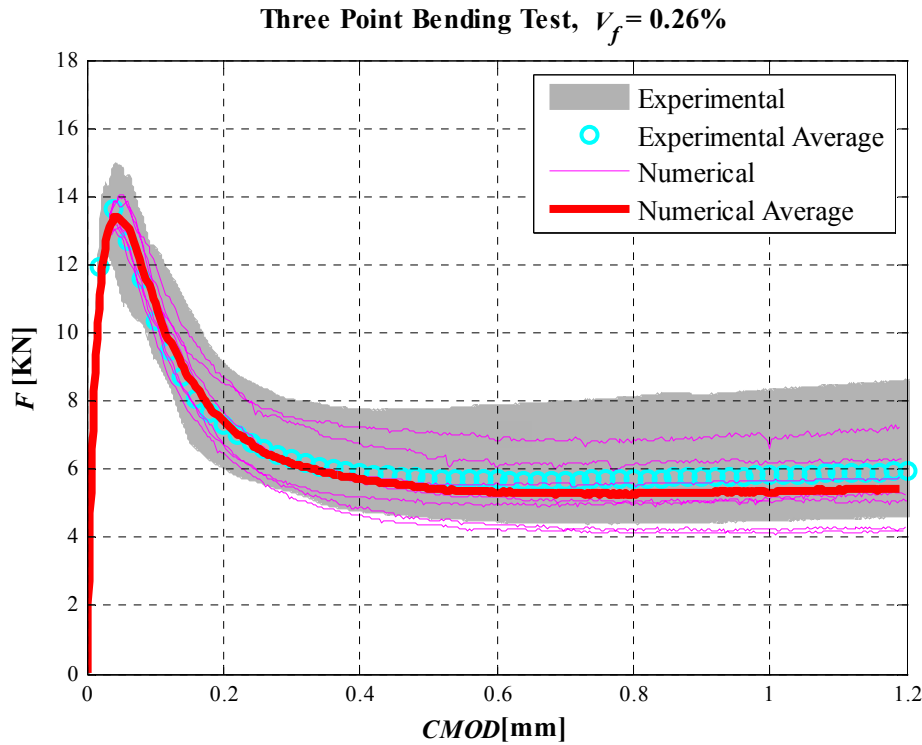with V_f= 0.26% of fibers.**

According to the approach used in the concrete calibration stage, one average curve will be generated to fit the start the calibration. The experimental tests show a certain scatter among the seven curves, which is very big. Two causes can be attributed to this scatter: the heterogeneity of the concrete and the different position that the fibers have in the specimen. For example one specimen that present more fiber in the central section allows to have more stress than another specimen where the fiber are close to the support. The fiber distribution is another important random effect that needs to be considered for this material.

The model was built taking into account these two effects. For simulating real situations, the MARS is equipped with two different seeds. One that is positioned in the Gen.mrs allows the reproduction of the heterogenic structure of the concrete, and the other located in the Run.mrs allows to change the random distribution of the fibers. By changing the seeds the randomness algorithm change the position of the particles and the fibers. The two files, nominated before, are the typical input files used in the numerical analysis.

Starting from the average experimental curve the calibration begins by using a generic seed for the Gen.mrs and Run.mrs files.

The idea is to initially look at how the model responds and after that start changing the parameters, defined in the previous section, to identify the most important ones. When a good calibration is found the second phase starts.

In the second step, the idea is to define a general study and to be able to show the heterogenic structure of the concrete and also the random distributions of fibers. Accordingly, utilizing the parameters values from the previous step, seven tests were run with different seed values. Clearly both the seeds in Run.mrs and in Gen.mrs were changed.

The curves found are averaged and then compared with the experimental average curve.

Figure 4.5: Comparison between numerical and experimental results, for 3PBT with V_f= 0.26% of fibers.

The agreement between the numerical results and the experimental data is very good. The values found for the parameters are:

- Elastic Modulus [E_f]=210 GPa;
- Spalling Parameter[k_{sp}]=150 MPa;
- Fiber Strength[σ_f]=1100 MPa;
- Fiber Strength Decay[k_{rup}]=0.0;
- Snubbing Parameter[k_{sn}]=0.5;
- Bond Strength[τ_0]=6.0 MPa;
- Volume Stiffness Ratio[η]=0.0;

- Debonding Fracture Energy[G_d]=5.0;
- Pull Out Hardening[β]=0.0;
- Plastic Parameter[k_p]=1.0;
- Cook Gordon Parameter[k_{cg}]=2.0;
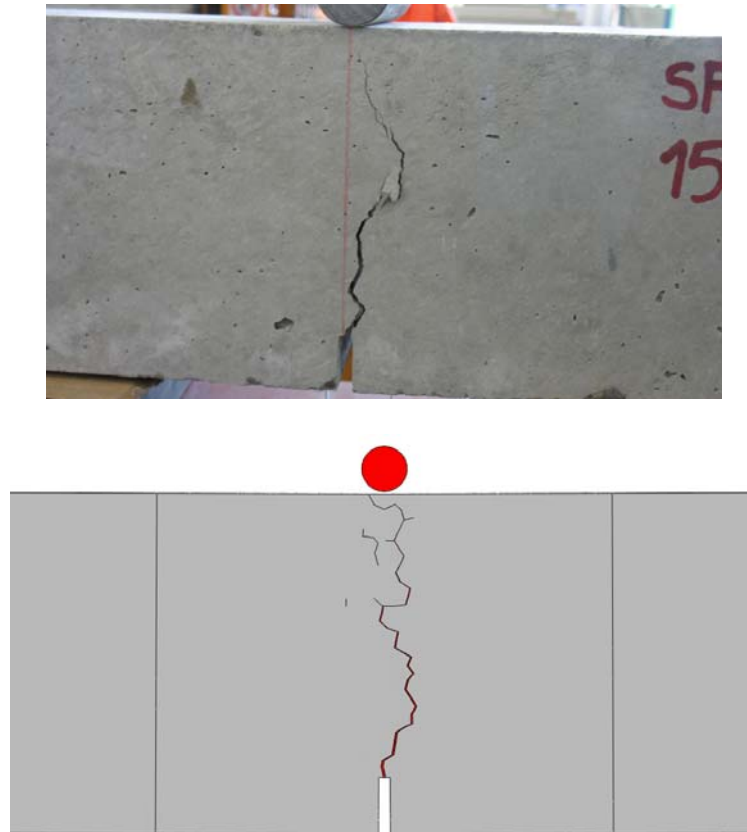
Figure 4.6: Comparison between of the damage of experimental and numerical beams subject to 3PBT.

Validation stage

In this stage the validation is done. The experimental group characterized by 0.45 % V_f is used to check if the model works. The idea is to have new numerical test using the same parameters set and changing only the fiber percentage distribution to fit the experimental curve. Accordingly, seven specimen were run.

Specimen	Particles	Tetrahedrons
A	1611	7057
B	1646	7270
C	1617	7149
D	1656	7385
E	1635	7247
F	1619	7115
G	1650	7311

Table 4.2: 3PBT single notch specimens with V_f = 0.45% of fibers.
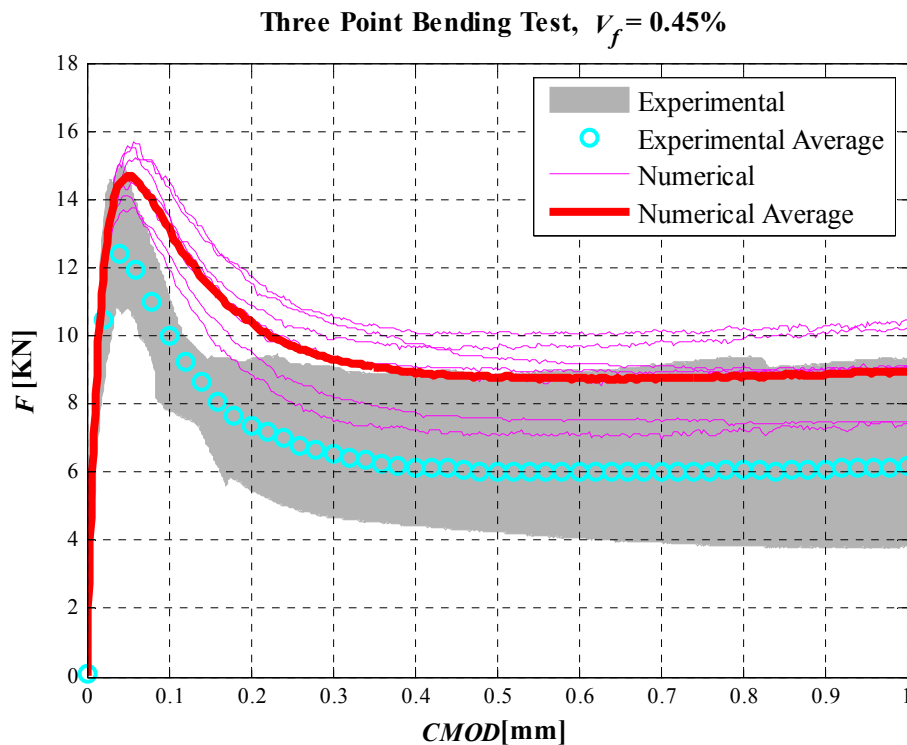

Figure 4.7: Comparison between numerical and experimental results, for 3PBT with V_f = 0.45% of fibers.

The results obtained in this case produce a post-peak load carrying capacity higher than the experimental one. For a CMOD of 0.8 mm the difference between the average numerical and experimental curves is about 45%.

In order to clarify this apparent discrepancy, it is useful to compare the actual number of fibers bridging the crack in the experimental and in the numerical simulations. During the experimental campaign, post-mortem evaluation was performed and the number of fibers on the crack surface was counted for all specimens of both FRC mixes. For the experimental test, the number of fibers in each third of the ligament length (i.e. the reduced cross-section with associated notch, as shown in Fig. 4.8).

The different areas identified in this way are named bottom, middle and top, respectively. Defining them is very important to understand the fibers response. The same information was clearly extracted from the numerical simulations.
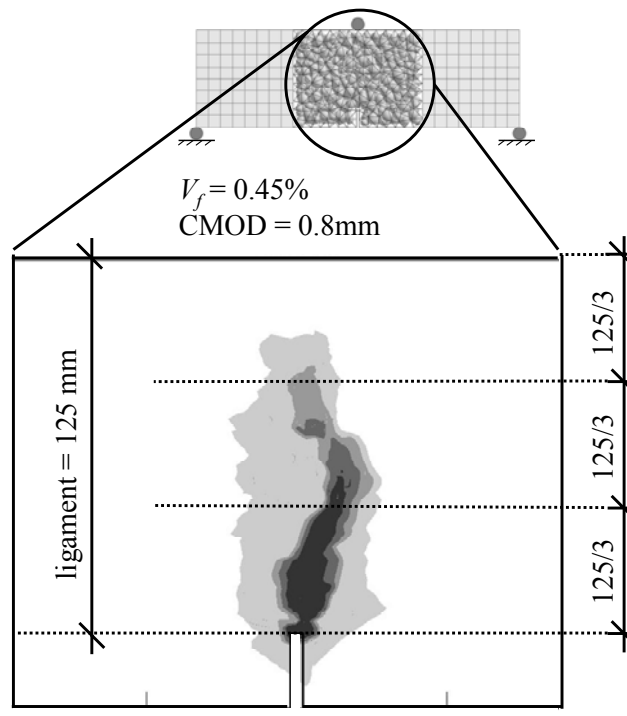
Figure 4.8: Crack opening isosurfaces.

To study the CMOD-Force in the fibers case, another approach will be used. The idea is to analyze the increment of load due to the fibers effect and finds a relation among this increment and the position of fibers in terms of bottom, middle or top area.

The new parameter introduced is the load increment, it is expressed by this relation: $L_i = 100(1 - P/P_0)$, where P is the load for the FRC specimens and P_0 is the average load for the plain concrete specimens.

Accordingly, plots of the load increment versus the number of fibers considering the bottom, bottom-middle and total regions were done. The results shows that this relation is very good for only the bottom region and also if the bottom-middle area is considered. Following this results the only two-thirds of the ligament length is plotted.

This choice is motivated by analyzing the crack pattern in the numerical simulations. Fig. 4.8 shows a gray-scale isosurfaces from a typical mesoscale crack opening. Each surface corresponds to a different crack opening value.

The minimum value that was plotted (very light gray) corresponds to a crack opening magnitude of $2v_d$. This corresponds to a situation at which a straight fiber, orthogonal to the crack surface, would experience full debonding (onset of the frictional pull-out phase). At this level of crack opening, fibers can be considered fully active. As it can be seen from the Fig. 4.8, the zone characterized by fully active fibers extends to approximately two-thirds of the ligament length above the notch. This indicates that the results are not perfect if the total section is considered. To highlight this finding, the relation among Number of Fibers and Load Increment due to fibers is plotted in Fig. 4.9. In this figure the Load Increment Due to Fiber is plotted for CMOD = 0.8mm.
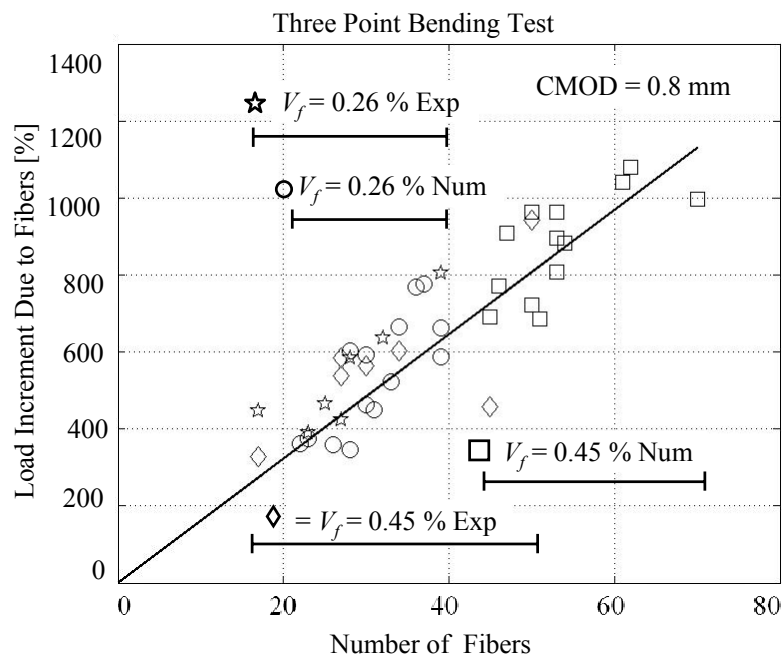

Figure 4.9: Load increment due to fiber versus number of active fibers.

This Fig shows clearly that there is a linear relationship between the load and number of fiber detected, and that both the experimental data and the numerical results have a similar trend. Looking with depth to the figure, it is possible to note that one inconsistency is present. This is matched with the number of the detected fibers from the experimental specimens.

For the numerical specimens, the range of detected fibers increases from (22-39) to (47-70) as the reported fiber volume fraction is nearly doubles from V_f=0.26% to V_f=0.45%. In the experimental tests, the increase in the number of detected fibers from (17-39) to (17-50) is not consistent with the near doubling of V_f. For the higher V_f the numerically simulated specimens feature more active fibers than the experimental ones. This explains the discrepancy in the curves shown in the Fig. 4.7, while confirming the validity of the fiber-matrix interaction strategy adopted in this study.

The different between the number of active fibers within the experimental and numerical crack ligament is due to the fact that in the numerical model a uniform fiber distribution was obtained, while such uniformity apparently was not obtained in the experimental specimens with higher V_f. Based on the fact that fiber dispersion can be significant in terms of load carrying capacity, LDPM-F should be extended to include non-uniform fiber distribution and, in addition, experimental data should be provided and more information about the actual fiber distribution obtained during specimen casting should be provided, G.Cusatis and co-worker(2009).

Chapter 5

Numerical analysis of projectile penetration for FRC slabs

Introduction

The goal of this chapter is to investigate the dynamic loads exerted on plain concrete slabs and FRC slabs by impacting objects. Examples of these problems include icebergs impacting floating concrete drilling platforms in the North Atlantic, aircraft crashing into concrete structure, missile impact. For concrete under quasi-static loading conditions, the failure mechanisms and constitutive relations for concrete under impact and high strain rate loading are not well known yet; partly because of the experimental and analytical difficulties involved, also relatively few studies of these relationships have been carried out under impact loading (Midness 1993). Considering the experimental tests described in Hanchak (1992), where impact tests where simulated using steel bullet, the numerical analysis in this study was developed.

The objective of this study is to investigate the response of FRC slabs under impact loading, and the effect of the slab thickness, the striking velocity of the bullet, and the percentage fibers in the concrete mix on the slab response. The results will be presented in terms of the bullet striking velocity and residual velocity just after exiting the slab.

The approach used herein to simulate these tests is to start by investigating the response of plain concrete slabs and to check if the model yields the same behaviour for experimental tests. The slabs were subjected to different shots to understand the controlling factors of the response. FRC slabs were then used and a parametric study was done to investigate the different parameters affecting the slab response.

Thus, the ballistic limit is the fundamental parameter that will be monitored to understand how the slab response change accordingly, for each test.

Geometry of the test

In order to simulate the impact test on the slab, two elements will be generated utilizing MARS; the slab and bullet elements. In this paragraph the geometry and the techniques used in generating both elements will be discussed.

The slab elements are 508 mm squares with two different thicknesses, t=50.8 mm and 101.6 mm. The slab is modelled using LDPM-F assigned the material parameters previously described. Fig. 5.1 shows the layout of the slab element.
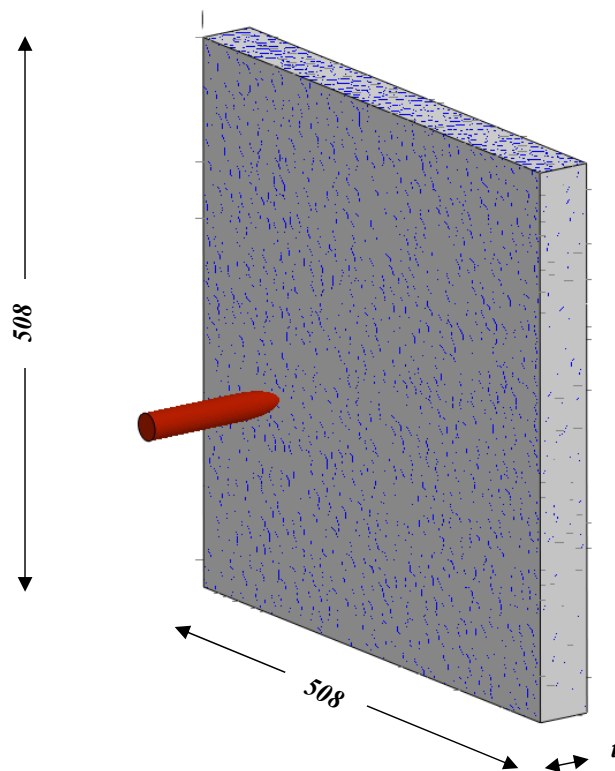
**Figure 5.1: Slab geometry realized by
LDPM and LDPM-F**

The bullet is simulated in accordance with the geometry and material properties described in the Hanchak (1992); The bullets were implemented in the numerical model as a rigid body where its steel properties were assigned according to "Vascomax t-250 Maranging Steel".

The geometry of the problem was chosen such that the bullet was placed at 25.4 mm from the slab, where the shot is positioned. Basically, this parameter doesn't affect the numerical test results, but it was found a reasonable value with respect to the computation time. The Fig. 5.2 shows the bullet geometry.

**Figure 5.2: Bullet geometry, realized
with finite element.**

Starting with this configuration the simulations were performed.

Penetration test of concrete slab

Plain concrete slabs with two different thicknesses were subjected to penetration tests under the bullet impact loading. The slab was subjected to impact velocity of up to 450 m/sec . This range of impact velocity was chosen in order to check how the ballistic limit, expressed as the highest strike velocity associated with zero residual velocity, increases with increasing t .

The first step was to check that the $V_s - V_r$ curve presents the same trend obtained from experimental results. To asses this comparison, different shots were done using different strike velocity V_s . For each velocity six numerical analyses were run by changing the "seed" parameters according to the reproduced heterogenic structure of the concrete. This approach allows to reduce the local effects caused by the internal structure of the concrete. The points used to create the $V_s - V_r$ curve were obtained by averaging the values from the six point, previously discussed.

The table 5.1 gives the bullets velocities used in the different shots. These lists of velocities fundamentally are chosen considering that the curve trend close to the ballistic limit is nonlinear. For this reason, large number of shots are selected in this zone. This region is identified as: velocity of ballistic limit-V_s = 150 m/sec.

However, it is important to highlight that this range is valid only for plain concrete slabs. The following table shows how the residual velocity change with respect to the slab thickness, where the ballistic limit is linked to.

Based on these data, the ballistic limit was found to increase with increasing t .

For plain concrete slabs with t = 101.6 mm the ballistic limit was found to be approximately 95% higher than that for slabs with t = 50.8 mm.

t =50.8 mm		t =101.6 mm	
V_s [m/sec]	V_r [m/sec]	V_s [m/sec]	V_r [m/sec]
30	0.00	100	-57.528
33	0.9651	110	-5.036
35	12.499	120	-3.871
40	24.932	126	0.00
48	46.726	130	0.9933
50	51.375	140	76.747
60	93.556	150	16.663
75	17.585	160	24.718
85	25.387	170	33.916
100	38.679	180	44.314
150	93.175	200	63.912
250	192.48	250	112.84
450	390.31	450	317.04

**Table 5.1: Results in term of V_s and V_r for
t=50.8 mm and t=101.6.**

The results can be represented in a plot format as follows:

**Projectile Penetration Analysis: Plain concrete**
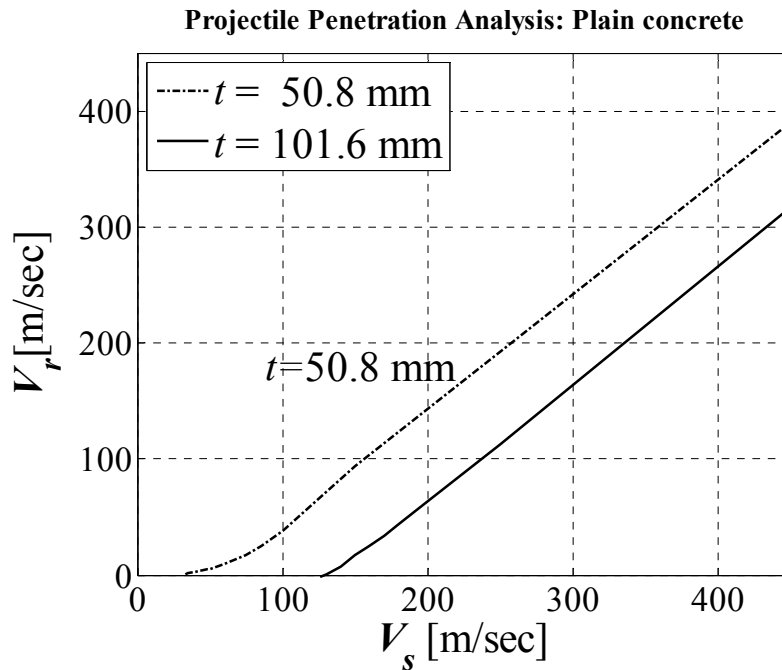
**Figure 5.3: Striker velocity versus Residual velocity for
plain concrete test for two thickness.**

As can be seen, the trend of the curves is nonlinear in the zone close to the ballistic limit, and is linear for shots characterized by striking velocity higher than 150m/sec. Based on this response, the tests were done using more shots in the limit zone to capture the best possible value for the ballistic limit. This Fig. 5.3 also demonstrates the capability of the numerical model in capturing the concrete behaviour, compared to the results found in Hanchak (1992).

Naming V_s^* the striker velocity that produces zero V_r, which is the condition identifying the ballistic limit. It is worth noting that the residual velocity can become negative value if $V_s < V_s^*$. Although it seems unreasonable, this case represents a real situation. Basically, this curve is the ballistic limit, which is the point characterized by the coordinate $V_s^*; V_r = 0$ m/sec, that represents a boundary dividing three different behaviours.
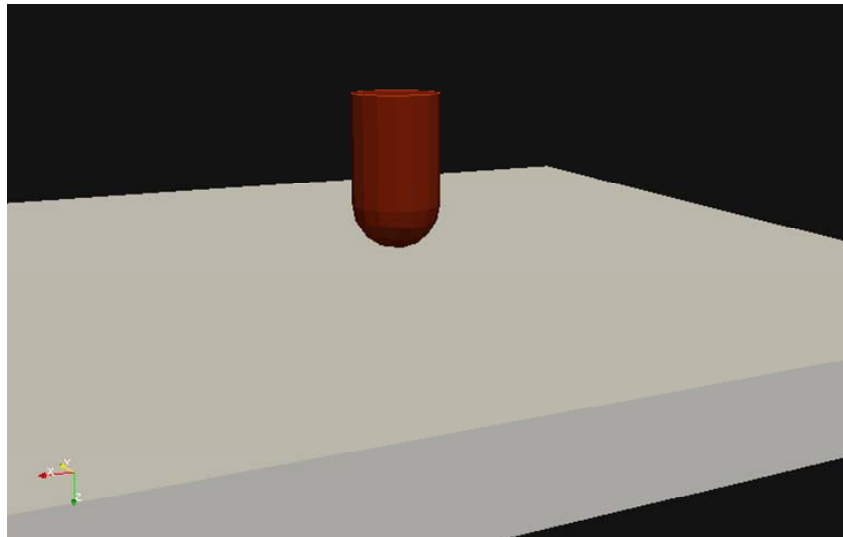
Figure 5.4: Numerical simulation of penetration into Plain Concrete Slab.

First behaviour is when $V_s > V_s^*$; the bullet will penetrate the slab and the residual velocity is proportional to the impact velocity. The second behaviour can be taken as the ballistic limit which is the point that divides two completely different responses. Here the projectile impacts the slab and it stays inside the slab, in this case the residual velocity is equal to zero.

The last situation possible is not shown in the Fig 5.3 . The curve in this case is placed in the second face. The behaviour gives residual velocity that has a negative value. In this case the physical phenomenon can be seen that the bullet can not penetrate the slab and it rebounded after collision. The slab was obviously damage, but its integrity is guaranteed. In this case there are also fragments in the other side of the slab due to the bullet impact but the number of these fragments is less than before.

According to this study it is possible to say that increasing the slab thickness allows to increment the ballistic limit. The effect of the thickness is kept the same also for high striking velocities.

Later will be shown that this relation was not found for the FRC slabs.

Penetration test of FRC slab

In this section, the simulations of steel projectile impacts on FRC slabs are studied, for different impact velocities. The numerical simulations were performed using the same material parameters defined in the previous chapter. The slabs used for this material have the same dimensions and also two different thicknesses were used. Using the same approach as in plain concrete slabs, both the thickness values and the fiber volume fractions where changed in the different simulations. To investigate the effect of fibers on the impact problems, three different volume fraction were examined: V_f = 1%, 2%, and 3%.

Projectile Penetration Analysis: FRC
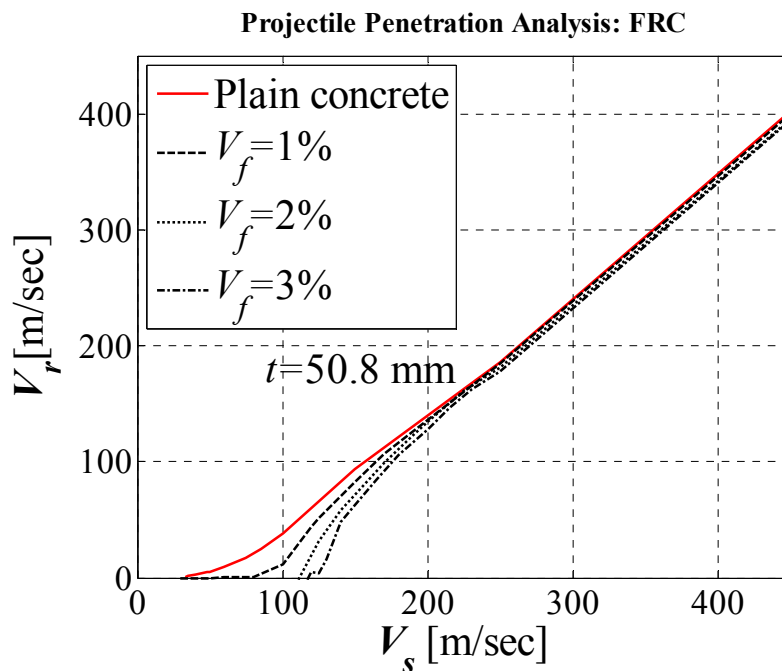
Figure 5.5: Striker velocity versus Residual velocity for FRC slabs test for t = 50.8 mm.

The Fig. 5.5 shows for FRC slab with t = 50.8 mm the obtained trends. Here is also plotted the curve for plain concrete in order to point out the fibers effect on the penetration problem.

Plain concrete		V_f= 1% mm	
V_s[m/sec]	V_r[m/sec]	V_s[m/sec]	V_r[m/sec]
30	0.00	35	-0.8465
33	0.9651	53	0.00
35	12.499	60	0.3382
40	24.932	80	0.8214
48	46.726	100	11.575
50	51.375	120	43.563
60	93.556	125	51.261
75	17.585	140	70.047
85	25.387	150	83.068
100	38.679	160	95.241
150	93.175	170	107.17
250	192.48	250	184.85
450	390.31	450	400.24

Table 5.2: Results in term of V_s and V_r for
t=50.8 mm and different V_f.

V_f= 2% mm		V_f= 3% mm	
V_s[m/sec]	V_r[m/sec]	V_s[m/sec]	V_r[m/sec]
70	-1.5256	118	0.00
90	-2.6334	120	4.4465
110	-2.8813	125	3.454
125	31.467	130	15.676
140	57.949	140	47.703
150	71.491	150	62.875
170	98.807	165	85.166
190	122.51	180	105.46
200	134.34	200	128.36
225	160.94	215	146.46
230	163.67	230	162.62
250	180.85	250	177.85
450	396.24	450	395.24

Table 5.3: Results in term of V_s and V_r for
t=50.8 mm and different V_f.

It is worth noting that the ballistic limit increase with increasing V_f. The FRC slabs with 1% V_f have ballistic limits that are approximately 50% higher than that for plain concrete. The slabs with 2% V_f showed an increase of 90 % higher than that for plain concrete slabs. Increasing the fibers percentage further does not

increase the ballistic limit. Everything can be summarized in the table 5.2. and 5.3.

The second step will be to perform the same study for $t = 101.6$ mm.
The following Fig. 5.6 gives the results from all tests:
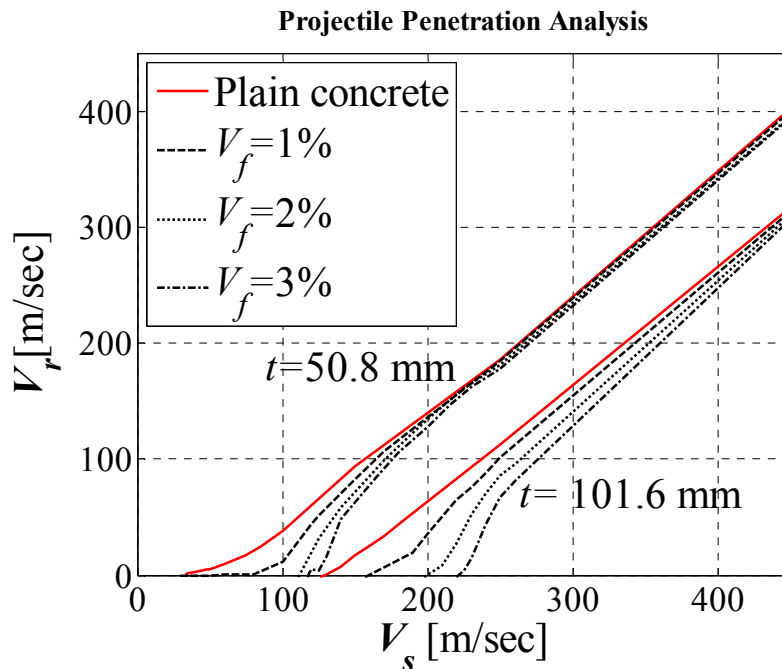
Figure 5.6: Striker velocity versus Residual velocity for FRC slabs test for $t = 101.6$ mm.

As it can be seen, the ballistic limit increases with increasing V_f. The FRC slabs with 2% V_f have ballistic limit that are roughly 175% and 80% higher than that for plain concrete, for $t = 50.8$ mm and 101.6 mm, respectively. The results are summarized in the following table

The 3% V_f simulations show, however, that an additional increasing in fiber content does not necessarily correspond to a significant additional increasing of the ballistic limit. Finally, the effect of the fibers becomes less and less significant for high striking velocities. This is due to the fact that at very high striking velocities, the penetration phenomenon is governed more by the mass of the system and the confined compressive resistance, rather than by the tensile fracturing behaviour, which is significantly influenced by the presence of the fibers.
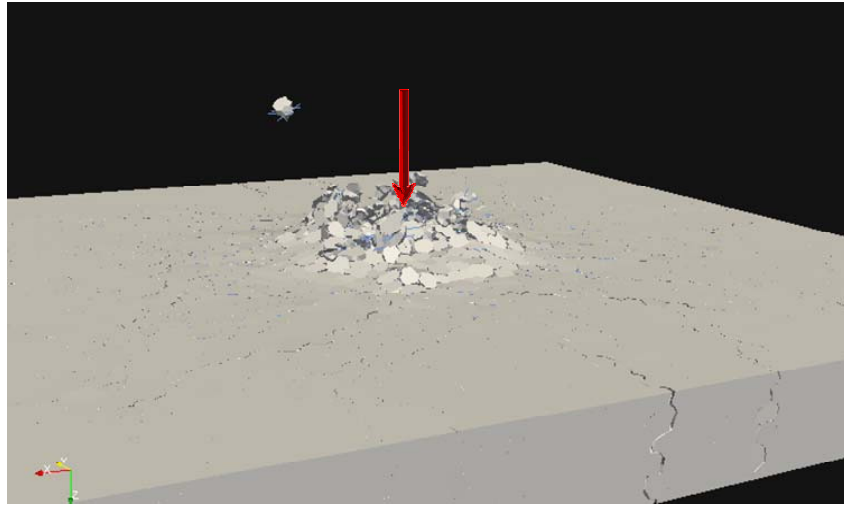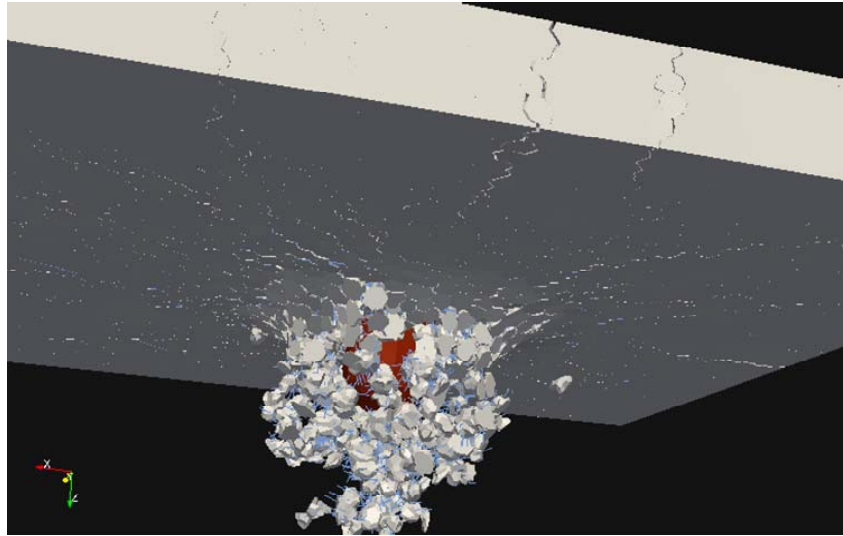
Figure 5.7: Snapshots of the penetration event characterized
by the formation of entrance craters.

Design of Armoring System

The study that is proposed in the previous section allows to explore different application for concrete and FRC structure. The idea of this paragraph is to present some of these applications. One example is found in Cusatis and al (2009). Here is shown the research developed by Engineer Research Development Center (ERCD). They are performing research towards the innovative design of lightweight and low-cost armoring systems. Within this effort, experimental characterization of very high strength ($f_c^{'}$ = 157 MPa) FRC mix was performed both quasi-statically and dynamically, Akers et al (1998).

In this work, the dynamic experiments consisted of impacts from a Fragment Simulating Penetrator (FSP) into FRC panels. The principle parameters that are considered for these tests are: FSP velocity and target panel thickness. These are chosen to generate extreme deformation of surface craters and perforation through the target. Of concern are the damage generated by the FSP to the target plates and the residual velocity when the projectile exits the target.

**Figure 5.8: Snapshots of the penetration event characterized
by the formation of exit craters.**

The fibers used were steel fibers of 25.4 mm length and bent ends, and were randomly distributed during the casting phase. Penetration experiments were conducted to measure the FRC's resistance to ballistic projectile penetration. Panels tested were 304.8 mm squares of 25.4, 50.8, and 76.2 mm thickness.

The LDPM-F is used to reproduce these experimental tests. Some preliminary results are reported herein. The LDPM-F was used to model the target panels, and the FSP was modeled with hexahedral finite elements. The principle data for these simulations are now shown. A typical LDPM-F mesh for 50.8 mm thick panel contained approximately 20,000 fibers, 115,000 LDPM particles, and 670,000 tetrahedral elements.

The Figs. Show snapshots of the penetration event characterized by the formation of entrance and exit craters. The Fig. shows the comparison between the post-penetration damage observed during the experiments (left) and that predicted by the simulation (right).
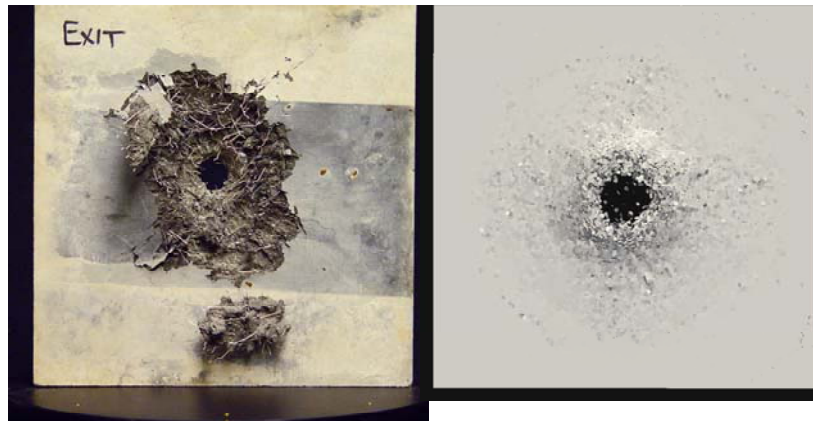
**Figure 5.9: Comparison between the post-penetration damage
of experimental and numerical slabs.**

Conclusions

In this thesis the Lattice Discrete Particle Model was calibrated in order to reproduce the experimental tests realized in the Laps, over concrete specimens.
In the same campaign, FRC specimens were performed and subjected to different tests.
Starting from these results, the goal was to extend the LDPM to include the effect of randomly dispersed fibers, using these experimental results to calibrate the new model. To achieve this aim fiber-matrix interaction was modeled by using an earlier formulated micromechanical theory providing the fiber crack bridging force as a function of the crack opening.
This law was coupled to the LDPM constitutive behavior at the facet level. The contribution of each individual fiber is taken into account by detecting the intersection between the fibers and the LDPM facets.
The formulated model, named LDPM-F, is able to reproduce the fiber toughening mechanisms and, once calibrated, is able to predict the macroscopic fracturing properties as a function of different fiber volume fractions.
The LDPM-F was used to investigate the effect of fibers on the penetration resistance of FRC slabs. Preliminary numerical results show that fibers influence significantly the penetration response for striking velocities close to the ballistic limit, whereas their effect tends to become less significant as striking velocity increases.

Bibliography

Begnini, A., Bažant, Z.P., Zhou, Y., Gouirand, O. and Caner, F.C. (2007). "Microplane Model M5 for Multiaxial Behavior and Fracture of Fiber-Reinforced Concrete" *Journal of engineering mechanics © ASCE/ January 2007.*

Buratti, N., Mazzotti, C., Savoia, M. and Thooft, H. (2008). "Study of the behavior of concrete reinforced through steel and polymeric fibers". *XVII Congress C.T:E., 5-8 November, 2008. Rome (Italy).*

Bolander, J.E., Yoshitake, K. and Thomure, J. (1999). "Stress analysis using elastically uniform rigid-body-spring networks". *J. Struct. Mech. Earthquake Engng. (JSCE), 633(I-49): 25-32.*

Cailleux, E., Cutard, T. and Bernhart, G. (2005). "Pullout of steel fibers from a refractory castable. Experiment and modeling". *Mechanics o Materials, 37:427-445.*

Camacho, G.T., and Ortiz, M. (1996). "Computational modelling of impact damage in brittle materials". *Int. J. of Solids and Struct. 33(20-22), 2899–2938.*

Carol, I., Lopez, C.M., and Roa, O. (2001). "Micromechanical analysis of quasi-brittle materials using fracture-based interface elements". *Internat. J. Numer. Methods Engrg., 52:193-215.*

Cusatis, G. (2001). "Tridimensional random particle model for concrete". *Ph.D. Thesis, Graduate School in Structural Engoneering, Politecnico di Milano, Piazza Leonardo da Vinci 32, 20133, Milan, Italy.*

Cusatis, G., Bažant, Z.P., and Cedolin, L. (2006). "Confinement-shear lattice CSL model for fracture propagation in concrete". *Compure Methods in Applied Mechanics and Engineering, 195(52):7154-7171.*

Cusatis, G., Bažant, Z.P., and Cedolin, L. (2003a). "Confinement-shear lattice model for concrete damage in tension and compression: I. Theory". *Journal of Engineering Mechanics-ASCE, 129(12):1439-1448.*

Cusatis, G., Bažant, Z.P., and Cedolin, L. (2003b). "Confinement-shear lattice model for concrete damage in tension and compression: II. Computation and validation". *Journal of Engineering Mechanics-ASCE, 129(12):1449-1458.*

Cusatis, G., Schauffert, E.A., Pelessone, D., O'Daniel, J.L., Marangi, P., Stacchini M. and Savoia, M. (2009). "Lattice Discrete Particle Model for Fiber Reinforced Concrete (LDPM-F) with Application to the Numerical Simulation of Armoring Systems".

Cusatis, G., Pelessone, D., Mencarelli, A. and Baylot, J. T. (2008). "Lattice Discrete Particle Model (LDPM) for Fracture Dynamics and Rate effect in concrete". *Proceedings of the 2008 ASCE Structures Congress, April 24-26, 2008, Vancouver, Canada.*

Cusatis, G., Pelessone, D., Mencarelli, A. (2009). "Lattice Discrete Particle Model (LDPM) for Concrete. I: Theory.".

Chern, J.-C., Yang, H.-J., and Chen, H.-W.(1992). "Behavior of steel fiber-reinforced concrete in multi axial loading". *ACI Mater. J., 89(1), 32-40.*

Cho, S. H., and Kim, Y.I. (2003). "Effects of steel fibers on short beams loaded in shear". *ACI Struct. J., 100(6), 765-774.*

Grimaldi, A., and Luciano, R. (2000). "Tensile stiffness and strength of fiber-reinforced concrete." *J. Mech. Phys. Solids, 48(9), 1987-2008.*

Hanchak, S.J., Forrestal, M., Young, E.R. and Ehrgott, Q. (1992). "Perforation of concrete slabs with 48 MPa (7ksi) and 140 MPa (20ksi) unconfined compressive strength." *Int.J. Impact Engng Vol. 12, No. 1, pp. 1-7.*

Kabele, P. (2004). "Linking scales in modelling of fracture in high performance fiber-reinforced cementitious composites". *Fracture Mechanics of Concrete structures, Proc., FraMCoS-5, 5th Int. Conf. on Fracture mechanics of Concrete and Concrete Structures, Vail, Colo., Vol. 1, V.C. Li, K. Y. Leung, K. J. William, and S.L. Billington, eds., IA-FracMCoS, Evanston, I11, pp. 71-80.*

Kanda and Li (1998). "Interface property and apparent strength of a high strength hydrophilic fiber in cement matrix". *ASCE Journal of Materials in Civil Engineering, 10(1), pp. 5-13.*

Katz. A., Li V.C. (1996). "A special technique for determining the bond strength of carbon fibers in cement matrix by pullout test". *Journal Materials Science Letter 15 (1996) pp. 1821-182..*

Kholmyansky, M. M. (2002)."Mechanical resistance of steel fiber-reinforced concrete to axial load". *J. Mater. Civ. Eng., 14(4), 311-319.*

Kullaa, J. (1994)."Constitutive modeling of fiber-reinforced concrete under uniaxial tensile loading". *Composites, 25(10),pp. 935-944.*

Kwak, Y. K., Emberhard, M. O., Kim, J. (2002). "Shear strength of fiber-reinforced concrete beams without stirrups". *ACI Struct. J., 99(4), 530-538.*

Leung, C.K.Y. and Li, V.C., (1992). "Effect to fiber inclination on crack bridging stress in brittle fiber reinforced brittle matrix composites". *J. Mech. Phys. Solids, 40(6):1333-1362.*

Lin, Z., Kanda, T. and Li, V.C. (1999). "On interface property characterization and performance of fiber-reinforced cementitious composites". *Concrete Science and Engineering, Vol. 1, September 1999, pp. 173-185.*

Lin, Z. and Li, V.C. (1997). "Crack bridging in fiber reinforced cementitious composites with slip-hardening interfaces". *Journal of Mechanics and Physics of Solids, 45(5), pp. 763-787.*

Li, F., and Li, Z. (2001). "Continuum damage mechanic based modeling of fiber-reinforced in tension". *Int. J. Solids Struct., 38, 777-793.*

Li, Z., Li, F., Chang, T.-Y.-P., and Mai, Y.W. (1998). "Uniaxial tensile behaviour of concrete reinforced with randomly distributed short fibers". *ACI mater. J., 95(5), pp. 564-574.*

Li, V.C., Stang, H. and Krenchel, H. (1993). "Micromechanics of crack bridging in fiber-reinforced concrete". *Materials and Structures, (26), pp. 486-494.*

Mencarelli, A.(2007). "the lattice discrete particle model (ldpm) for concrete: calibration and validation under quasi-static loading conditions". *Ph.D. Thesis, Graduate School in Structural Engineering, Rensselaer Polytechnic Institute, Troy, New York.*

Mindess, S., Yang, C. (1993). "Perforation of plain and fibre reinforced concretes subjected to low-velocity impact loading." *CEMENT and CONCRETE RESEARCH. Vol. 23, pp. 83-92.*

Mirsayah, A. A., and Banthia, N. (2002). "Shear strength of steel fiber-reinforced concrete". *ACI Mater. J., 99(5), 473-479.*

Morton, L. and Groves, G:W. (1979). "The effect of met al wires on the fracture of a brittle matrix composites". *Journal of Material Science, (11), pp. 617-622.*

Nataraja, M. C., Dhang, N., and Gupta, A. P. (1999). "Stress-strain curves for steel-fiber reinforced concrete under compression". *Cem.Concr.Compos., 21 (5-6), 383-390.*

Pantazopoulou, S.J., and Zanganeh, M. (2001). "Triaxial tests of fiber reinforced concrete". *J. Mater. Civ. Eng., 13(5), 340-348.*

Peng, X., and Meyer, C. (2000)."A continuum damage mechanics model for concrete reinforced with randomly distributed short fibers". *Comput. Struct., 78, 505-515.*

Rameh, K., Seshu, D. R., and Prabhakar, M. (2003). "Constitutive behavior of fibre reinforced concrete under axial compression". *Cem. Concr. Compos., 25(3), 343-350.*

Redon, C., Li, V.C., Wu, C., Hoshiro, H., Saito, T. and Ogawa, A. (2001). "Measuring and modifying interface properties of PVA fibers in ECC matrix". *ASCE Journal of Materials in Civil Engineering, 13(6), pp. 399-406.*

Schlangen ,E., and Van Mier, J.G.M. (1992). "Shear fracture in cementitios composites, Part II: Numerical simulations. Fracture mechanics of concrete structures". *Proc. FraMCoS-1, Bažant Z.P., ed., Elsevier, London, 671-676.*

Traina, L. A., and Mansour, S. A. (1991). "Biaxial strength and deformational bahavior of plain and steel concrete". *ACI Mater. J., 88(4), 354-312.*

Wang, Y., Li, V.C. and Backer, S. (1988). "Modeling of fiber pull-out from a cement matrix". *Journal of Cement Composites and Lightweight Concrete, 10(3), pp. 143-149.*

Wittmann, F.H., Roelfstra, P.E., and Kamp, C.L. (1988). "Drying of concrete: an application of the 3L-approach.". *Nucl. Eng. Des., 105:185-198.*

Yang, E.-H., Wang, S., Yang, Y, and Li, V.C. (2008). "Fiber-Bridging Constitutive Law Of Engineered Cementitious Composites". *Journal of Advanced Concrete technology Vol. 6, No. 1, 181-193, February 2008.*

Yang, E.H., Wang, S. , Yang, Y., and Li, V.C. (2007). "Fiber-Bridging Constitutive Law of Engineered Cementitious Composites". *Journal of Advanced Concrete Technology Vol. 6, No. 1, 181-193, February 2008 © 2008 Japan Concrete Institute, ys. Solids, 48(9), 1987-2008.*

Yin, W. S., SU, E. C. M., Mansur, M. A., and Hsu, T. T. C. (1998). "Biaxil tests of plain and fiber concrete". *ACI Mater. J., 86(3), 236-243.*

Acknowledgment